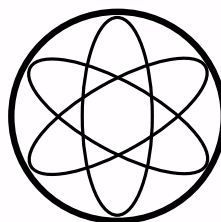Technische Universität München
Fakultät für Physik
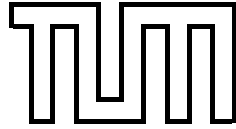
Dissertation

**Diffraction Based Investigation
of Elastic and Plastic Deformation
on Multiphase Alloys**

von
Alexander Erwin Heldmann
Februar 2021

Heinz Maier-Leibnitz Zentrum

Fakultät für Physik

TECHNISCHE UNIVERSITÄT MÜNCHEN

Forschungs- und Neutronenquelle Heinz-Meier Leibnitz
(MLZ)

Diffraction Based Investigation of Elastic and Plastic Deformation on Multiphase Alloys

Alexander Erwin Heldmann

Vollständiger Abdruck der von der Fakultät für Physik der Technischen Universität München zur Erlangung des akademischen Grades eines

Doktors der Naturwissenschaften (Dr. rer. nat.)

genehmigten Dissertation.

Vorsitzender:

Prof. Dr. Frank Pollmann

Prüfer der Dissertation:

1. Prof. Dr. Winfried Petry
2. Prof. Dr. Wolfgang W. Schmahl

Die Dissertation wurde am 15.02.2021 bei der Technischen Universität München eingereicht und durch die Fakultät für Physik am 04.05.2021 angenommen.

Für meinen Vater,
einem einzigartigen Menschen, mit dem ich viele großartige Stunden verbringen durfte.
Ruhe in Frieden

Abstract

In recent years the demand on new more versatile engineering components and new metal printing techniques led to an increase in material development and testing. As research progresses on this field new methods in industrial manufacturing became available to set parameters like the texture or microstructure. Therefore it is necessary to provide reliable and fast measurement techniques to characterize and predict all basic mechanical parameters such as the single-crystal elastic constants, critical resolved shear stresses and the stress distribution among phases.

This work provides a diffraction measurement technique for the investigation and characterization of the mechanical behavior on polycrystalline multiphase engineering alloys. Diffraction techniques are used first to determine all relevant elastic properties, the single-crystal elastic constants, anisotropy and all bulk elastic moduli. This includes a self-consistent calculation to determine and account for the stress distribution in multiphase materials improving significantly the obtained results. Then they are used to determine plastic parameters such as the critical resolved shear stresses and track the microstructural evolution by evaluating the Bragg peak areas and FWHMs occurring at different deformation stages during the experiment. The last section contains an elasto plastic self consistent modeling based on the previous results. The obtained lattice-strain - macro-stress curves are directly compared to the experimental data. The reliability and accuracy of this method has first been tested on different single and dual phase ferrous metals. It was later used to not only investigate the titanium alloys Ti64 and Ti38644 two single-phase alloys consisting of a h.c.p. and b.c.c. crystal structure. But it was also used to determine all eight single-crystal elastic constants considering the load partitioning of the dual phase alloy Ti6246 during a single experiment for the first time. The Experiment was further evaluated in the plastic regime and different deformation behaviors of Ti6246 are discussed.

Kurzzusammenfassung

In den letzten Jahren hat sich die Nachfrage und Entwicklung nach flexibleren Komponenten stark erhöht. Einerseits sind die Kosten für die industrielle Fertigung von komplexen Verbundmaterialien stark gesunken andererseits drängen neue Fertigungstechnologien, wie die Möglichkeit eine Vielzahl von Materialien zu drucken, auf den Markt und verändern diesen entscheidend. Aus diesem Grund ist es unerlässlich neue schnelle und verlässliche Methoden zur Materialcharakterisierung zu finden, um den zukünftigen Herausforderungen in Forschung und Industrie begegnen zu können.

In dieser Arbeit wird eine diffraktometrische Messmethodik zur Bestimmung und Charakterisierung der mechanischen Eigenschaften von polikristallinen multiphasen Werkstoffen vorgestellt. Zunächst werden alle relevanten elastischen Eigenschaften wie die elastischen Einkristallkoeffizienten, Anisotropie und makroskopischen Module mittels Diffraktion bestimmt. Dies beinhaltet insbesondere eine selbstkonsistente Berechnung der Lastverteilung in multiphasen Werkstoffen, die die Auswertung der elastischen Einkristallkoeffizienten wesentlich verbessert. Die so erworbenen Materialkennwerte werden anschließend als Ausgangsdaten für eine elasto-plastische selbstkonsistente Modelierung verwendet. Die berechneten Spannungs-Dehnungskurven werden direkt mit den experimentel erworbenen Gitterdehnungen und Makrowerten verglichen. Die Methodik wird zunächst an verschiedenen Eisen- und Stahllegierungen auf ihre Genauigkeit geprüft. Im späteren Verlauf werden nicht nur die einphasigen Titanlegierungen Ti64 und Ti38644 auf ihre mechanischen Eigenschaften untersucht sondern es ist auch gelungen alle acht elastischen Einkristallkoeffizienten der zweiphasigen Titanlegierung Ti6246 unter Berücksichtigung der Lastverteilung der Phasen innerhalb eines einzigen Experiments zu bestimmen. Der letzte Teil der Arbeit umfasst eine ausführliche Auswertung der plastischen Deformation von Ti6246 mittels Diffraktionsexperimenten.

Preface

This thesis is submitted in fulfillment of the requirements for a doctoral degree in the Faculty of Physics of Technische Universität München in Germany. The research was carried out between July 2016 and Februar 2021 at the MLZ institute Heinz Maier-Leibnitz in Garching (FRM II). The aim of this project was to implement new diffraction methods to evaluate the stress-strain behavior of engineering materials. I am very greatful for the opportunity to achieve my doctoral research under the supervision of Prof. Dr. Winfried Petry and the financial support granted by the MLZ facility.

Special thanks goes to Dr. Markus Hoelzel for his great support during my studies. He helped with his experience and paid attention to a lot of details during the planning of all experiments. I also would like to thank Dr. Michael Hofmann for his support at the Stress-Spec instrument and knowledge of materials science. I am thankful for all the valuable discussions we three had together. I also owe my gratitude to Prof. Dr. Winfried Petry, Dr. Markus Hoelzel and Dr. Michael Hofmann for reviewing my thesis.

I appriciate the beam times granted for my core studies on SPODI at the MLZ and the technical assistance of Josepf Pfanzelt during setup. I would also like to thank Dr. Weimin Gan for his support during the texture analysis and the beam time I received for my studies on STRESS-SPEC at the MLZ. I acknowledge the beam time at the neutron diffractometer D20 located at the Institute Laue-Langevin (ILL) and thank the assistance of Dr. Thomas Hansen and his team by installing the experimental setup on-site. Furthermore, I wanted to thank the team at the High Energy Materials Synchroton Beamline at DESY for their technical assistance during the synchroton Experiments and the possibility to carry out the experiments necessary to complete my studies.

I owe my gratitude to Prof. Dr. Schmahl for the interesting discussions and valuable input for my studies. A special thank also goes to Dr. Erika Grießhaber for the EBSD measurements and preparation of the samples with thanks to the team who have worked on the ion-polishing. I also wanted to thank Mr. Armin Kriele for the assistance at cutting and polishing the samples adn granted me access to the advances materials lab at the MLZ facility.

Finally, I wanted to thank my family for their support, especially my grandmother and my mother. You made it possible for me to accomplish my goals.

Contents

List of Figures

List of Tables

List of Abbreviations

ϵ_{ik}	Elements of the Strain Tensor
$\hat{C}$	Crystal Frame
$\hat{L}$	Measurement Frame
$\hat{S}$	Sample Frame
$\mathbf{A}$	General tensor of compliance
$\mathbf{C}$	Tensor of Stiffness
$\mathbf{S}$	Tensor of Compliance
$\mathbf{u}$	Displacement Vector
σ_{ik}	Elements of the Stress Tensor
$\mathbf{A}'(g)$	General tensor of compliances expresses in the measurement frame with the orientation g
$\mathbf{F}_{ij}(\mathbf{Q}, hkl)$	Components of the stress factor
ξ	Transformation matrix from the crystal to the measurement frame.
$\mathbf{Q}$	Measurement vector
m. r. d.	multiples of random distributions
$\mathbf{m}$	Plain normal
DEC	Diffraction Elastic Constants
$S_1, \frac{1}{2}S_2$	Diffraction elastic constants
γ_i	Orientation parameters along crystallographic directions
ν	Poisson ratio
κ	Bulk modulus
G	Shear modulus
E	Young's modulus
$\mathbf{f}^\alpha$	Stress transition factors of phase α
$\mathbf{w}$	Eshelby's Tensor
$\mathbf{I}$	Unity Tensor
A	Zener Anisotropy
EPSC	Elasto Plastic Self-Consistent
τ_c^i	Critical Yield Stress or Yield Strength of Slip System i
α	Resolving Parameter Determining the Total Shear Stress Along a Specific Crystallographic Direction
$\dot{\gamma}^i$	Shear Rates
$\mathbf{h}$	Hardening Matrix Defined by Activated Slip Systems
$\mathbf{L}$	Instantanious Stiffness Coefficients

1   Introduction

The demands on modern engineering components led to an increase in materials development and testing in recent years. New reliable and precise methods for the characterization of the basic mechanical parameters such as the single-crystal elastic constants, critical resolved shear stresses of slip families among many others are needed to meet future requirements in science and industry.

One aspect in modern engineering is to predict the stress-strain behavior of the key components during operation. These predictions are often used to decide which materials are of general interest or to solve specific problems for researchers and industry, alike. Most commonly finite element models (FEM) are used for the prediction of large scale deformation behavior and the FEM rely on a precise knowledge of the single-crystal elastic constants, yield stress, present micro structure and in some cases the elemental composition.

Besides the requirements every material has to full-fill during operation, the manufacturing and shaping during assembling additionally stresses the materials and can sometimes reduce the durability significantly. An important technique to investigate the evolution of materials during use or assembling is the diffraction based classical stress analysis. It takes into account the present phases and its precision depends on the accuracy of the diffraction elastic constants used for the evaluation of the measurement. They can either be measured in-situ by diffraction in a tensile experiment or they can be calculated from the single-crystal elastic constants using different grain-to-grain interaction models.

The classical stress analysis is also widely used in geology and encounters even larger difficulties. Many of the investigated materials have low symmetry crystal structures, complex microstructures and are brittle which is very common for rocks or ceramics.

There are only few limited methods to access these single-crystal elastic constants and besides the diffraction techniques all of them require the measurement of single-crystals. The most established method uses ultra-sounds. The use of single-crystals during measurements is essential to gain accurate results [1]. Another technique to determine single-crystal elastic constants is inelastic neutron scattering which measures the phonon dispersion relation [2]. This gives access to constants even in extreme conditions or unstable phases. However, it is difficult to grow single-crystals with similar elemental composition as used in modern engineering alloys.

As mentioned above, it is not possible to grow single-crystals for most engineering materials. To overcome the limited access to single-crystals, different approximation models have been developed to project the elastic constants from one alloy to a similar one. Depending on the complexity these projections may be afflicted by large uncertainties which heavily influences the accuracy of the predictions.

Improved manufacturing processes allow production of multi-phase materials with defined

phase ratios. Components made from such multi-phase materials often benefit from combining the properties of the constituent phases. For example in aerospace turbines high durability in extreme conditions needs to be ensured. It was discovered that especially dual-phase titanium alloys match the high requirements needed. Here the α-phase ensures the ductility while at the same time the β-phase improves corrosion resistance and high temperature yield. However, in many cases one or more of the occurring phases are only meta stable and therefore exist only in presence of the other phase. In this case it is inevitable to investigate mechanical properties of the compound as well as single-crystal properties at the same time. This is of particular interest, when the elasticity differs strongly from phase to phase the stress does not uniformly distribute among the present phases and leads to so called "load-transfer" where the stress in one phase is significantly higher than in the other during loading.

In a similar way additive manufacturing is gaining more and more interest in industry and research as an advanced production process. Sharp and distinct textures are created commonly during the printing of engineering components. An investigation on the impact to the elastic bulk properties will reveal if any artificial setting of the grain orientation would improve the components mechanical properties.

Single-elastic constants are required in all common deformation theories to predict mechanical behavior of engineering components. However, the difficulty to access these constants led to a severe lack of data in modern material developments. Only for a small proportion of materials reliable literature values are available and even fewer remain consistent in case of varying measurement conditions. One of the few well known materials on this area are ferrous metals. Their versatility ensured their use over many decades and their importance in modern days is hard to underestimate. Therefore they still are object to extensive research due to their high value in all different kinds of modern industries [3, 4, 5, 6, 7, 8].

The steady amount of new materials and the increasing amount of research require the development of standard procedures to generalize the obtained results for an easier use among the many different areas of application. The diffraction technique introduced here, offers a sophisticated method to meet these requirements. It ensures high precision and straightforward evaluation of experiments. Besides the experimental procedure a newly implemented software written in a modern programming language is introduced which allows an easy evaluation of the measurement. The software accounts for a wide range of materials and is flexible enough to adapt to the different micro structures and diffraction methods give information on any present phase. Therefore the software accounts for multiple phases present and the distribution of stress between them.

Many of the utilized theories were included into the Elasto-Plastic Self-Consistent (EPSC) modeling. Therefore the EPSC modeling implemented into the software benefits from directly measured input parameters from a single experiment. The wide field of accessible

materials offer countless opportunities for further development and research.

The accuracy of the experiment and evaluation procedure is demonstrated here on ferrous metals. The results of the f.c.c. and the b.c.c phase of single and dual-phase alloys are compared to available literature data. The EPSC framework implemented is used to describe and predict the deformation behavior of austenitic steel. The prediction of the EPSC model is tested against experimental data obtained during a diffraction tensile test on ferritic structural steel S235JR. Further investigations on a dual-phase titanium alloy and the load distribution between the α and the β phase are presented. A detailed overview of the morphology and texture is also given as it is required to perform a correct analysis and develop a proper understanding for the mechanism acting. The last part of this work presents the plastic deformation behavior of a dual phase titanium alloy. Diffraction techniques are used in combination with the microstructural investigation to qualify the plastic deformation mechanism such as dislocation or stress pile-up, slip transfer and stress redistribution.

2 Historical Review on the Deformation of Solids

In this section a historical review and a timeline (figure 1) on titanium alloys and on the modern theory of elasticity is given with a particular focus on embedding diffraction methods into the characterization and modeling.

17th and 18th century

The first principles of linear elastic deformation have been stated in the late 17th-century by the British physicist Robert Hooke. Hooke's law states that "*The force needed to extend or compress a spring by some distance scales linearly with respect to that distance*". It was easily recognized that Hooke's law in his linear form is only a first order approximation to describe the deformation behavior of real solid bodies.

After 1800 a.d. when matrices became more popular in mathematics a generalization of Hooke's law for small deformations has been elaborated and the modern theory of elasticity has been founded.

In 1791 titanium was first discovered by the English pastor William Gregor. But due to the high melting point of 1993 K its practical use at that time was very limited.

1910 - 1930

Evolving manufacturing processes and better equipment in research draw the interest of M. A. Hunter and the General Electric Company on titanium alloys in the believe it could withstand $6000°$C in its pure metallic form. So in 1906 Hunter was the first to produce pure metallic titanium and found that its melting point is lower than expected. But, anyhow he invented a commercially method of production for $TiCl_4$ the Hunter process which was named after him.

The elasticity of most commonly used materials had been only partly described by the single-crystal approximation and therefore the theory was expanded for polycrystals. At the beginning of the 20th century Voigt and Reuss elaborated an analytical solution for the deformation behavior of polycrystals for small strains with extreme assumptions. Voigt assumed that the occurring strains distribute evenly in the solid and the stress varies accordingly. This led to isotropic behavior of the polycrystal [9, 10]. The other extreme was solved by Reuss, he assumed that the stress is distributed homogeneously over the solid which lead to an anisotropic solution for the deformation behavior [11].

At the same time engineering was evolving and the behavior of large strains, i. e. the plastic behavior, became more important. The first approach for the large strain behavior of an ideal single-crystal was emphasized by Taylor and Elam in 1923 [12].

1946

A study conducted by the U.S. Air Force in 1946 concluded that titanium-based alloys meet all requirements needed for aerospace industry. Importantly they exceed the strength-to-weight ratio of either steel or aluminum by far. In consequence the nations as to name the U.S.A, United Kingdom, Japan and the U.S.S.R. founded new titanium branches among their metalworking industry. The new availability of the metal to other branches of the industry and research gave rise to many new opportunities in for example chemical processing, medicine and power generation.

1950s

The next major advancements in the theory of elasticity were made in the 1950s. The first and most reliable measure for the anisotropy was introduced by Zener in 1948 for cubic materials [13]. A new description of the strain behavior along different crystal orientations is established. The anisotropy gets more complicated with growing degree of freedom for lower crystal symmetries. Only many years later several approaches were established to create evenly reliable measures of anisotropy for different crystal symmetries.

At the same time Hill verified the solutions of Voigt and Reuss as the upper and lower limit for the predicted strains and proposed the arithmetic mean introduced by Wu and Walpole as a more accurate description for the strain behavior of a crystalline aggregate often called as Hill's approximation [14].

One of the most common used titanium alloys Ti-6Al-4V is introduced in 1954 to aerospace and armor industry. It is the first titanium alloy used for mass fabrication.

1960s

In 1957 Eshelby introduced what is best described as an elastic susceptibility by introducing the *inclusion model* into the modern theory of elasticity. Many models describing small or large strain behavior rely strongly on the *inclusion model* [15]. One year later Kroener derived a more elaborated approach for the grain-to-grain interaction and provided new equations for the large strain behavior of single crystals [16]. In 1963 Kneer extended the work of Kroener to hexagonal symmetries [17]. The next couple of years Hill elaborated a new generalization between differential increments of stress and strain during the different stages of plastic deformation. This approach establishes a basis for the description of plastic deformation behavior in poly-crystalline materials also known as *Elasto Plastic Self-Consistent Modeling* (EPSC) [18, 19, 20].

At the same time high-temperature applications of titanium were gaining the interest of the U.S. and U.S.S.R because of their use for space flights. To win the space race both nations put a huge effort into the development of new alloys capable of resisting extreme conditions. One of the least dense β-alloys Ti-3Al-8V-6Cr-4Mo-4Zr was introduced just before in 1966.

An alloy featuring a similar high-strength as the titanium α-phase and the high corrosion resistance of the β-phase is introduced to the metal community. The well behavior of the metastable β phase during manufacturing leads to a fast development for mass fabrication of this alloy.

1970s

In the following years Hutchinson evaluated the models proposed by Hill through extensive research and experiments. He further developed and simplified the models and made significant contributions to the *Elasto Plastic Self-Consistent Modeling* of f.c.c. and b.c.c. crystal symmetries. He analyzed the influence of different parameters during the modeling and backed his conclusion with different types of tensile loading experiments. [21, 22].

1979

For the improvement of the prediction by EPSC models the precise knowledge of the input parameters became of great importance. Therefore in the same time period many research groups started collecting elastic and plastic properties of different single crystals by ultrasound measurements. A suggestion of how to overcome the obstacle of measuring the single-crystal elastic constants in technologically relevant polycrystals was first emphasized by Hauk & Kockelmann in 1979. The basic idea is to apply an externally known stress to the material and measure the average resulting strains by diffraction methods. It arose from the classical stress analysis were internal stresses are calculated by measuring occurring strains in the materials which is essentially its reverse [23].
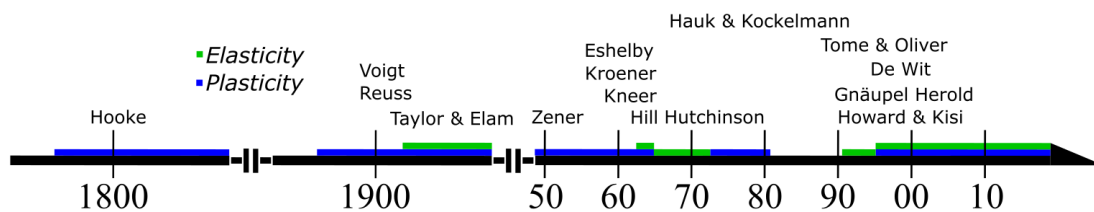
Figure 1 – The time line shows some of the important research groups. The blue and green line indicates large advancements on field of elastic and plastic deformation, respectively.

1990s

In the early 90s Ti6Al-4V was recognized as highly flexible implant with low Young's modulus. Its mechanical properties combined with its high bio compatibility makes it unique until today. Next major advancements in EPSC modeling were made around the turning of the century. Computational power increased and was easily accessible in research. Thus, it was realized that the averaging methods used during the EPSC modeling are naturally suited to be used for comparison to diffraction data. Throughout the 90s Tome and his group implemented a new version of the models suggested by Hill and Hutchinson in Pascal[24].

2000s

The models implemented in the EPSC evaluation developed by Tome were extended to account for grain reorientation due to twinning and enabling the modeling of hexagonal crystal structures for the investigation of Zircaloy-2 [25, 26, 27]. The computational power reached the point where different types of texture could be included into the modeling and Matthies investigated the influence of the texture on the different types of grain-to-grain interaction models. At the same time he introduced a new average between Voigt and Reuss models which better suits real physical conditions [28, 29].

In the year 1997 the grain-to-grain modeling suggested by Kroener was extended by De Wit to account for present anisotropies by including an orientation dependence of the shear modulus into the equations [30]. One year later Gnäupel-Herold et al. further applied the idea of Hauk & Kockelmann and derived the single-crystal elastic constants of different f.c.c and b.c.c phases in ferrous metals by diffraction methods [8] on basis of Kroeners approach. Howard & Kisi extended the equations elaborated by Reuss to fit for all different types of crystal symmetries in the same year to derive all 5 elastic constants of the α-phase in Ti64 [31]. This technique was further modified to fit different models proposed by Hill and Reuss [32, 5, 6].

The economical pressure forces the aerospace industry among many others to produce more efficient components. To meet the negotiated standards all industries are pushed into new fields of development for high efficiency materials. In consequence different properties are combined and the availability of dual-phase alloys grows as new opportunities for research arise. Ti 6246 combined the high ductility of the α-phase and the high temperature performance of the β-phase in extreme environments and became a new standard alloy in high-temperature jet engines, gas turbine compressor components and in high performance automotive valves. Even though the field of applications was growing only few groups as for example Fre'our et al. put effort into the further development of grain-to-grain interaction models or the influence of doping elements on the single-crystal elastic constants[33, 34, 35].

2010s

Upcoming printing methods enable the printing of three dimensional shapes. The technology was first available for plastic parts, only. In a short time the technology was further developed to print metal components. Soon Ti64 emerged to a highly appropriate candidate for additive manufacturing and to create shapes which are challenging for conventional production. Investigations show an interesting texture development during additive manufacturing which leads to the conclusion that the texture development can be used as advantaged depending on the given shape of the component.

The easy availability of even very complex engineering materials and a growing interest in

the development of texture leads to a need of more complex anisotropy measures. During the last years there is growing effort to find equally good measures which apply to a more wide range of structures[36, 37, 38, 39].

3 Goals

The aim of this work is to develop an easy to use and fast procedure to measure and predict the stress-strain behavior of engineering materials. The use of diffraction methods provides advantages during the investigation because they are able to deliver precise information on lattice spacing even in complex multi-phase materials. On this basis the technique is able to determine the single-crystal elastic constants of materials as they are deployed for operation. The similarities between diffraction techniques and the EPSC modeling framework provide a good premise to compare the predictions of the EPSC modeling to diffraction data and ensure the correctness of the modeled plastic stress-strain behavior. This means that this method allows to quantify the elastic and plastic behavior of any crystalline material during a single measurement.

To achieve this goal a technique first used by Gnäupel-Herold et al. to determine the elastic constants of single-phase cubic alloys is implemented and is further developed to handle modern anisotropic multi-phase alloys including texture effects. A standard experimental procedure is given using a specific test rig with a rotatable load axis on diffractometers. The method allows simultaneous measurement of multiple phases in a compound and extract all relevant single-crystal and bulk elastic properties.

To account for the stress re-distribution among the different phases a self-consistent method is developed and applied which quantifies the load transfer by transition factors for every phase. These allow to calculate the stress present in each phase from the applied sample stress.

For the data treatment a dedicated software had to be developed due to a lack of existing maintained solutions developed for modern computer systems which are able to process diffraction and other experimental data for a full analysis of every aspect during elastic and plastic deformation. The software accounts for multiple phases and predicts the load transfer depending on the elastic properties of the phases. It is designed to handle diffraction, tensile, texture and crystallographic data comfortably and includes them into the evaluation process. For the plastic regime an EPSC modeling framework is used. It predicts the average strain values measured by diffraction. In addition, it allows further predictions of strains along orientations, which are not accessible by diffraction experiments.

The accuracy of the evaluation is tested on different ferrous metals because of the large amount of available literature data. The results of two single-phase alloys with f.c.c. and b.c.c. crystal structure and two dual-phase alloys are compared to these reference values and a detailed analysis of the different grain-to-grain interaction models and texture is provided. The technique was finally applied to determine all 8 single-crystal elastic constants in an industrial used dual-phase titanium alloy, simultaneously. To account properly for the phase interaction this work provides detailed information on the morphology and texture. The

predicted constants are compared and discussed with respect to a detailed analysis of the corresponding phases in single-phase alloys.

4 Theory

This section summarizes all necessary parts of the theoretical background needed for complete data treatment and analysis. The formalism used mainly originates from Behnken, Hill, Hutchinson and Gnäupel-Herold [40].

In the first part all principle definitions regarding mechanical deformation are introduced. This comprises basic definitions, notations and commonly used coordinate systems. For proper understanding it is vital, how the experimental measurements are aligned with respect to the coordinate systems defined in modern deformation theory. The same applies to the length scales for which different types of strains are considered. It is important to describe how the applied tensile force during diffraction experiments distributes among the different grains and present phases.

In the following basic units as measured strains and applied stresses are categorized in scale and coordinate systems. The introduced transformations are used to involve basic elements such as micro structure and texture into this framework and combine it to experimentally accessible parameters such as diffraction elastic constants. In this way even with standard industrial characterization methods poorly available properties such as anisotropy are covered. The core of the introduced framework is how the grains interact with another, usually referred to as grain-to-grain interactions. This part introduces different assumptions on how the stress or strain is distributed among the single-crystal domains and it combines basic micro structure into the evaluation. Diffraction experiments are sensitive to all present phases and in most cases the individual strains are measured simultaneously. To improve the evaluation of multi phase alloys the theoretical basis of how stress distributes in multi-phase compounds is introduced.

The final part focuses on the plastic deformation and gives a detailed introduction into the common theory of single-crystal deformation. It summarizes different slip families for different crystal symmetries and introduces slipping of crystallographic planes along specific directions as the basic mechanism causing large strains in single crystals. A way to predicting the stress-strain behavior is introduced along with the basic concept of crystal hardening. Finally, the single-crystal deformation theory is expanded by a self consistent approach to describe large strains in polycrystals, also known as Elasto-Plastic Self-Consistent Modeling (EPSC).

4.1 Mechanical Properties and their Orientations

The shape and volume are fundamental parameters to describe solids. Their mechanical behavior defines the change of these parameters under a given stress. The properties are macroscopic values but are linked on atomic scale.

The Strain Tensor   is defined by any change in volume or shape in solids, e.g. through deformation. It is caused by external forces and can be described by the displacement $\mathbf{u}$ of an arbitrary point $\mathbf{r}$ in the solid to $\mathbf{r}'$ (Figure 2). The length $\mathrm{d}l$ before deformation and $\mathrm{d}l'$ after is described by [41]:

$$\mathrm{d}l = \sqrt{\mathrm{d}r_1^2 + \mathrm{d}r_2^2 + \mathrm{d}r_3^2}$$

$$\mathrm{d}l' = \sqrt{(\mathrm{d}r_1 + \mathrm{d}u_1)^2 + (\mathrm{d}r_2 + \mathrm{d}u_2)^2 + (\mathrm{d}r_3 + \mathrm{d}u_3)^2}$$

With the substitution $\mathrm{d}u_i = \frac{\partial u_i}{\partial u_k}\mathrm{d}r_k$ and some permutations $\mathrm{d}l'^2$ can be rewritten into:

$$\mathrm{d}l'^2 = \mathrm{d}l^2 + 2\epsilon_{ik}\mathrm{d}r_i\mathrm{d}r_k \tag{1}$$

Equation (1) defines $\mathrm{d}l'^2$ as the sum of $\mathrm{d}l$ and a second term consisting of the so called strain tensor ϵ_{ik} defining the deformation given by:

$$\epsilon_{ik} = \frac{1}{2}\left(\frac{\partial u_i}{\partial r_k} + \frac{\partial u_k}{\partial r_i} + \frac{\partial u_l}{\partial r_i}\frac{\partial u_l}{\partial r_k}\right) \tag{2}$$

The strain tensor is by its definition symmetric, $\epsilon_{ik} = \epsilon_{ki}$. This means that for every point
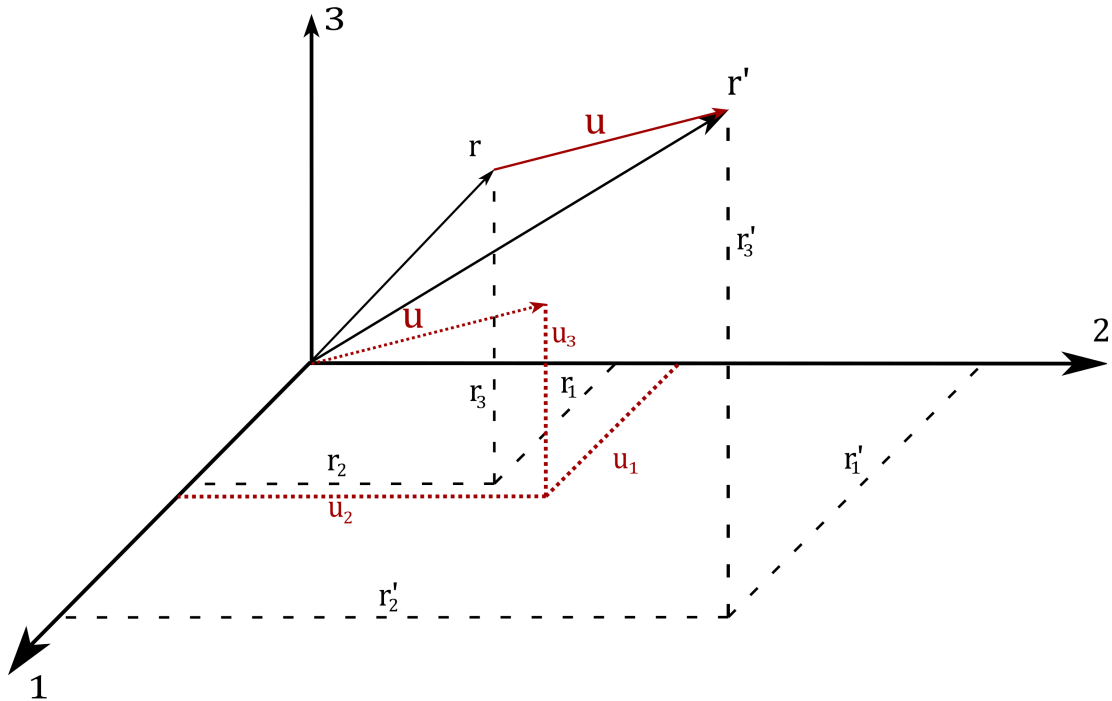
Figure 2 – The displacement vector $\mathbf{u} = \mathbf{r}' - \mathbf{r}$ describes the difference in space between the location $\mathbf{r}$ and $\mathbf{r}'$. The components of the strain tensor ϵ_{ik} are formed from derivatives of $\frac{\partial \mathbf{u}}{\partial \mathbf{r}}$.

of the strain field there exists a coordinate system, the so called principal axis, in which the only non-zero components of the strain tensor are the diagonal elements ϵ_{11}, ϵ_{22} and ϵ_{33} [41].

Even if the displacement vector may be large in special cases, the deformation of the solid

remains small, e.g. the components of the strain tensor are small in most cases. Therefore the last part of equation (2) can be neglected as small quantity of second order except for a few special cases[1][41].

$$\epsilon_{ik} = \frac{1}{2}\left(\frac{\partial u_i}{\partial r_k} + \frac{\partial u_k}{\partial r_i}\right) \tag{3}$$
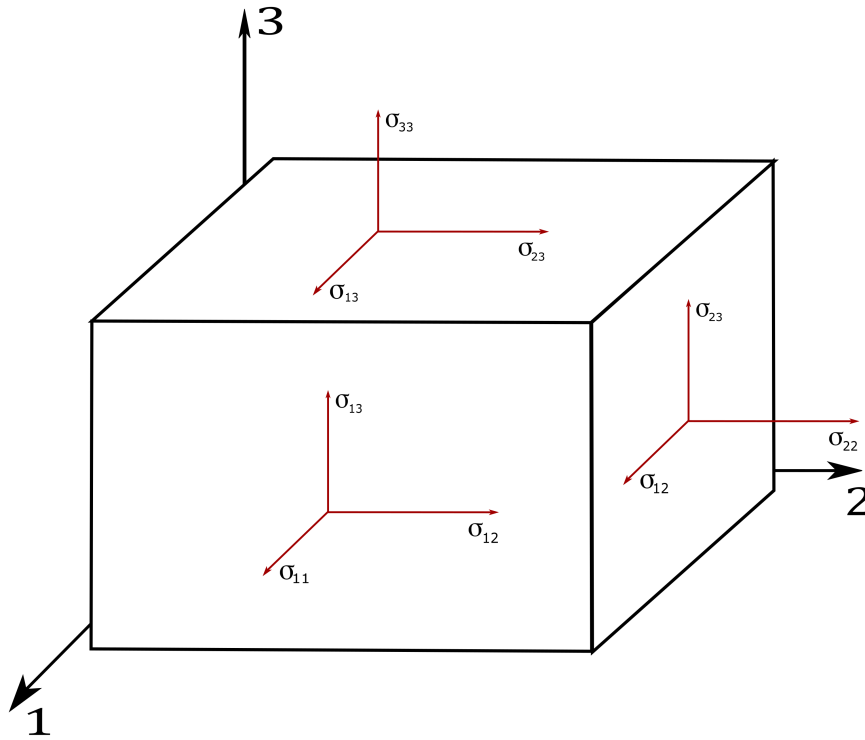
Figure 3 – The components of the stress tensor which are describing an applied force are shown for different interaction points [40].

The Stress Tensor   is most widely used to describe acting forces in solids. In a non-deformed solid in thermal equilibrium the atoms are arranged in a way that all parts are in mechanical equilibrium, too. This means the effective forces acting on any fraction of a volume disappear if cut out. During the deformation process the state of equilibrium is left and so called internal stresses appear in the solid in order to reestablish the equilibrium. These internal stresses are caused by inter-atomic forces which act only on a small scale, e.g. neighboring atoms. The resulting force on a specific volume part of the solid is given by $\int \mathbf{F} \mathrm{d}V$. The forces acting on one volume element can only act through the surface of the volume, therefore all three components of the force can be rewritten into an integral over the surface of the volume. This implies that the forces F_i can be represented by the

---

[1]In general a solid cannot undergo any deformation such that the shape in one dimension is getting especially small without causing heavy strains and compression.

divergence of a second rank tensor[41].

$$\int F_i \mathrm{d}V = \int \frac{\partial \sigma_{ik}}{\partial r_k} \mathrm{d}V = \oint \sigma_{ik} \mathrm{d}f_k \tag{4}$$

f_k are the normal components of the considered surface and σ_{ik} are the components of the stress tensor, which is a symmetric $(3\mathrm{x}3)$ second rank tensor [41]. Figure 3 shows how the stress tensor components act on different orientations of the surfaces. Depending on the surface orientation the stress tensor has one component in the normal direction and two in the tangential direction.

The average of the stress tensor is given by integrating $\frac{\partial \sigma_{il}}{\partial r_l} r_k$ over the total volume of the body.

$$\int \frac{\partial \sigma_{il}}{\partial r_l} r_k \mathrm{d}V = \int \frac{\partial (\sigma_{il} r_k)}{\partial r_l} \mathrm{d}V - \int \sigma_{il} \frac{\partial r_k}{\partial r_l} \mathrm{d}V = 0 \tag{5}$$

The first integral gets rewritten into a surface integral and considering $\frac{\partial r_k}{\partial r_l} = \delta_{kl}$ the above equation becomes to:

$$\oint \sigma_{il} r_k \mathrm{d}f_l - \int \sigma_{ik} \mathrm{d}V = 0$$

The surface integral expresses the external forces acting on the whole surface of the considered body. Which means that the average of the stress tensor can be immediately calculated by external forces without solving the basic equations of the equilibrium [41].

$$\int \sigma_{ik} \mathrm{d}V = V \overline{\sigma}_{ik} \tag{6}$$

Hooke's Law   If an external force is removed from the body the elastic part of the occurring strains will relax and the plastic part will remain permanently. The total strain can then be divided into an elastic and a plastic part:

$$\epsilon = \epsilon_{el} + \epsilon_{pl} \tag{7}$$

If the acting stress remains below the elastic limit all occurring strain are elastic and their dependence on the stress is linear. Because of the tensor nature of applied stress and occurring strain each component of the stress tensor depends on all components of the strain tensor and vice versa. They form a total of 81 linear equations [40].

$$\sigma_{ij} = c_{ijkl} \epsilon_{kl} \qquad \epsilon_{ij} = a_{ijkl} \sigma_{kl}, \qquad \text{with} \qquad \mathbf{A} = \mathbf{C}^{-1} \tag{8}$$

The equation shown above defines the fourth rank tensors of stiffness $\mathbf{C}$ and of compliance $\mathbf{A}$, both consisting of 81 elements. Due to the symmetries of σ and ϵ the relation $a_{ijkl} = a_{jikl} = a_{ijlk}$ holds for both tensors and reduces the independent elements from 81 to 36. Using these symmetry elements the two indexes ij of the tensor notation may be

combined into one index of the Voigt notation as shown in Table 1 [40]. In this notation

Table 1 – Transformation of the index from tensor to Voigt's notation.

$$
\begin{array}{lll}
11 \rightarrow 1 & 23 \rightarrow 4 & 32 \rightarrow 4 \\
22 \rightarrow 2 & 13 \rightarrow 5 & 31 \rightarrow 5 \\
33 \rightarrow 3 & 12 \rightarrow 6 & 21 \rightarrow 6
\end{array}
$$

σ and ϵ become vectors with six rows and $\mathbf{A}$ reduces to a second rank tensor (6x6). The tensor $\mathbf{A}$ in Voigt's notation is symmetric which is caused by additional symmetry properties linked to the elastic energy from stresses and strains, e.g. $a_{ijkl} = a_{klij}$. This reduces the number of independent elements to 21.

$$
\begin{pmatrix}
\epsilon_1 \\ \epsilon_2 \\ \epsilon_3 \\ \epsilon_4 \\ \epsilon_5 \\ \epsilon_6
\end{pmatrix}
=
\begin{pmatrix}
a_{11} & a_{12} & a_{13} & a_{14} & a_{15} & a_{16} \\
\cdot & a_{22} & a_{23} & a_{24} & a_{25} & a_{26} \\
\cdot & \cdot & a_{33} & a_{34} & a_{35} & a_{36} \\
\cdot & \cdot & \cdot & a_{44} & a_{45} & a_{46} \\
\cdot & \cdot & \cdot & \cdot & a_{55} & a_{56} \\
\cdot & \cdot & \cdot & \cdot & \cdot & a_{66}
\end{pmatrix}
\begin{pmatrix}
\sigma_1 \\ \sigma_2 \\ \sigma_3 \\ \sigma_4 \\ \sigma_5 \\ \sigma_6
\end{pmatrix}
\tag{9}
$$

Equation (9) shows Hooke's law in the notation of Voigt and all independent 21 components of the tensor $\mathbf{A}$. Depending on the crystal symmetry an additional reduction in the independent constants may appear or parts of the elements may be zero. The color-code used for underlining in the equation shows the example of a cubic symmetry. In this case all gray components are zero and the elements of the same color are identical which reduces the number of independent components to three. For isotropic materials additionally $a_{44} = 2(a_{11} - a_{12})$ holds which means there are only two independent components left. The color-code on the components are an example of the hexagonal symmetry. For this lattice type $a_{66} = 2(a_{11} - a_{12})$ holds universally.

Coordinate Systems and Transformations   between them are needed to describe all properties within their own orientations. In order to describe the physical relations properly, transformations between the different coordinate systems are necessary[40] .

Properties related to the crystal, for example the single-crystal compliances, are expressed in the so called crystal frame $\hat{C}$ in which the unit vectors are oriented along the (100), (010) and (001) crystal direction.

The different orientations of the grains and the applied load in loading experiments are expresses in the so called sample frame $\hat{S}$. The S_3-axes is oriented along the sample normal and the other two axis left are oriented along the symmetry directions of the surface of the sample.

In every experiment the physical properties are measured along a so called measurement
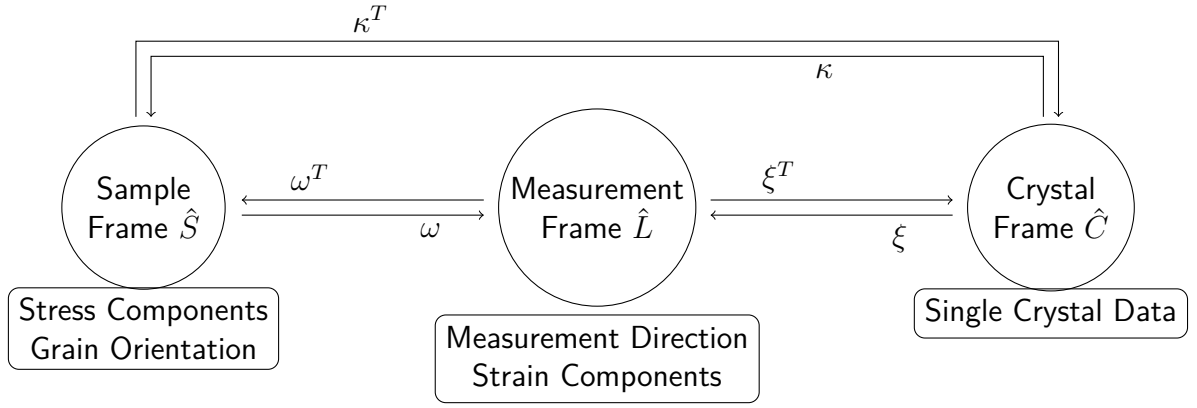
Figure 4 – Coordinate systems and their relative orientations [40]. During diffraction experiments the load is applied in the sample frame $\hat{S}$. The strain are measured in the measurement frame $\hat{L}$ and deformation itself is defined in the crystal frame $\hat{C}$. For the evaluation of the experiments all input and output data has to be synchronized to the same frame. The transformation between the frames is defined by their relative orientation to one another and is calculated with the transformation matrices ω, ξ and κ and their transposed.

direction $\mathbf{Q}$, also known as the scattering vector in diffraction experiments, which in most cases is not aligned to $\hat{C}$ or $\hat{L}$. The measurement frame $\hat{L}$ is oriented in such a way that L_3 is parallel to $\mathbf{Q}$ and L_2 is aligned parallel to the sample surface [40]. Figure 4 shows the different coordinate systems and the transformations between them.

Equation (10) shows the transformation matrix ω from the sample to the measurement frame. The first rotation ϕ is done around the S_3-axes and puts S_2 perpendicular to L_3. Then the coordinate system is rotated at the angle ψ around the S_2-axes to parallelize S_3 and $\mathbf{Q}$. The last rotation aligns $S_{1,2}$ with $L_{1,2}$. These angles are illustrated in Figure 5 on the right[8].

$$\omega = \begin{pmatrix} -\cos(\psi)\cos(\phi)\sin(\varphi) & -\cos(\psi)\sin(\phi)\sin(\varphi) & \sin(\psi)\sin(\varphi) \\ +\sin(\phi)\cos(\varphi) & +\cos(\phi)\cos(\varphi) & \\ -\cos(\psi)\cos(\phi)\cos(\varphi) & -\cos(\psi)\sin(\phi)\cos(\varphi) & \sin(\psi)\cos(\varphi) \\ +\sin(\phi)\sin(\varphi) & +\cos(\phi)\sin(\varphi) & \\ \sin(\psi)\cos(\phi) & \sin(\psi)\cos(\phi) & \sin(\psi) \end{pmatrix} \tag{10}$$

The second transformation matrix ξ is shown in equation (11). As illustrated in Figure 5 on the left the first rotation around the C_3-axes turns C_2 perpendicular to projection of L_3. The second rotation around C_2 rotates C_3 parallel to $\mathbf{Q}$. The last rotation aligns $C_{1,2}$ with
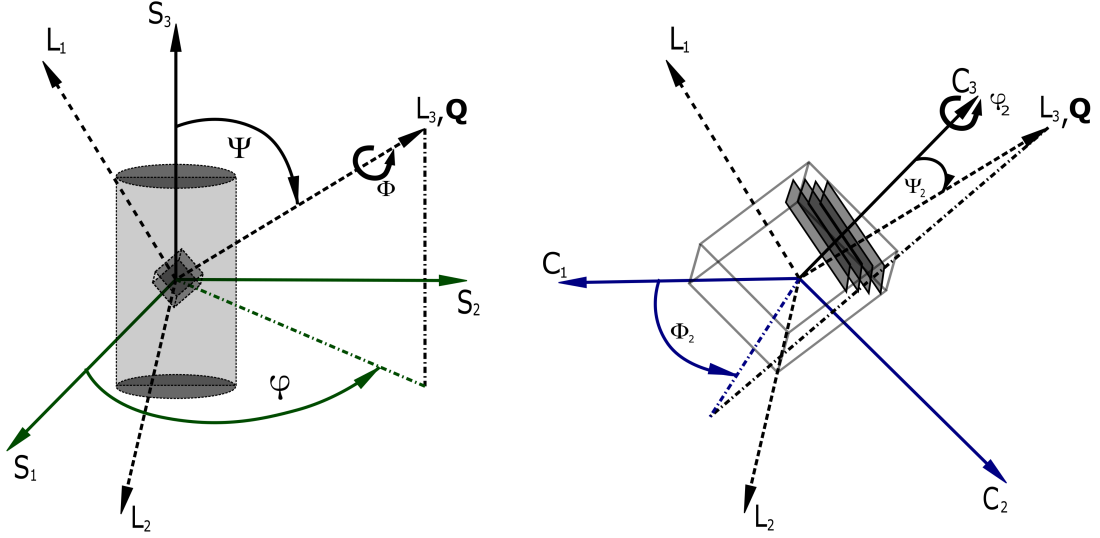
Figure 5 – The angular relation between the sample frame $\hat{S}$ and measurement frame $\hat{L}$ is shown on the left and on the right the relation between the crystal frame $\hat{C}$ and the measurement frame is shown. During single-axis loading test, as used during the tensile diffraction experiments the load is applied along L_3. The angles ϕ and ψ are adjusted by turning the complete load axis from the horizontal to a vertical position. Depending on the orientation of the crystallites during the diffraction experiment only certain grains will make a contribution. Their orientation is typically related to the orientation of the applied load [42].

$L_{1,2}$[8].

$$
\xi =
\begin{pmatrix}
-\cos(\varphi_2)\sin(\phi_2)\cos(\psi_2) & \cos(\varphi_2)\cos(\phi_2)\cos(\psi_2) & \cos(\phi_2)\sin(\psi_2) \\
+\cos(\varphi_2)\sin(\phi_2) & +\sin(\varphi_2)\sin(\phi_2) & \\
-\sin(\varphi_2)\sin(\phi_2)\cos(\psi_2) & \cos(\varphi_2)\sin(\phi_2)\cos(\psi_2) & \sin(\phi_2)\sin(\psi_2) \\
-\cos(\varphi_2)\cos(\phi_2) & \sin(\varphi_2)\cos(\phi_2) & \\
\sin(\varphi_2)\sin(\psi_2) & \cos(\varphi_2)\sin(\psi_2) & \cos(\psi_2)
\end{pmatrix}
\tag{11}
$$

In order to ensure the correct orientations of L_3 to the diffraction planes ($h\ k\ l$) the rotations in equation (10) and (11) are defined by the Euler angles $\{\varphi + \pi, \psi, \phi\}$ and $\{\varpi_2, \psi_2, \pi/2 - \phi_2\}$, respectively[8].

The last transformation κ from the crystal into the sample frame can be executed by successively applying the transformations ω and ξ.

4.2 Size Scales in Deformation

All deformations in solids can be split up into three different length scales, the overall sample, the grains and the atomistic level, i. e. macroscopic, mesoscopic and microscopic scale. In Figure 6 the different scales of deformation are shown. In general the force is applied to the sample aligned with the sample frame, shown in the top. In this case the elastic tensor $\overline{\mathbf{C}}_S$
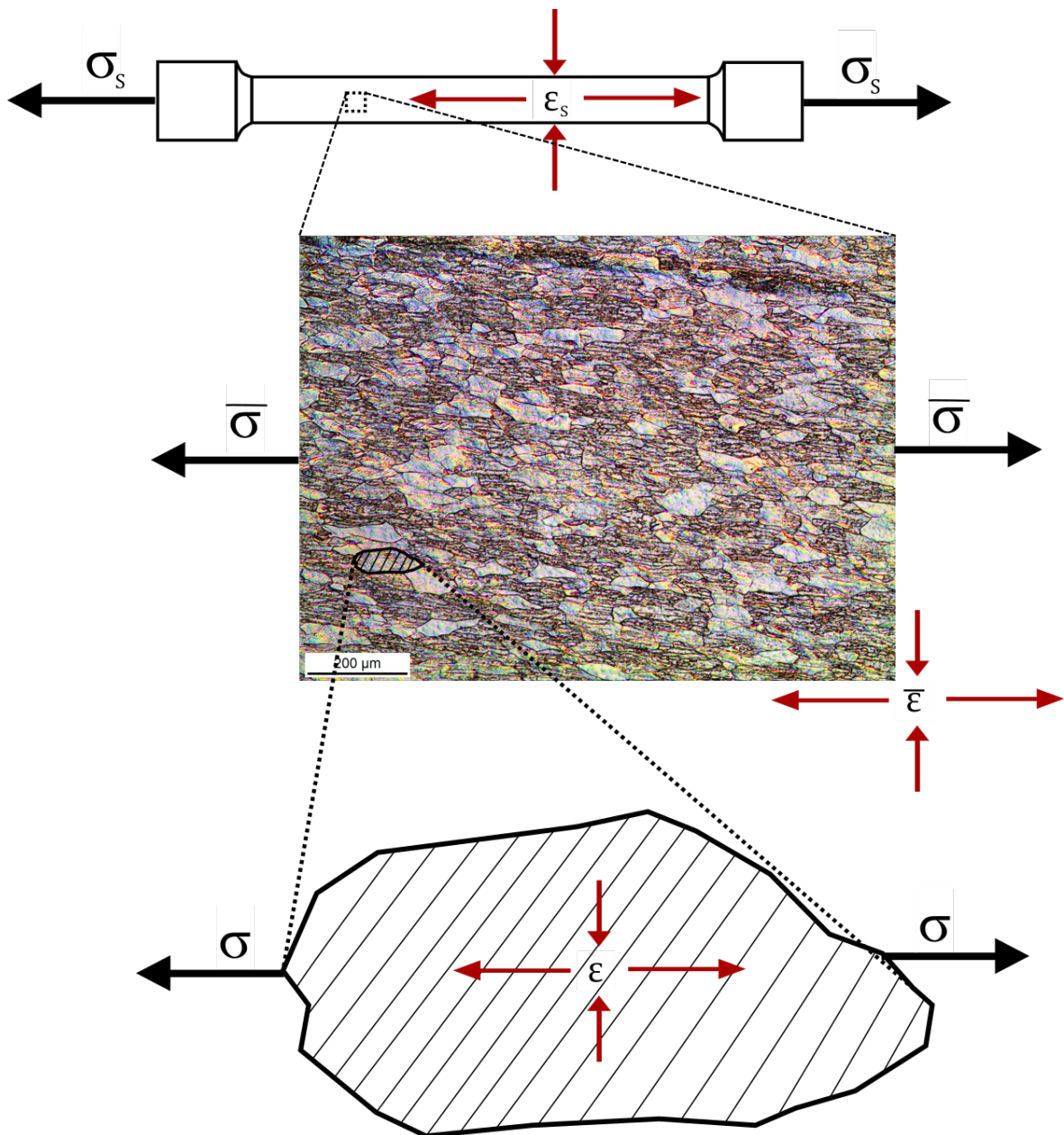
Figure 6 – All three length scales on which solids are deformed under external load. The macroscopic scale is indicated by σ_S and ϵ_S. The mesoscopic scale represents the average over a certain number of grains with different orientations and is denoted by $\bar{\sigma}$ and $\bar{\epsilon}$. The microscopic scale is a single grain in a specific orientation and denoted by σ and ϵ.

in Hooke's law is calculated by averaging the average single-crystal elastic constants $\overline{\mathbf{C}}_\alpha$ of the different phases.

For any sample orientation only those lattice planes are contributing to the scattering signal, i. e. the Bragg reflection, for which grains are oriented within the measurement geometry. This ensemble of grains is described in the measurement frame, therefore to correctly apply Hooke's law the elastic tensor $\overline{\mathbf{C}}_\alpha$ of one phase is calculated by averaging the single-crystal elastic constants over the different grain orientations and taking into account the orientation

distribution (texture). As described later, it is important to take other effects like the grain-to-grain interaction or the load transfer into account during the averaging on the mesoscopic scale.

The microscopic scale is illustrated at the bottom of Figure 6 and is aligned with the crystal frame. All single-crystal properties such as the single-crystal elastic constants, critical resolved shear stresses, dislocations and many other properties are described in this frame. The following list contains an overview over all used notations and their meaning

- For all of the second order tensor the same notations are used. The S in σ_S and ϵ_S indicates the sample. This means every component of these tensors is given in the sample frame and as they represent the sample, all averages of lower size scales are averaged again into the two tensors.

- The bar of $\bar{\sigma}$ and $\bar{\epsilon}$ indicates the grain level. Therefore the stress or strain of a defined ensemble of grains is averaged into the tensors. The distribution of the ensemble is chosen freely but follows specific rules depending on the properties the ensemble is representing. For example during tensile diffraction experiments the ensemble is chosen in a way that it represents every grain orientation meeting the diffraction condition.

- No indication on σ or ϵ means the tensor is defined in a single orientation. They represent the most basic unit and do not contain any average information. They can be viewed as a single-crystal domain along a specific orientation.

- All notations introduced, apply for all fourth-order tensors as well. Similar to the second order tensors, no indication **C** represent the conditions met in a single-crystal domain. The indication **C'** shows if the tensor is defined along any specific orientation with respect to the sample frame S.

- In the case of $\overline{\mathbf{C}}_\alpha$ the bar indicates that this tensor is averaged over an ensemble of tensors **C** along different orientations. Similar to the stress or strain tensors the ensemble is chosen depending on what they are representing, indicated by the lower letter. S represents the hole sample while greek symbols stand for different phases. During the averaging it is convenient to apply any texture weightings.

4.3 Diffraction based stress-strain analysis

In diffraction experiments only average values for the strains are measured. As described in 4.1 the measured values depend on the angles ψ and φ, e. g. **Q** and on the crystal orientation $\langle hkl \rangle$), giving $\epsilon(\mathbf{Q}, hkl) = \bar{\epsilon}$. In a similar way the average applied stress is the macroscopically applied stress, $\bar{\sigma} = \bar{\sigma}_S$.

As shown in equation (6) the macroscopic average of the strains and stresses is obtained by volume averaging over the total sample volume. This average can be applied to Hooke's law:

$$\overline{\epsilon} = \overline{\mathbf{A}\sigma} = \overline{\mathbf{A}}\overline{\sigma} \tag{12}$$

The average compliance tensor $\overline{\mathbf{A}}$ is calculated only over those orientations which are
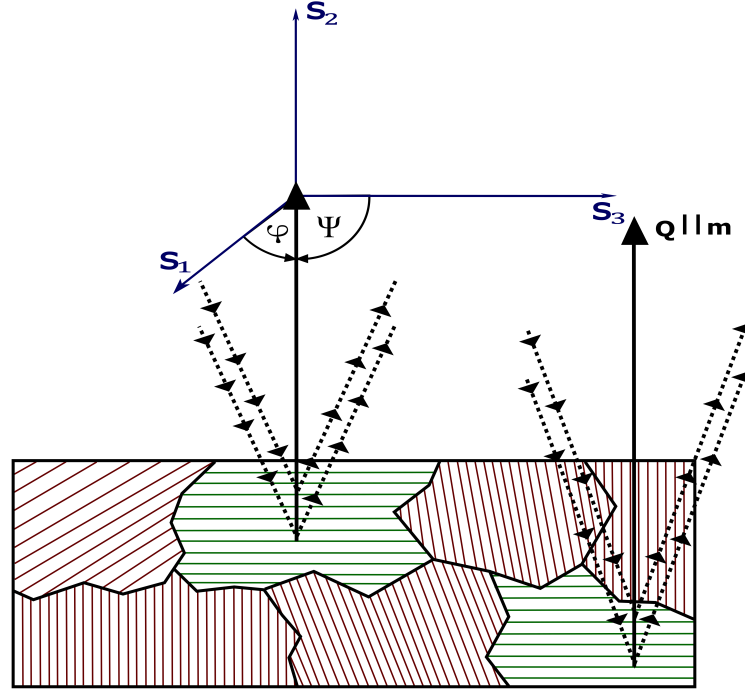
Figure 7 – The neutrons or X-rays involved in the scattering process are indicated by black dotted lines. The grains exhibiting green lattice planes are involved in the scattering process, which means that $\mathbf{Q}\|\mathbf{m}$. The grains marked by red lattice planes are not oriented along the direction to fullfill die scattering condition. The sample frame is shown in blue and determines the orientation angles ψ and φ.

contributing to the diffracted intensity during the experiment. A schematic view of an diffraction experiment is shown in Figure 7, only those lattice planes are contributing to the observed Bragg peak for which the plane normal $\mathbf{m}$ coincides with the scattering vector $\mathbf{Q}$.

$$\mathbf{A}'_{uwij}(g) = \xi_{um}(g)\xi_{wn}(g)\xi_{io}(g)\xi_{jp}(g)\mathbf{A}_{mnop} \tag{13}$$

$\overline{\mathbf{A}}$ is transformed from the crystal- to the measurement frame, $\mathbf{A}'(g)$ by the transformation matrix (11) leading to Equation (13). In this manner Equation (12) can be expresses as [40]:

$$\epsilon(\mathbf{Q}, \mathbf{m}) = \sum_{i,j} \mathbf{F}_{ij}\overline{\sigma}_{ij} + \epsilon^{pl}(\mathbf{Q}, \mathbf{m}) \tag{14}$$

4.3 Diffraction based stress-strain analysis

with the stress factor $\mathbf{F}_{ij}(\mathbf{Q}, \mathbf{m})$ given by:

$$\mathbf{F}_{ij}(\mathbf{Q}, \mathbf{m}) = \sum_{u,w} \frac{\int_{\mathbf{m}||\mathbf{Q}} \mathbf{A}'_{uwij}(g) m_u m_w f(g) \mathrm{d}g}{\int_{\mathbf{m}||\mathbf{Q}} f(g) \mathrm{d}g} \tag{15}$$

In most solids the grains are not randomly oriented. A quantitative measure of how many grains are oriented along a specific direction is given by multiples of random distributions (m. r. d.) combined into an Orientation Distribution Function (ODF) $f(g)$. To solve Equation (15) analytically different assumptions can be taken into consideration [40].

(i) No plastic strains are occurring, e. g. $\epsilon^{pl}(\mathbf{Q}, \mathbf{m}) = 0$

(ii) No texture, e. g. $f(g) = 1$

(iii) Elastic isotropy, e. g. the elastic properties do not depend on the lattice direction.

During the introduction of the elastic regime assumption (i) always applies except it is explicitly stated otherwise.

In Equation (14) the strains are measured along $\mathbf{Q}$ and expressed in the measurement frame. In this case, the only observed component of the strain tensor is ϵ_{33} and assuming (iii) it follows:

$$\epsilon_{33} = \frac{1}{2\pi} \sum_{i,j} \int_{\mathbf{m}||\mathbf{Q}} \mathbf{A}'_{33kl}(g) \mathrm{d}g \cdot \overline{\sigma}_{ij} \tag{16}$$

$$\overline{\mathbf{A}'^{r}} = \int_{\mathbf{m}||\mathbf{Q}} \mathbf{A}'(g) \mathrm{d}g \tag{17}$$

Equation (16) can be transformed with the knowledge of the rotation symmetry of the average tensor and the measurement direction in the measurement frame, yielding:

$$\epsilon_{33} = \overline{\mathbf{A}'^{r}}_{3311} \mathrm{tr}(\overline{\sigma}') + (\overline{\mathbf{A}'^{r}}_{3333} - \overline{\mathbf{A}'^{r}}_{3311}) \sum_{i,j} \overline{\sigma}_{ij} m'_i m'_j \tag{18}$$

Equation (18) can then be transformed into the specimen reference frame, which leads to the general equation of stress analysis [40]

$$\overline{\epsilon_{33}} = s_1(\sigma_{11} + \sigma_{22} + \sigma_{33}) + \frac{1}{2} s_2 \Big(\cos^2(\varphi)\sigma_{11} + \sin^2(\varphi)\sigma_{22}) \sin^2(\psi) + \sigma_{33} \cos^2(\psi) \Big) \tag{19}$$

with the diffraction elastic constants (DEC) $s_1(hkl)$ and $\frac{1}{2}s_2(hkl)$:

$$s_1(hkl) = \overline{\mathbf{A}'^{r}}_{3311} \tag{20}$$

$$\frac{1}{2} s_2(hkl) = \overline{\mathbf{A}'^{r}}_{3333} - \overline{\mathbf{A}'^{r}}_{3311} \tag{21}$$

The averaging in equation (20) and (21) can be solved analytically if the grains are randomly oriented in the measurement volume (ii), leading to the following equations with the

orientation paramters γ_i defined in table 2 [40] .

$$\overline{A'}^r_{3311} = \frac{1}{2}\gamma_m\gamma_n(\delta_{pq} - \gamma_p\gamma_q)\mathbf{A}_{mnpq} \tag{22}$$

$$\overline{\mathbf{A}'}^r_{3333} = \gamma_m\gamma_n\gamma_p\gamma_q\mathbf{A}_{mnpq} \tag{23}$$

If the material is further considered as elastically isotropic (iii), the integration in equation (20) and (21) becomes independent of the orientation distribution of the grains yielding the following equations for the DEC.

$$s_1(hkl) = \mathbf{A}_{1122}; \qquad \frac{1}{2}s_2(hkl) = 2(\mathbf{A}_{1111} - \mathbf{A}_{1122}) \tag{24}$$

Table 2 – The orientations parameters γ_i represent angles between the lattice direction and the crystal frame C.

γ_1	γ_2	γ_3
$\frac{h}{\sqrt{h^2+k^2+l^2}}$	$\frac{k}{\sqrt{h^2+k^2+l^2}}$	$\frac{l}{\sqrt{h^2+k^2+l^2}}$

4.4   Diffraction Elastic Constants

In classical stress analysis DECs are used to link measured strains to existing phase stresses and therefore calculate for example the residual stresses in a given sample via equation (19). The phase stress of phase α can be derived by measuring the strains of different orientations in φ and ψ.

$$\overline{\sigma}^\alpha = \frac{1}{d_0}\frac{1}{\frac{1}{2}s_2}\frac{\partial d(\varphi,\psi)}{\partial \sin^2(\psi)} \tag{25}$$

Equations (25) is for many cases linear and s_1 and $\frac{1}{2}s_2$ can be easily evaluated by the slope and by the point of intersection to the y-axis. In some cases the $d(\sin^2(\psi)$-distribution is non-linear due to texture effects or plasticity induced micro stresses. The texture effects are minimized by maximizing the grain statistics and increasing the number of orientations measured. It has been shown by different authors that in this case the influence of the texture in the derived DECs are small and negligible [28, 7]. In the case of micro stresses induced by large plasticity the evaluation has to be performed on lattice planes which are not or only insignificantly affected [40].

In multi-phase systems it is possible to derive the compound DEC $\frac{1}{2}s_2^C$, but its use for the evaluation of phase stresses is in this case limited. As described later in section 4.7, the phase stress $\overline{\sigma}^\alpha$ in a compounds is given by equation (53) and combined with equation (25)

the following relationship for compound DECs is derived [40].

$$\frac{1}{d_0} \frac{1}{\frac{1}{2}s_2^C} \frac{\partial d(\varphi, \psi)}{\partial \sin^2(\psi)} = \sigma^L + \frac{1}{\mathbf{f}^\alpha} \overline{\sigma}_0^\alpha \tag{26}$$

The microstresses $\overline{\sigma}_0^\alpha$ are caused by different different plastic or thermal behavior. The two cases where compound DECs may be used for the evaluation are given below. In all other cases the transition factors $\mathbf{f}^\alpha$ have to be taken into account for the evaluation.

   i $\overline{\sigma}_0^\alpha$ is very small or zero. In this case the compound DECs are the same as the single-phase DECs.

  ii The phase fraction of the measured phase is $> 95\%$ or the elastic difference is small, e. g. $\mathbf{f}^\alpha \approx 1$.

4.5 Elastic Grain-to-Grain Modeling

The single crystals forming a polycrystal are defining the respective elastic properties of the material. The physical interactions between the single crystals are essential for the derivation of the polycrystalline elastic properties, for example the macroscopic Young's or shear modulus. The DECs provide a link between the bulk properties and the lattice strains measured in diffraction experiments i.e. the DECs are related to the single-crystal elastic constants via grain-to-grain interactions. An overview of the most important relations between the bulk elastic parameter in isotropic materials is provided in table 3.
The assumption that all strains are homogeneously distributed as suggested by Voigt [9], $\mathbf{A} = \langle \mathbf{C} \rangle^{-1}$, leads to following expressions for the DECs for all crystal symmetries.

$$s_1 = \frac{x + 4y - 2z}{2(x - y + 3z)(x + 2y)}; \quad \frac{1}{2}s_2 = \frac{15}{2x - 2y + 6z} \tag{27}$$

$$x = c_{11} + c_{22} + c_{33}; \quad y = c_{12} + c_{13} + c_{23}; \quad z = c_{44} + c_{55} + c_{66}; \tag{28}$$

Equations (22) and (23) can directly be solved with the replacement of $\mathbf{A} = \mathbf{S}$ with the assumption of a homogeneous distribution of stress inside the grains [11], which is referred to as the Reuss approximation. In this approximation the elastic behavior is anisotropic and the equations for the DECs contain the orientation parameters, Γ and H, for different crystal symmetries, shown for cubic and hexagonal symmetries in table 4.

$$s_1 = s_{12} + (s_{11} - s_{12} - \frac{1}{2}s_{44})\Gamma \tag{29}$$

$$\frac{1}{2}s_2 = s_{11} - s_{12} - 3(s_{11} - s_{12} - \frac{1}{2}s_{44})\Gamma \tag{30}$$

Table 3 – Relations between the different bulk elastic parameters in isotropic materials to the single-crystal and diffraction elastic constants. A more detailed overview is provided by Behnken [40]

	E, ν	E, G	κ, G	c_{11}, c_{12}	
E	E	E	$\frac{9\kappa G}{3\kappa+G}$	$\frac{(c_{11}-c_{12})(c_{11}+2c_{12})}{c_{11}+c_{12}}$	Young's modulus Materials response to uniaxial tension or stress
G	$\frac{E}{2(1+\nu)}$	G	G	$\frac{c_{11}-c_{12}}{2}$	Shear modulus Materials response to shear stress
ν	ν	$\frac{E-2G}{2G}$	$\frac{3\kappa-2G}{6\kappa+2G}$	$\frac{c_{12}}{c_{11}+c_{12}}$	Poisson ratio Materials response orthogonal to applied stress
κ	$\frac{E}{3(1-2\nu)}$	$\frac{EG}{3(3G-E)}$	κ	$\frac{c_{11}+2c_{12}}{3}$	Bulk modulus Materials response to hydrostatic stress
s_1	$-\frac{\nu}{E}$	$\frac{2G-E}{2EG}$	$\frac{2G-3\kappa}{18\kappa G}$	$-\frac{c_{12}}{(c_{11}-c_{12})(c_{11}+2c_{12})}$	-
$\frac{1}{2}s_2$	$\frac{1+\nu}{E}$	$\frac{1}{2G}$	$\frac{1}{2G}$	$\frac{1}{c_{11}-c_{12}}$	-

Equations (29) and (30) show a linear relationship in the orientation for cubic symmetries and equations (31) and (32) a parabolic relationship in H^2 for hexagonal symmetries.

$$s_1 = \frac{1}{2}\left[s_{12}(1-H^2) + s_{13}H^2 + (s_{11}+s_{33}-2s_{13}-s_{44})(1-H^2)H^2\right] \qquad (31)$$

$$\frac{1}{2}s_2 = \frac{1}{2}[s_{11}(1-H^2)(2-3H^2) - s_{12}(1-H^2) + s_{13}(H^2(5-6H^2)-1) + s_{33}(3H^2-1)H^2 + 3s_{44}H^2(1-H^2)] \quad (32)$$

Table 4 – Orientation parameters for different crystal symmetries and there dependence on the γ_i

Crystal symmetry	Parameter	γ_i - dependence
cubic	3Γ	$3(\gamma_1^2\gamma_2^2 + \gamma_2^2\gamma_3^2 + \gamma_3^2\gamma_1^2)$
hexagonal	H^2	γ_3^2

Hill investigated the elastic behavior of aggregates and found that the assumptions of Voigt

and Reuss are leading to following conditions [14].

$$\kappa_r \leq \kappa \leq \kappa_v; \qquad G_r \leq G \leq G_v; \qquad E_r \leq E \leq E_v \tag{33}$$

Where κ, G and E are representing the bulk-, shear- and Young's modulus, respectively. The index r denotes the Reuss approximation, v Voigts approximation and no index the real value. He found empirically that the arithmetic or geometric average would "suggest themselves as good approximations" [14]. However, the arithmetic average was widely referred to as Hill approximation in literature, therefore this work sticks to the same reference. Hill focused in his work on the bulk properties and their characteristics, while Matthies investigated both the single-crystal and bulk properties in combination and found that a simple arithmetic mean, indexed by a, leads to an inequality in the averaged elastic compliances derived for Reuss and Voigt as shown below [28].

$$\overline{\mathbf{S}(g)}^a = \overline{\mathbf{S}}^{\text{Reuss}} \neq \overline{\mathbf{S}}^{\text{Voigt}} = [\overline{\mathbf{C}}^{\text{Voigt}}]^{-1} = [\overline{\mathbf{C}(g)}^a]^{-1} \tag{34}$$

The arithmetic average of both approximations shown in Equation (34) leads to the following conditions:

$$
\begin{aligned}
\overline{\mathbf{S}}^{\text{Hill(S)}} &= \frac{\overline{\mathbf{S}}^{\text{Reuss}} + \overline{\mathbf{S}}^{\text{Voigt}}}{2}; \qquad \overline{\mathbf{C}}^{\text{Hill(C)}} = \frac{\overline{\mathbf{C}}^{\text{Reuss}} + \overline{\mathbf{C}}^{\text{Voigt}}}{2} \\
\overline{\mathbf{S}}^{\text{Hill(S)}} &= [\overline{\mathbf{C}}^{\text{Hill(S)}}]^{-1}; \qquad \overline{\mathbf{C}}^{\text{Hill(C)}} = [\overline{\mathbf{S}}^{\text{Hill(C)}}]^{-1} \\
\overline{\mathbf{S}}^{\text{Hill(S)}} &\neq \overline{\mathbf{S}}^{\text{Hill(C)}}; \qquad \overline{\mathbf{C}}^{\text{Hill(C)}} \neq \overline{\mathbf{C}}^{\text{Hill(S)}}
\end{aligned}
\tag{35}
$$

To avoid the dependence of operation sequence, e. g. calculating from **S** or **C**, Matthies suggested a geometric mean which can be formerly interpreted as [28].

$$\overline{\mathbf{S}}^{\text{Matthies}} = \{[\overline{\mathbf{S}}^{\text{Hill(S)}}\overline{\mathbf{S}}^{\text{Hill(C)}}]^{\frac{1}{2}}\}$$

$$\tag{36}$$

$$\overline{\mathbf{C}}^{\text{Matthies}} = \{[\overline{\mathbf{C}}^{\text{Hill(S)}}\overline{\mathbf{C}}^{\text{Hill(C)}}]^{\frac{1}{2}}\}$$

It is easily shown that equation (36) obeys $\overline{\mathbf{S}}^{\text{Matthies}} = [\overline{\mathbf{C}}^{\text{Matthies}}]^{-1}$.

Besides the approaches by Voigt, Reuss and the different averages between these models, there exist self-consistent approaches based on the inclusion model developed by Eshelby. Kroener started from the assumptions of a grain ensemble in a solid which is distributed in a way that all macroscopic forces applied to it will distribute homogeneously. From this one can calculate a valid average stress tensor $\overline{\sigma}$ and accordingly the connected average strain tensor $\overline{\epsilon}$ over the whole volume. These average values will differ from the values obtained for a single grain depending on its orientation g and shape and may be described by a linear

relationship [16].

$$\sigma(g) = \mathbf{p}(g)\bar{\epsilon}$$
$$\epsilon(g) = \mathbf{q}(g)\bar{\sigma}$$

(37)

The relationship between the fourth-rank tensors $\mathbf{p}(g)$ and $\mathbf{q}(g)$ may be derived by applying Hooke's law to $\sigma(g)$ and $\bar{\epsilon}$.

$$\mathbf{p}(g) = \mathbf{C}(g)\mathbf{q}(g)\overline{\mathbf{C}}$$

(38)

With the assumption of spherical grains equation (37) is integrated over all orientations. The obtained average values of the strain $\bar{\epsilon}'$ and stress $\bar{\sigma}'$ for the grains may deviate to some extend from the average value over the whole ensemble of grains.

$$\bar{\sigma} = \bar{\sigma}' + \alpha = \mathbf{C}\bar{\epsilon}$$
$$\bar{\epsilon} = \bar{\epsilon}' + \beta = \mathbf{S}\bar{\sigma}$$

(39)

Without defining α and β it is obvious that if $\bar{\sigma} > \bar{\sigma}'$ then $\bar{\epsilon} > \bar{\epsilon}'$ or vice versa. Combined with equations (37) and (39) these define upper and lower borders for sample stiffnesses via the following conditions [16]:

$$\overline{\mathbf{p}}' < \overline{\mathbf{C}} < \overline{\mathbf{q}}', \quad \text{or} \quad \overline{\mathbf{p}}' > \overline{\mathbf{C}} > \overline{\mathbf{q}}'$$

(40)

Equation (37) can then be rewritten into the following equation:

$$\sigma(g) = (\mathbf{C} + \mathbf{r}(g))\bar{\epsilon}$$
$$\epsilon(g) = (\mathbf{S} + \mathbf{t}(g))\bar{\sigma}$$

(41)

And since equation (12) and its inverse must hold, $\mathbf{r}(g)$ and $\mathbf{t}(g)$ or their grain averages $\mathbf{r}'(g)$ and $\mathbf{t}'(g)$ averaged over all orientations are vanishing [16].

$$\int \mathbf{r}'(g)\mathrm{d}g = 0; \qquad \int \mathbf{t}'(g)\mathrm{d}g = 0;$$

(42)

$\mathbf{r}(g)$ and $\mathbf{t}(g)$ are representing the difference in single-crystal elastic constants for the average grain of a polycrystal to those of an average oriented grain. Therefore both can be physically interpreted as an "elastic susceptibility" or in combination with the primitive volume as "elastic polarizability" [15].

In case of an anisotropic sphere with the single-crystal elastic constants $\mathbf{C}_1$ in an isotropic

medium with constants $\mathbf{C}_2$ the polarization $\mathbf{r}(g)$ and $\mathbf{t}(g)$ can be derived analytically [16].

$$
\begin{aligned}
r'(g) &= \mathbf{C}_1(g) - \mathbf{C}_2 + \mathbf{C}_1(g)\mathbf{u}(g) \\
t'(g) &= \mathbf{u}(g)\mathbf{S}_1(g) \\
\mathbf{u}(g) &= -\mathbf{v}^{-1}(g)[\mathbf{C}_1(g) + \mathbf{C}_2] \\
\mathbf{v}(g) &= \mathbf{C}_1(g) - \mathbf{C}_2 + \mathbf{C}_2\mathbf{w}
\end{aligned}
\tag{43}
$$

With the Eshelby's tensor $\mathbf{w}$.

To derive the bulk properties the integration in (42) has to be calculated. For $\mathbf{r}'(g)$ this leads to a fourth order polynomial for the shear modulus.

$$
G^4 + aG^3 + bG^2 + cG + d = 0 \tag{44}
$$

$$
a = \frac{3\kappa + 2\nu}{4}; \qquad b = \frac{9\kappa^2 + 12\kappa\nu - 8\kappa\mu - 96\mu\nu}{64}
$$

$$
c = -\frac{(3\kappa + 52\nu)\mu\kappa}{64}; \qquad d = -\frac{6\kappa^2\mu\nu}{64}
$$

And to a third order polynomial for $\mathbf{t}'(g)$ [16].

$$
G^3 + \alpha G^2 + \beta G + \gamma = 0 \tag{45}
$$

$$
\alpha = \frac{3\kappa + 4\nu}{8}; \qquad \beta = -\frac{(\kappa + 12\nu)\mu}{8}; \qquad \gamma = -\frac{\kappa\mu\nu}{4}
$$

$$
\kappa = c_{11} + 2c_{12}; \qquad \mu = c_{44}; \qquad \nu = \frac{c_{11} - c_{12}}{2}
$$

Later Gairola derived together with Kroener the effective shear modulus G describing the polycrystal in terms of a comparison medium G_0 i.e the matrix [43].

$$
G = \frac{\alpha_2 G_0^2 + \beta_2 G_0 + \gamma}{G_0^2 + \alpha_1 G_0 + \beta_1} \tag{46}
$$

$$
\alpha_1 = \frac{3}{40}(15\kappa' + 12\nu + 8\mu); \qquad \alpha_2 = \frac{1}{5}(2\nu + 3\mu)
$$

$$
\beta_1 = \frac{3}{20}\kappa'(3\nu + 2\mu); \qquad \beta_2 = \frac{3}{40}(6\kappa'\nu + 9\kappa'\mu + 20\nu\mu); \qquad \gamma = \frac{3}{4}\kappa'\nu\mu
\tag{47}
$$

Where the bulk moduli where set to $\kappa' = \frac{1}{3}\kappa$. If the shear modulus of the effective medium is set to the same as the comparison medium, $G_0 = G$, equation (45) with $\alpha = \alpha_2 - \alpha_1$ and $\beta = \beta_2 - \beta_1$ will be recovered [30].

De Wit modified the constant in (47) by introducing the orientation parameter Γ from table 4 into equations (47) α_1 and β_1.

$$
\alpha_1 = \frac{3}{8}(3\kappa' + 4[\mu + 3(\nu - \mu)\Gamma]; \qquad \beta_1 = \frac{3}{4}\kappa'[\mu + 3(\nu - \mu)\Gamma]
\tag{48}
$$

The DECs are the same for Kroener's and de Wit's model.

$$S_1 = \frac{1}{9\kappa'} - \frac{1}{6G}; \qquad \frac{1}{2}S_2 = \frac{1}{G} \tag{49}$$

4.6 Derivation of Single-Crystal Elastic Constants

To obtain the single-crystal elastic constants from reverse stress analysis a minimization problem must be addressed which includes the elastic constants as fitting parameters. The χ^2-minimization technique offers a straight forward fitting procedure with enough flexibility and performance to be further modified for the use inside a self-consistent calculation scheme to incorporate multi-phase analysis. There exist two different approaches to define the χ^2-function.

The diffraction elastic constants are offering the first possibility for the definition of the χ^2-function as suggested by Gnäupel-Herold et al. [8].

$$\mathbf{S}(hkl, a_{ijkl}) = \begin{pmatrix} S_1(hkl, a_{ijkl}) \\ 1/2 S_2(hkl, a_{ijkl}) \end{pmatrix} \tag{50}$$

By defining $\mathbf{S}$ as a two dimensional vector the χ^2-function can be defined in the following way:

$$\chi^2(a_{ijkl}) = \sum_i^n \left[\frac{S_1(hkl)_{\mathsf{meas}} - S_1(hkl, a_{ijkl})_{\mathsf{calc}}}{\sigma(S_1(hkl)_{\mathsf{meas}})} \right]^2 + \left[\frac{\frac{1}{2}S_2(hkl)_{\mathsf{meas}} - \frac{1}{2}S_2(hkl, a_{ijkl})_{\mathsf{calc}}}{\sigma(\frac{1}{2}S_2(hkl)_{\mathsf{meas}})} \right]^2 \tag{51}$$

In this case the DECs $\mathbf{S}_{\mathsf{meas}}$ are fitted from the experimental data and minimized to calculated ones $\mathbf{S}_{\mathsf{calc}}$ from the single-crystal elastic constants by selecting a grain-to-grain interaction model.

The strains $\overline{\epsilon_{33}}$ directly offer the second possibility to define the χ^2-function, leading to following expression:

$$\chi^2(a_{ijkl}) = \sum_i^k \left[\frac{\overline{\epsilon_{33}}(hkl)_{meas} - \overline{\epsilon_{33}}(hkl, a_{ijkl})_{calc}}{\sigma(\overline{\epsilon_{33}}(hkl)_{meas})} \right]^2 \tag{52}$$

In principle both techniques are leading to the same results with an important difference. Equation (51) is a more specialized form of (52), which leads to a great reduction in the summation terms of χ^2, e. g. $n >> k$ because the S_i are combined values from the different measurement directions and only depend on the scattering planes.
In both cases the texture is taking into account by applying additional weightings to equation

(51) and (52) based on the respective m.r.d. values of the crystal orientations involved during the experiment. In case of the DECs the m.r.d. weightings are first applied during the fitting process for each scattering plane involved during the measurement, then for each DEC a total weighting factor is calculated and applied in equation (51). For the strain based minimization function the weightings are applied during the calculation of the integral in the denominator of equation (15). This leads to a higher impact of strains measured on lattice planes involving more grains during the scattering process [42].

4.7   Load Transfer

In materials containing more than one phase the grain-to-grain interaction models discussed earlier are not covering the interactions between the different phases, figure 8. In the case the phases have significantly different rigidity the stress appearing in the sample distributes differently among those phases. As a result only the effective stiffness of the corresponding phase is observed during diffraction experiments. The difference between the elastic properties are a measure for the difference between the effective and single phase values and lead to large differences in the stress distribution among the phases as shown in figure 9 [42]. Additionally, depending on the microstructure micro stresses are appearing between the phases directly influencing the apparent phase stresses which act effectively on one phase. This means that the phase stresses consist of a macro stress dependent and an independent part:

$$\overline{\sigma}^\alpha = \overline{\sigma}_0^\alpha + \mathbf{f}^\alpha [\sigma^L + \sigma^I] \tag{53}$$

Where $\overline{\sigma}^\alpha$ is the overall average phase stress of phase α, $\overline{\sigma}_0^\alpha$ is the independent part, σ^I is the residual stress, σ^L is the applied load and $\mathbf{f}^\alpha$ is a 4th rank tensor similar to the elastic constants and its components are the stress transition factors [40].

$$\mathbf{f}_{ijkl}^\alpha = \frac{\partial \overline{\sigma}_{ij}^\alpha}{\partial (\sigma^L + \sigma^I)_{kl}}; \text{with} \quad \sum_{\alpha=1}^n p^\alpha \mathbf{f}^\alpha = \mathbf{I} \tag{54}$$

$\mathbf{f}^\alpha - \mathbf{I}$ is measure for the difference of elasticity of the phases and is therefore called elastically induced and $\mathbf{I}$ representing the unity tensor. It represents the micro stress dependent part and therefore directly quantifies $\overline{\sigma}^{II}$.

$$\overline{\sigma}^{II} = \overline{\sigma}_0^\alpha + [\mathbf{f}^\alpha - \mathbf{I}][\sigma^L + \sigma^I] \tag{55}$$

To derive an expression for the stress transition factors in dependence of the elastic properties of the sample and containing phases one starts with Eshelby's inclusion model from equation (41). The stress in the inclusion σ_E, is derived by the equivalent stress free
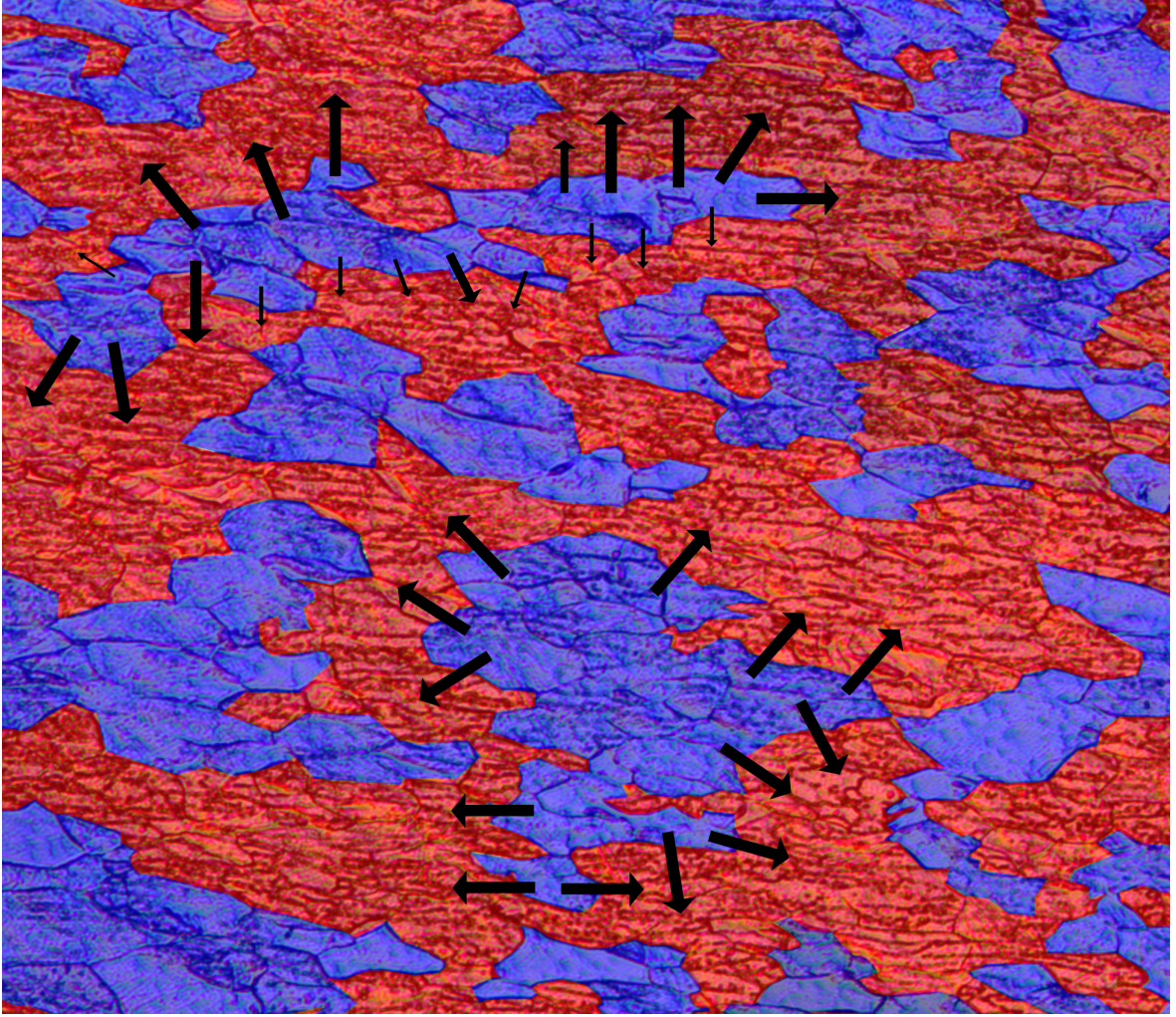
Figure 8 – Schematic illustration of a multi-phase system where the elastic properties of one phase are different from the other. In this case the load is distributed from the blue to the red phase. The amount of transferred stress depends on the elastic properties as well as microstructure of the phases.

transformation ϵ^T.

$$\epsilon^T = -[(\overline{\mathbf{C}}_E - \overline{\mathbf{C}}_M)(\mathbf{w}^{-1} + p(\mathbf{w}^{-1} - \mathbf{I})) + \overline{\mathbf{C}}_M]^{-1}(\overline{\mathbf{C}}_E - \overline{\mathbf{C}}_M)\bar{\epsilon} \tag{56}$$

$$\sigma_E = -\overline{\mathbf{C}}_S(\mathbf{w}^{-1} - \mathbf{I})[(\overline{\mathbf{C}}_\alpha - \overline{\mathbf{C}}_S)\mathbf{w}^{-1} + \overline{\mathbf{C}}_S]^{-1}(\overline{\mathbf{C}}_\alpha - \overline{\mathbf{C}}_S)\bar{\epsilon} + \overline{\mathbf{C}}_S\bar{\epsilon} \tag{57}$$

Where the index m represents the matrix, and s indicates the sample averages. The transition factors are derived by redefining the inclusion as α-phase and the elastic constants of the matrix by homogeneous elastic constants of the sample in equation (57) and comparison of Hooke's law with equation (54) [40].

$$\mathbf{f}^\alpha = -\overline{\mathbf{C}}_S(\mathbf{w}^{-1} - \mathbf{I})[(\overline{\mathbf{C}}_\alpha - \overline{\mathbf{C}}_S)\mathbf{w}^{-1} + \overline{\mathbf{C}}_S]^{-1}(\overline{\mathbf{C}}_\alpha - \overline{\mathbf{C}}_S)\overline{\mathbf{S}}_S + \mathbf{I} \tag{58}$$
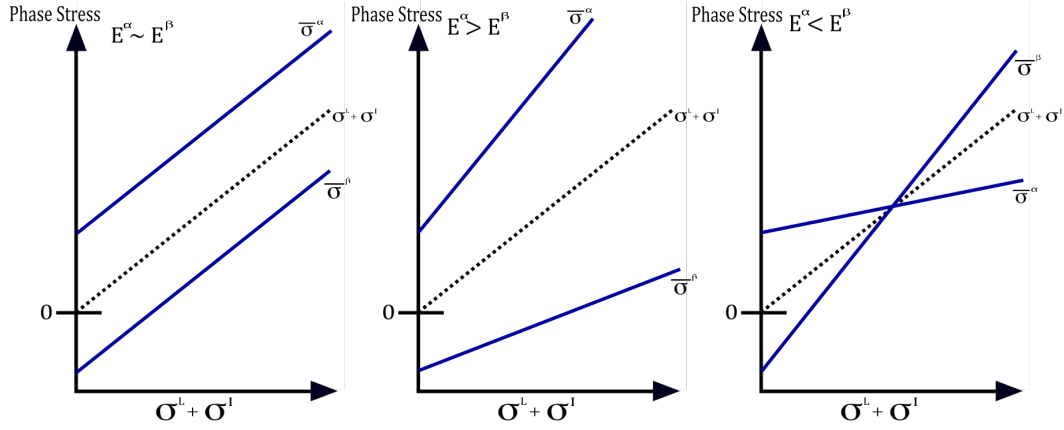
Figure 9 – The effective phase stress as a function of the applied macro stress $\sigma^L + \sigma^I$ for different elastic properties of the phases [40]. Depending on the Young's modulus for raising phase stress the difference in stress between the phases is varying but the average stress remains constant. The three examples above illustrate the stress distribution among the phases for varying compliances of the phases.

Where **w** is the Eshelby's tensor defined in equation (59) for a sphere in a homogeneous matrix .

$$\mathbf{w}^{-1}_{1111} = \frac{7 - 5\nu}{15(1 - \nu)}; \quad \mathbf{w}^{-1}_{1122} = \frac{-1 + 5\nu}{15(1 - \nu)}; \quad \mathbf{w}^{-1}_{1212} = \frac{4 - 5\nu}{15(1 - \nu)} \tag{59}$$

4.8 Elastic Anisotropy

Anisotropic behavior mainly depends on the crystal symmetry and gets more complicated for lower symmetries. This means that different physical properties depend on the orientation of the crystal, like mechanical properties, elasticity, the development of plastic deformation, cracking, thermal expansion, residual stress distribution and many others. An example of this is shown in figure 10 where the Young's modulus is shown for a varying anisotropy. For $A = 1$ the Young's modulus is equal in any direction and the plot shows a circle. A quantification of the anisotropy for all crystal symmetries is not straightforward. Different approaches have been developed by Zener, Chung et al., Ledbetter et al., Ranganathan et al., Tromans and Kube [13, 36, 44, 37, 38, 39].

For cubic symmetry lattices Zener defined the ratio of the maximum and minimum values of the oriented shear moduli as the anisotropy index A [13]. An illustration of the Young's modulus along different crystallographic directions for a wide range of A is given in figure 10.

$$A = \frac{2c_{44}}{c_{11} - c_{12}} \tag{60}$$

The crystal behaves elastically isotropic for $A = 1$, which means the resistance to shear on $[100]$ in $\langle 0kl \rangle$ equals the resistance on $[110]$ in $\langle -110 \rangle$ [13].

The adaption of equation (60) to lower symmetries causes difficulties. As illustrated in equation 9 in hexagonal crystal symmetries five independent single-crystal elastic constants
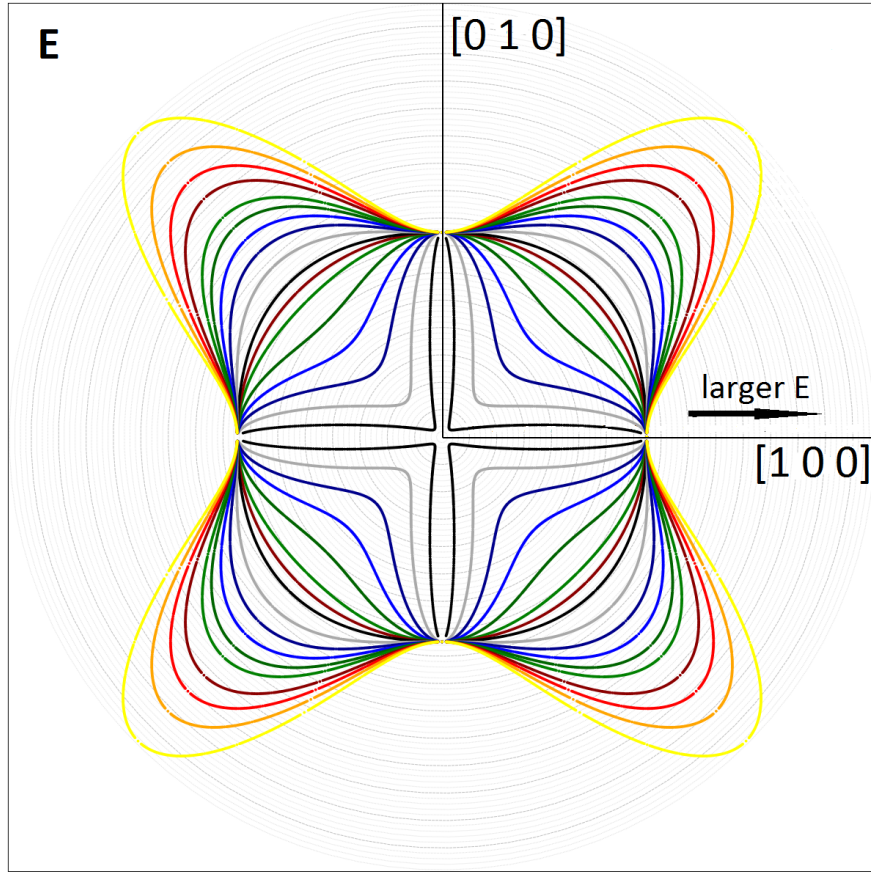
Figure 10 – The Young's modulus E is shown for the [1 0 0] × [0 1 0] plane. For $A = 1$ the Young's modulus is equal in any direction and the plot shows a circle. A is continously growing from black to yellow showing large differences for changing anisotropies. The lines pointing inwards represent theoretical values of if E for anisotropies smaller than one.

exist resulting in more than two independent shear moduli. Thus, the additional degrees of freedom in those system invalidates the application of the Zener anisotropy

Chung et al. suggested the difference of the two limiting shear moduli given by Voigt G_V and Reuss G_R as a measure for the elastic anisotropy and defined the dimensionless quantity A^C.

$$A^C = \frac{G_V - G_R}{G_V + G_R} = \frac{3(A-1)^2}{3(A-1)^2 + 25A} \tag{61}$$

Howerver, equation (61) can also be applied only to cubic symmetries. A^C is always positive and zero for elastic isotropy [36].

Ledbetter et al. generalized equation (60) to all symmetries by solving Christoffel's equations (62) for the minimum and maximum shear wave velocities, v_1 and v_2.

$$\det(\mathbf{C}_{ijkl}n_i n_l - \rho v^2 \delta_{jk}) = 0 \tag{62}$$

Where the components of the wave propagation vector are denoted by n_i. Applying the relationship of the single-elastic constants to the mass density ρ and the shear wave velocity,

equation (63) is obtained.

$$A^L = \frac{v_2^2}{v_1^2} \tag{63}$$

A^C and A^L lack universality, since A^C is only defined for cubic crystal and per definition $A^L > 1$ and therefore does not cover cubic crystals with $A < 1$ such as alkali halides like CsF or KCl [37]. Ranganathan et al. introduced an anisotropy measure A^U which accounts for the tensor nature of the elastic properties by taking into account the shear and bulk modulus

$$A^U = 5\frac{G^V}{G^R} + \frac{\kappa^V}{\kappa^R} - 6 \tag{64}$$

$A^U \geq 0$ and equals zero if the crystal is locally isotropic. In the case of cubic crystal symmetry A^U may be expressed in terms of A or A^C to enable a comparison between the different anisotropy measures.

$$A^U = \frac{6}{5}\left(\sqrt{A} - \frac{1}{\sqrt{A}}\right)^2 = 10\left(\frac{A^C}{1 - A^C}\right) \tag{65}$$

4.9   Stress-Strain Behavior for Single Crystals

The following section describes the stress-strain behavior of polycrystals beyond the elastic limits. The approach introduced here is based on Hill's formalism of deformation theory reworked into a self-consistent calculation scheme by Hutchinson, the Elasto-Plastic Self-Consistent Modeling (EPSC). For this approach basically the common theory of single-crystal deformation is expanded to describe large strains in polycrystals by dividing the deformation into piecewise linear fractions which are calculated self-consistently step by step.

Slip Systems   build the basis of all modern theories of plasticity. It is assumed that plastic deformation in single-crystals is caused by slip of different crystallographic planes in certain directions without disturbing the lattice geometry. The combination of a plane with a certain slip direction is called slip-system and all symmetrically equivalent planes and direction are summed up into so called slip families. In ideal single crystals the close packed planes are activated along the direction with the lowest number of obstacles, i.e atoms in glide direction. Therefore only certain slip families are activated depending on the crystal structure.

In face centered cubic   lattices only one slip family is activated during loading, the close packed planes in close packed directions $\{111\}\langle110\rangle$, as shown in Figure (11). This family consist of four planes each associated with three possible slip directions making a total of 12 slip systems summarized in table 5, each may be activated in positive or negative direction.
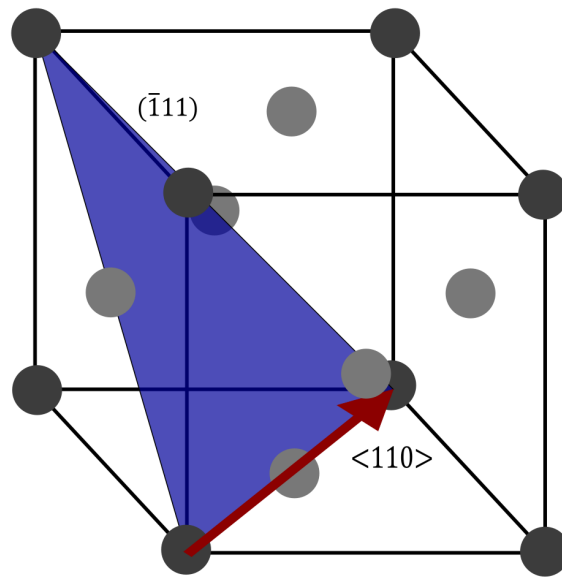
Figure 11 – f.c.c. crystals only contain one slip family along the closed packed planes (111) in the closed packed directions $\langle 110 \rangle$.

Table 5 – The four slip planes with their three associated slip directions for the $(111)\langle 110 \rangle$ slip family.

Plane	Directions		
(111)	$[1\bar{1}0]$	$[01\bar{1}]$	$[\bar{1}01]$
$(\bar{1}11)$	$[110]$	$[101]$	$[01\bar{1}]$
$(1\bar{1}1)$	$[110]$	$[10\bar{1}]$	$[011]$
$(11\bar{1})$	$[1\bar{1}0]$	$[101]$	$[011]$

In body centered cubic   structures some uncertainties exist with respect to which slip planes are activated during plastic deformation [21]. Taylor proposed that in this crystal structure the exact knowledge of every possible slip system is not necessary to correctly model the macroscopic deformation and now it is commonly accepted that slip may occur on any plane associated with any of the four $\langle 111 \rangle$ slip directions. In Figure 12 two glide planes with the lowest Miller indices (110) and (211) which define the basic slip families are shown. In both cases there exist three symmetry equivalent planes in four different direction leading to a total of 48 slip system summarized in the two slip families $\{110\}\langle 111 \rangle$ and $\{211\}\langle 111 \rangle$. A full table of all 24 slip systems is given in 6. There exist many other slip planes associated with the slip direction $\langle 111 \rangle$ but most of them can be obtained by superposition of the (110) and (211) planes. This is in particular true for the slip plane $(321) = (110) + (211)$ which is a closed packed plane as well.

Hexagonal systems   act similar to f.c.c., close packed planes slip in close packed directions. These planes are divided into three categories.

- Pyramidal planes (hkn) are divided into two sub-categories: Type 1 planes where
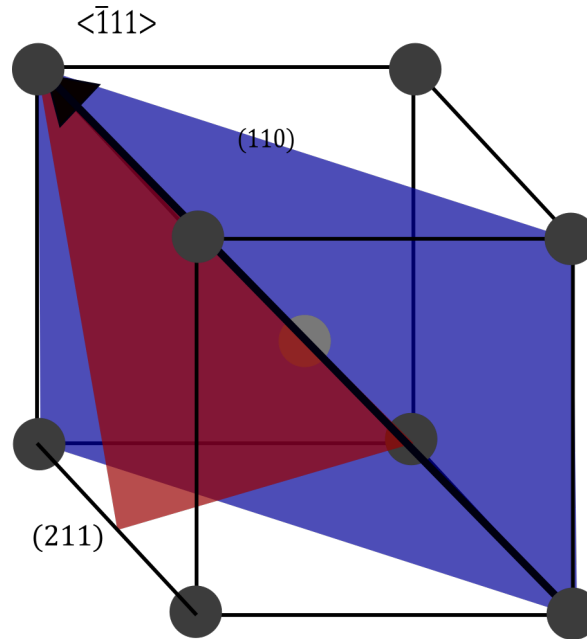
Figure 12 – For b.c.c. crystal structures all slip planes with an associated slip direction in any of the four $\langle 111 \rangle$ directions are commonly accepted. The main slip plains are (110) and (211)

Table 6 – The detailed slip systems of the two main slip families $\{110\}\langle 111 \rangle$ and $\{211\}\langle 111 \rangle$.

Plane	Direction	Plane	Direction	Plane	Direction	Plane	Direction
(110)	$[1\bar{1}1]$	(110)	$[\bar{1}11]$	(110)	$[111]$	$(1\bar{1}0)$	$[11\bar{1}]$
$(10\bar{1})$	$[111]$	$(10\bar{1})$	$[1\bar{1}1]$	(101)	$[11\bar{1}]$	(101)	$[\bar{1}11]$
(011)	$[111]$	(011)	$[\bar{1}11]$	$(0\bar{1}1)$	$[111]$	$(0\bar{1}1)$	$[\bar{1}11]$
(112)	$[11\bar{1}]$	(121)	$[1\bar{1}1]$	(211)	$[\bar{1}11]$	$(11\bar{2})$	$[111]$
$(1\bar{2}1)$	$[111]$	$(\bar{2}11)$	$[111]$	$(1\bar{1}2)$	$[\bar{1}11]$	$(12\bar{1})$	$[\bar{1}11]$
$(21\bar{1})$	$[1\bar{1}1]$	$(\bar{1}12)$	$[1\bar{1}1]$	$(\bar{1}21)$	$[11\bar{1}]$	$(2\bar{1}1)$	$[11\bar{1}]$

either $h = 0$ or $k = 0$ and type 2 where both $h \neq 0$ and $k \neq 0$.

- Basal planes $(00l)$ behave in the same way as the basal planes in f.c.c. structures.

- Prism planes are defined by $l = 0$ and are divided into type 1 planes $(h\bar{h}0)$ and type 2 planes $(hh0)$.

The basal plane consists of one slip plane which may be activated in three directions. For prism type 1 three planes may be activated in six directions and for type 2 one plane may be activated in three directions. The pyramidal type 1 consists of six planes in six different directions and type 2 consists of three planes in one direction.

The Slip Initiation   process is started when the resolved shear stress on a crystallographic plane i reaches a critical yield stress or yield strength τ_c^i associated with the given system in
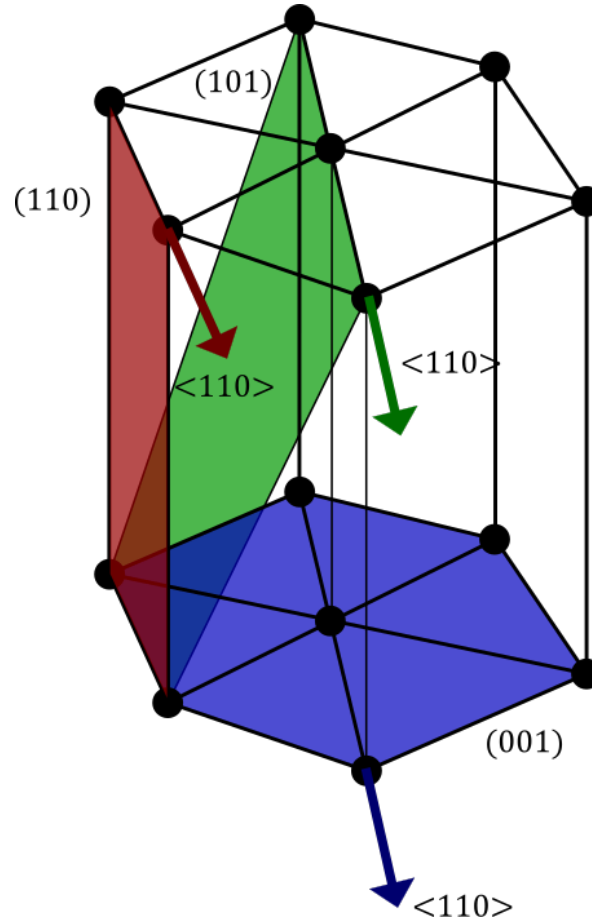
Figure 13 – For hexagonal crystal structures similarly to f.c.c. slip occurs on close packed planes along close packed direction. The three different types of slip planes are illustrated: basal $(00l)$ in blue, prism type $(h\bar{h}0)$ in red, $(hh0)$ and pyramidal (hkn) in green.

the slip direction. The resolved shear stress τ_r^i on a given slip system i is the resolved force divided by the slip plane area. As shown in Figure 14 in the case of a uni-axial tensile force applied along the tensile axis, τ_r can be written as:

$$\tau_r = \frac{F}{A}\cos(\phi)\sin(\lambda) \tag{66}$$

Where $\cos(\phi) \cdot \sin(\lambda)$ is known as the Schmid factor. Commonly the components of the second-order stress tensor σ described in section 4.1 are non zero.

$$\alpha_{kl}^i = \frac{1}{2}(\mathbf{m}_k^i\mathbf{n}_l^i + \mathbf{m}_l^i\mathbf{n}_k^i) \tag{67}$$

In this case τ_r^i is calculated with the so called resolving parameter α. Where $\mathbf{n}^i$ is normal to the slip plane i and $\mathbf{m}^i$ its slip direction [22].

$$\tau_r^i = \sigma\alpha^i \tag{68}$$
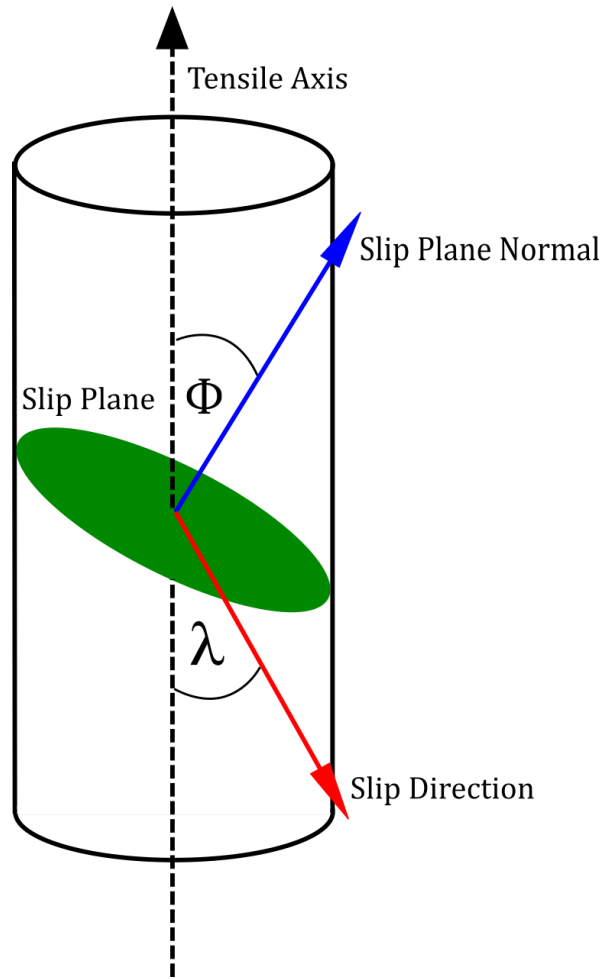
Figure 14 – Slip occurs when the applied stress on the slip plane reaches a critical value in slip direction

To calculate plastic deformation first a set of slip systems is chosen from all possible systems by checking if $\tau_r^i = \tau_c^i$. If this condition is satisfied the slip systems may load or unload depending which condition is satisfied [22].

$$\begin{aligned}
\dot{\sigma}\alpha^i &= \dot{\tau}_c^i; & \dot{\gamma} &\geq 0 & \text{loads} \\
\dot{\sigma}\alpha^i &< \dot{\tau}_c^i; & \dot{\gamma} &= 0 & \text{unloads}
\end{aligned} \tag{69}$$

For an inactive system $\tau_r^i < \tau_c^i$ with $\dot{\gamma} = 0$.

Plastic deformation is driven by the sum of the contribution of the shear rates $\dot{\gamma}^i$ of every active slip system.

$$\dot{\epsilon}_p = \sum_i \dot{\gamma}^i \alpha^i \tag{70}$$

Slip Hardening   is a process which arises from condition equations (69). It is obvious for the yield τ_c^i to change during plastic deformation, i.e. it "hardens". The rate of change $\dot{\tau}_c^i$ is

positive and a function of the shear rate $\dot{\gamma}^i$ and is called the generalized law of hardening.

$$\dot{\tau}_c^i = \sum_j \mathbf{h}^{ij} \dot{\gamma}^i \tag{71}$$

Equation (71) accounts for observations on latent hardening and double slip and allows hardening of one system by the glide of another system. Latent hardening describes the hardening of a slip system even if the system itself is not activated and double slip occurs if more than one slip system is active at the same time. Due to the linearity of equation (71) coupling remains the same independent of the number of activated glide systems. There exist different types of hardening defining the shape of the matrix $\mathbf{h}$ [20].

- **Perfect plasticity** occurs if all components of $\mathbf{h}$ are zero.

- **Isotropic hardening** occurs when all components of $\mathbf{h}$ are equal.

- **Independent hardening** occurs if the only non-zero components of $\mathbf{h}$ are the diagonal elements.

- **Kinematic hardening** occurs if $\mathbf{h}_{ij} = h \cdot \alpha^i \alpha^j$

By adding the elastic part to equation (70) the general stress-strain relation (72) is obtained.

$$\dot{\epsilon} = \mathbf{A}\dot{\sigma} + \sum_i \dot{\gamma}^i \alpha^i \tag{72}$$

Given that in $\mathbf{h}$ all principal minors of all orders do not vanish, equation (72) can be explicitly expressed by a piecewise-linear function [20].

$$\dot{\sigma} = \mathbf{L}\dot{\epsilon} \tag{73}$$

$\mathbf{L}$ is piecewise constant and relates $\dot{\epsilon}$ and $\dot{\sigma}$ uniquely together if $\mathbf{h}$ is positive semi-definite. In the case of no active systems it is obvious that $\mathbf{L} = \mathbf{A}^{-1}$ follows. For plastic deformation every branch of $\mathbf{L}$ results from the shear rate $\dot{\gamma}^i$ defined by the set of active slip systems. Each non-zero shear rate satisfies the conditions given by equations (71) and (70). Defining N relations for every non-zero shear rate [22].

$$\sum_j \dot{\gamma}^j X^{ij} = \alpha^i \mathbf{C}\dot{\epsilon}; \qquad \text{with} X^{ij} = \mathbf{h}^{ij} + \alpha^i \mathbf{C}\alpha^j \tag{74}$$

The shear rates are not always uniquely defined for a given state of stress, however it is always possible to find at least one set of shear rates for which all constitutive relations are satisfied [20].

$$\dot{\gamma}^i = \mathbf{f}^i \dot{\epsilon}; \qquad \mathbf{f}^i := \sum_k \mathbf{Y}^{ik} \mathbf{C}\alpha^k; \text{with} \quad \mathbf{Y} = \mathbf{X}^{-1} \tag{75}$$

In consequence the number of active slip systems defines $\mathbf{L}$.

$$\mathbf{L} = \mathbf{C}(\mathbf{I} - \sum_m \alpha^m \mathbf{f}^m) \tag{76}$$

If $\mathbf{h}$ is positive definite and the shear rates are unique an inverse $\mathbf{M}$ of $\mathbf{L}$ always exists. In the case of isotropic hardening $\mathbf{h}$ is only semi positive semi-definite. Therefor $\mathbf{L}$ happens to be singular and its inverse $\mathbf{M}$ does not exist. This restricts the stress rate into certain regions of the stress rate space.

4.10   Stress-Strain behavior for polycrystals

The general idea to describe the deformation behavior of polycrystals is to average the single-crystal behavior over a sufficient number orientations. This concept was first introduced by Hill and he proved in case of a sufficient large collection of single-crystals that the influence of the applied loading on the predicted crystal behavior becomes negligible, i. e. the macroscopic elastic moduli remain the same independent if the deformation behavior is calculated from a uniform straining or homogeneously applied stress [45]. Matthies later estimated the lower limit of statistical relevance during the averaging to a couple thousand grains [29].

$$\dot{\overline{\sigma}} = \overline{\mathbf{L}}\dot{\overline{\epsilon}} \qquad \dot{\overline{\epsilon}} = \overline{\mathbf{M}}\dot{\overline{\sigma}}, \quad \text{with} \quad \overline{\mathbf{M}} = \overline{\mathbf{L}}^{-1} \tag{77}$$

$\overline{\mathbf{L}}$ and $\overline{\mathbf{M}}$ depend on the entire collection of $\mathbf{L}$ and $\mathbf{M}$ and will therefore vary continuously along with the given stress or strain rate. The strict non-linear stress-strain behavior arises the problem to maintain a uniform straining for certain stress inputs and the consistency of the proposed model in selecting a particular branch of $\overline{\mathbf{L}}$ or $\overline{\mathbf{M}}$ among an infinite number of branches [22]. However, Hill proposed a self-consistent modeling which naturally sticks to particular branch of $\overline{\mathbf{L}}$ or $\overline{\mathbf{M}}$ with the restriction that changes in the used stress or strain rates remain below a certain limit [45].

To simplify further explanation, a specific deformation history is assumed from which one specific stress or strain state is selected for each grain. This defines the set of active slip systems and $\mathbf{L}$ and therefore the corresponding stress-strain curve of each single-crystal as shown in the previous section. Hill proposed each of these aligned and ellipsoidal crystallites to be embedded into an homogeneous matrix with moduli $\overline{\mathbf{L}}$ of the poly crystal as shown in figure 15 [18, 22]. The inclusion theory of Eshelby predicts the stress and strain rates to be uniform and relates them to macroscopic rates $\dot{\overline{\sigma}}$ and $\dot{\overline{\epsilon}}$ with two fourth order tensors $\mathbf{A}$ and $\mathbf{B}$ [15].

$$\dot{\epsilon} = \mathbf{A}\dot{\overline{\epsilon}}, \qquad \dot{\sigma} = \mathbf{B}\dot{\overline{\sigma}} \tag{78}$$

In order to more closely define the transition tensors $\mathbf{A}$ and $\mathbf{B}$ it is necessary to quantify the discrepancies between the stress and strain rates of the inclusions and the matrix.

$$\dot{\bar{\sigma}} - \dot{\sigma} = \mathbf{L}^*(\dot{\bar{\epsilon}} - \dot{\epsilon}), \qquad \dot{\bar{\epsilon}} - \dot{\epsilon} = \mathbf{M}^*(\dot{\bar{\sigma}} - \dot{\sigma}) \tag{79}$$

The "constraint tensor" $\mathbf{L}^*$ and its inverse $\mathbf{M}^*$ are defined to be ellipsoidal voids of the same alignment contained by the matrix. Under these conditions the constraint tensor only depends on the shape, orientation of the inclusion and $\overline{\mathbf{L}}$. Hutchinson gave formulas for $\mathbf{L}^*$ in the Appendix of his work in 1970 [22]. From equations (73), (77), (78) and (79) direct expressions for $\mathbf{A}$ and $\mathbf{B}$ are directly accessible.
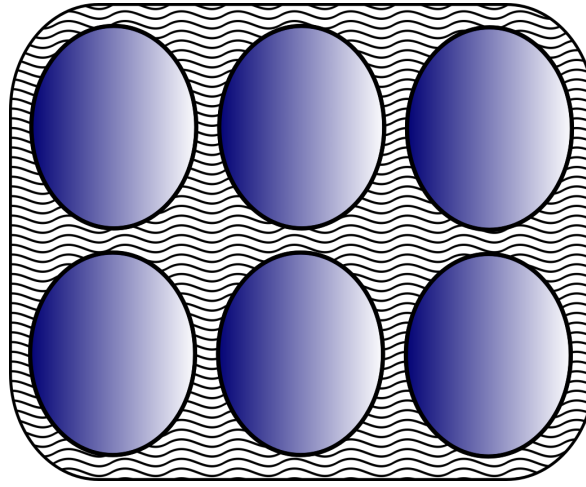
Figure 15 – The figure shows the ellipsoidal inclusions of the grains as suggested by Hill. All are equally aligned in the Matrix. The same shape and alignment is considered for voids assumed for L^*

$$\mathbf{A} = (\mathbf{L}^* + \mathbf{L})^{-1}(\mathbf{L}^* + \overline{\mathbf{L}}) \qquad \mathbf{B} = (\mathbf{M}^* + \mathbf{M})^{-1}(\mathbf{M}^* + \overline{\mathbf{M}}) \tag{80}$$

As stated before the average of the single-crystal collection defines the behavior of the poly crystal. In this scope a similar statement for $\overline{\mathbf{L}}$ is derived from the equations (73), (77) and (78).

$$\overline{\mathbf{L}} = \overline{\mathbf{LA}} \qquad \overline{\mathbf{M}} = \overline{\mathbf{MB}} \tag{81}$$

In order to derive $\overline{\mathbf{M}}$, $\mathbf{M}$ of every single-crystal contained by the collection must be derived. In case of a singular $\mathbf{L}$ its inverse does not exist and $\mathbf{M}$ is not available at this point in stress-strain space, therefore the use of $\mathbf{L}$ a more straight forward solution to predict the stress-strain behavior. But as shown earlier both ways lead to an identical solution.

In case of two-phase composite materials are straightforward adapted. In this case the grains of every constituent phase are calculated individually with use of the overall moduli of the combined material. The averages in equation (81) are adapted according the phase ratio of

the composite.

$$\overline{\mathbf{L}} = c_1 \cdot \overline{\mathbf{L}_1 \mathbf{A}_1} + c_2 \cdot \overline{\mathbf{L}_2 \mathbf{A}_2} \qquad \overline{\mathbf{M}} = c_1 \cdot \overline{\mathbf{M}_1 \mathbf{B}_1} + c_2 \cdot \overline{\mathbf{M}_2 \mathbf{B}_2} \tag{82}$$

The same principle applies to $\mathbf{A}$ and $\mathbf{B}$ from equation (78).

$$\mathbf{A}_i = (\mathbf{L}^* + \mathbf{L}_i)^{-1}(\mathbf{L}^* + \overline{\mathbf{L}}) \qquad \mathbf{B}_i = (\mathbf{M}^* + \mathbf{M}_i)^{-1}(\mathbf{M}^* + \overline{\mathbf{M}}) \tag{83}$$

5 Experimental

The measurement of the elasto plastic properties requires diffractometric tensile or compression tests. Section 4 shows in detail the theoretical background and the arising requirements to successfully perform the measurements. In general any diffractometer is suited for the experiments provided it has the necessary resolution to distinguish the peak shifts, $\frac{\Delta d}{d}$, between the load steps and enough intensity to ensure the statistical significance of the obtained strain values, i. e. to ensure the strains measured represent the average strain along a specific crystallographic direction. In the following part of this section four diffractometers are introduced which were used during the diffraction studies.

The elastic properties vary over the crystallographic direction and therefore the reversal of the classical stress analysis requires accurate strain values along different directions, i. e. shifts measured for a given bragg peak (hkl) at a specific load step. The minimum amount needed to specify all independent single-crystal elastic constants of a given phase depends on the symmetries given by its crystal structure. Effectively, for each independent component of the elastic tensor an corresponding equation has to be solved.

The diffraction elastic constants require to measure the strains for different ψ angles, the angle between the measurement direction and the load axis. In the case of most neutron instruments the Debye-Scherrer cones are to large to be captured completely by a single detector. However, because of the large scattering angles the peak shifts are in many cases more pronounced. To align the ring segment accordingly a rotateable tensile rig is used. Its compact design makes it highly flexible and easy to ship, a detailed description is given in a later section. The large dimensions of typical neutron beams allow sampling a large number of grains even for coarse grain materials. On the other hand, high-energy synchroton beamlines allow the collection of complete Debye-Scherrer cones in very short time interval albeit with very small beam sizes.

The total number of measured strain values depend on the number of orientations n_{or} and the number of load steps n_{ls} at which diffraction patterns are collected. The total number of Bragg peaks measured is equal to $n_{or} \cdot n_{ls}$ therefore the largest gain in statistics is achieved if both numbers match because the statistical significance increases quadratically. The most efficient measurements are performed between three to five different ψ orientations and load steps depending on the grain size, texture and crystal structure.

A summary of all investigated samples is provided at the end of this section. It contains a detailed description of the sample composition and all instruments which where used during the experiments including all settings. For each sample a detailed experimental procedure is given which contains all relevant information on the measured orientations and load steps.

5.1 High-Resolution Neutron Powder Diffractometer SPODI

The powder diffractometer SPODI located at the Heinz Maier-Leibnitz Zentrum (MLZ) in Garching near Munich is a high-resolution thermal neutron diffractometer optimized for structural studies of complex systems.
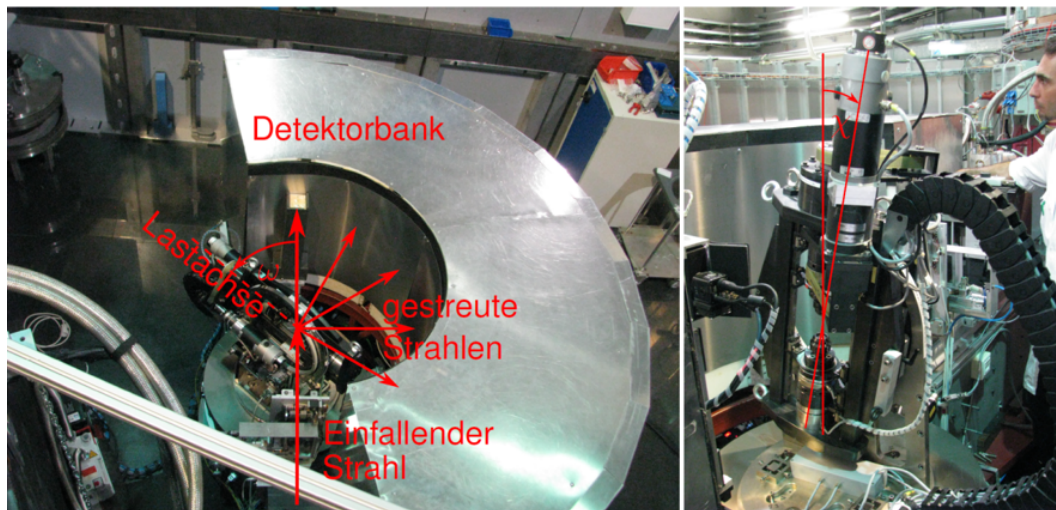
Figure 16 – Experimental setup at SPODI showing the scattering geometry and the mounted tensile rig. On the left a top down view is shown. The ω angle is defined by the angle of the load axis and the outgoing beam. On the right the tensile rig is shown in tilted position. The χ angle is defined to be $90°$ when horizontal and $180°$ when vertical.

Figure 16 shows photos of the tensile rig mounted onto the instrument and figure 17 illustrates a schematic of the instrument SPODI. The neutrons are generated at the source and then transported via a neutron guide to the monochromator. Depending on the take-off angle and selected diffraction plane of the germanium monochromator crystals the wavelength is selected. The monochromator is 200 mm high and consists of a stack of 15 germanium wafer crystals with 551 planes parallel to the surface with a mosaicity of $20'$ and $11'$ in horizontal and vertical direction, respectively. The standard take-off angle is $155°$ with a monochromator-to-sample distance of 5 m. At that angle three different wavelengths of 1.548 Å, 2.536 Åand 1.111 Å can be selected for the diffraction planes Ge(551), Ge(331) and Ge(771) [46]. The evacuated beam tube between the monochromator and sample contains slits which control the beam shape and divergence at the sample. From the sample the neutrons are scattered into the detector consisting of 80 ^{3}He detector tubes covering $160°$ around the sample with a total height of 300 mm. Fixed Soller collimators are mounted in front of every detector tube allowing a $10'$ horizontal divergence. This multi detector setup requires a stepwise data aquisition. Typically the position is varied in $0.05°$ per step which requires a recording of 40 individual steps for a complete diffraction pattern. This detector setup causes a higher data collection time for comparable statistics, but offers a very high resolution over wide scattering angle as shown in Figure 18. An example of the
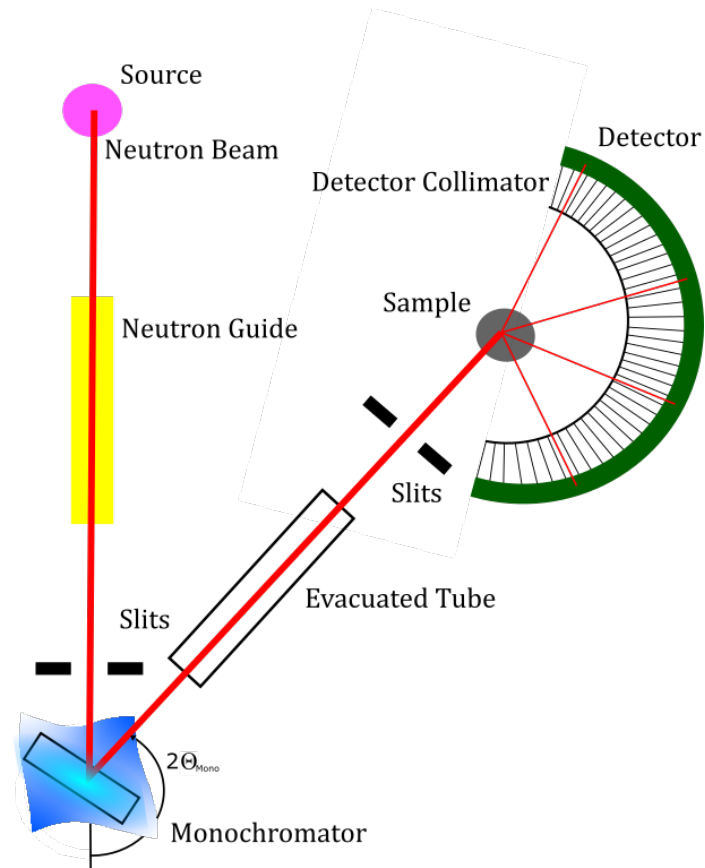
Figure 17 – Illustration of SPODI. The neutrons are generated at the source, are transported to the monochromator through a neutron guide. The wavelength of neutrons is set via the monochromator angle $2\Theta_{Mono}$. The neutrons are approaching the sample and are scattered into the detector.

2D data acquired during a typical experiment on SPODI is shown in Figure 19 [46].
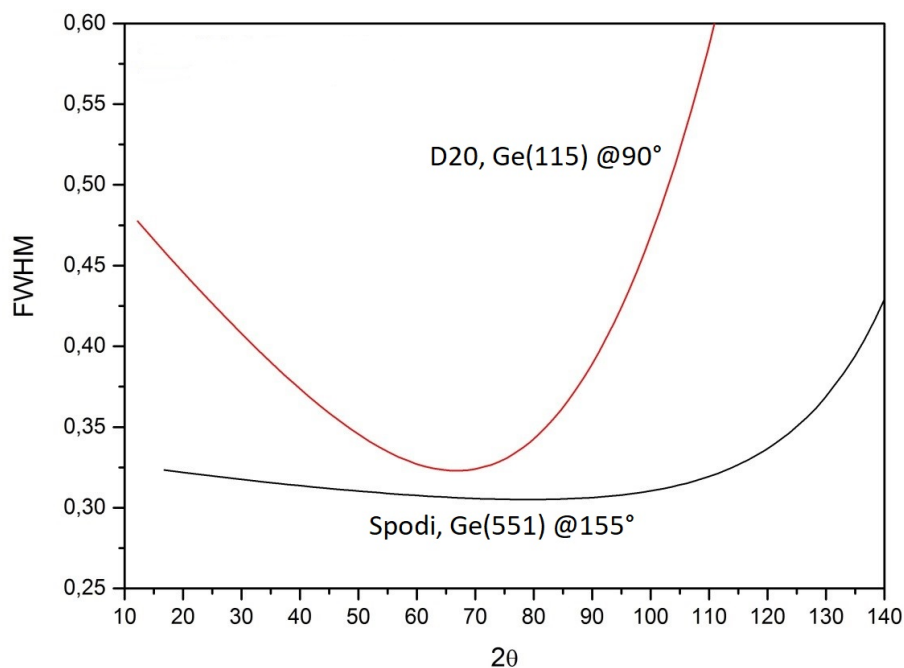
Figure 18 – Illustration of the resolution function of SPODI and D20 at ILL. The FWHM of SPODI is indicated in black for a take-off angle of $155°$ and the Ge(551) Monochromator. It remains nearly constant over the detection range. In red the resolution of D20 is shown and shows a good resolution compared to its significant higher neutron flux.
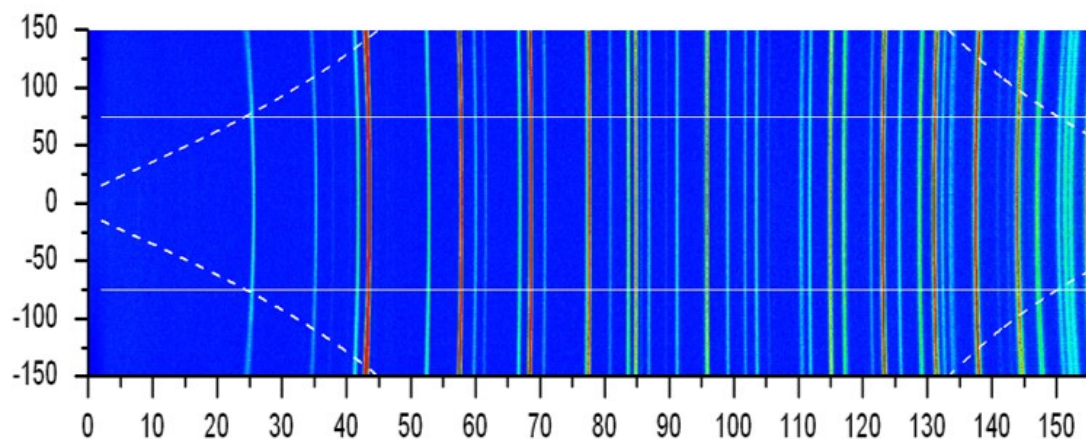
Figure 19 – The collected 2D-Data from SPODI. Only parts of the Debye Scherrer rings are collected during a measurement.

5.2 Materials Science Diffractometer STRESS-SPEC

The materials science diffractometer STRESS-SPEC is build for non-destructive material investigations with diffraction methods. With it's flexible design it can be equally applied for phase specific residual stress, texture analysis as well as phase analysis.
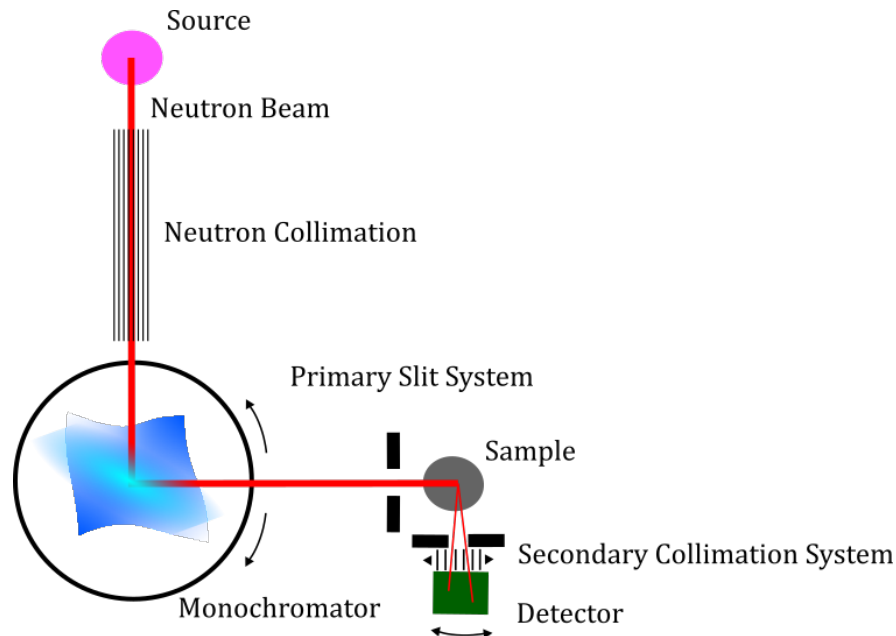
Figure 20 – Illustration of STRESS-SPEC. The neutrons are generated at the source, are passing the primary slit system, then scattered at the sample and then detected after the secondary slit system.

From the source the neutrons are collimated to the monochromator as shown in Figure 20. For the experiments three different monochromator crystal setups are available: Ge (511), Si (400) and PG. The take-off angle $2\Theta_{Mono}$ influences the wavlength and intensity of the neutron beam and is given by the angle of the sample to the monochromator. The resolution of the instrument is defined by the horizontal divergence, the variation of the wavelength $\frac{\Delta\lambda}{\lambda}$ and $2\Theta_{Mono}$. The Take-Off angle can be varied between $35°$ and $110°$ which allows high flexibility in intensity and resolution. The neutrons are passing the primary slit system before the sample and the secondary slit system after being scattered from the sample [47]. The slit systems define the gauge volume measured in the sample and can be varied from 1x1x1 mm^3 to 5x5x20 mm^3. The definition of a fixed gauge in sample during the measurements is important for the reproducibility of the geometrical alignment for strain and texture studies. The two dimensional ^{3}He detector has an active area of 200x200 mm^2 with a spatial resolution of about 1.5x1.5 mm^2. A radial oscillating collimator is mounted in front of the detector. This diminishes scattering from the sample environment and has no effect on the "accuracy" of the instrument. The instrumental resolution is given in Figure 22 for the different monochromator setups. A typical picture of the collected data is given in Figure (21). Due to the measurement geometry and size of the detector only approximately
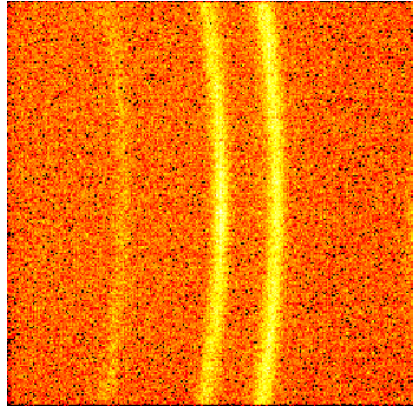
Figure 21 – The collected 2D-Data from STRESS-SPEC. Only parts of the Debye Scherrer rings are collected during a measurement and the angular coverage is approximately $16°$.
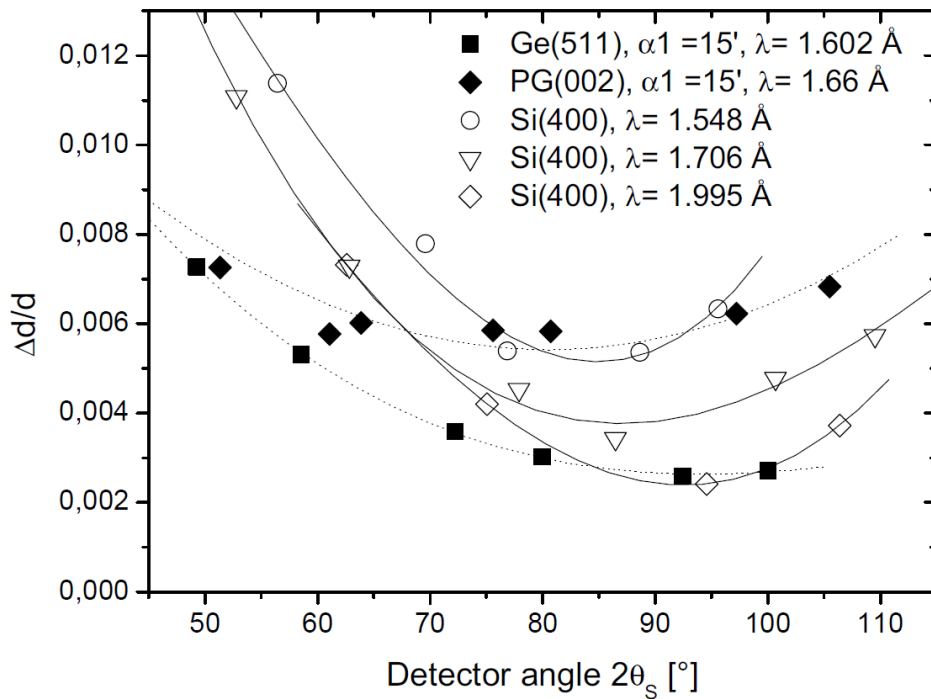
Figure 22 – The crsolution of STRESS-SPEC for different wavelength and monochromator setups.

$16°$ are covered during the diffraction experiment. As illustrated in figure 20 The detector is able to move around the sample retaining a constant scattering angle of $90°$ during the measurement. Therefore the vertical divergences do not affect the spatial resolution and the gauge volume remains near the ideal cubic shape [47].

The instruments setup is optimized to measure texture and strains along crystallographic directions. The constant scattering angle aligns the tensile angle χ with ψ which allows a straightforward evaluation of the experimental data and to measure the extension of every (hkl) peak for $\psi = 0$. However, the alignment of χ to ψ is only valid for a short interval in the scattering angle 2Θ on the detector and therefore limits its covering range to about

$15°$. Unless the peaks are in close proximity to one another every peak has to be measured separately increasing the beam time for the experiments.

5.3 High-Intensity Neutron Powder Diffractometer D20

The high efficiency neutron diffractometer D20 is located at the Institute Laue-Langevin (ILL). It operates at a maximum neutron flux of $10^8 \frac{\text{neutrons}}{\text{scm}^2}$. A large curved linear position sensitive detector provides the fastest counting rate, at a given resolution, among any other reactor based two-axis diffractometer [48].
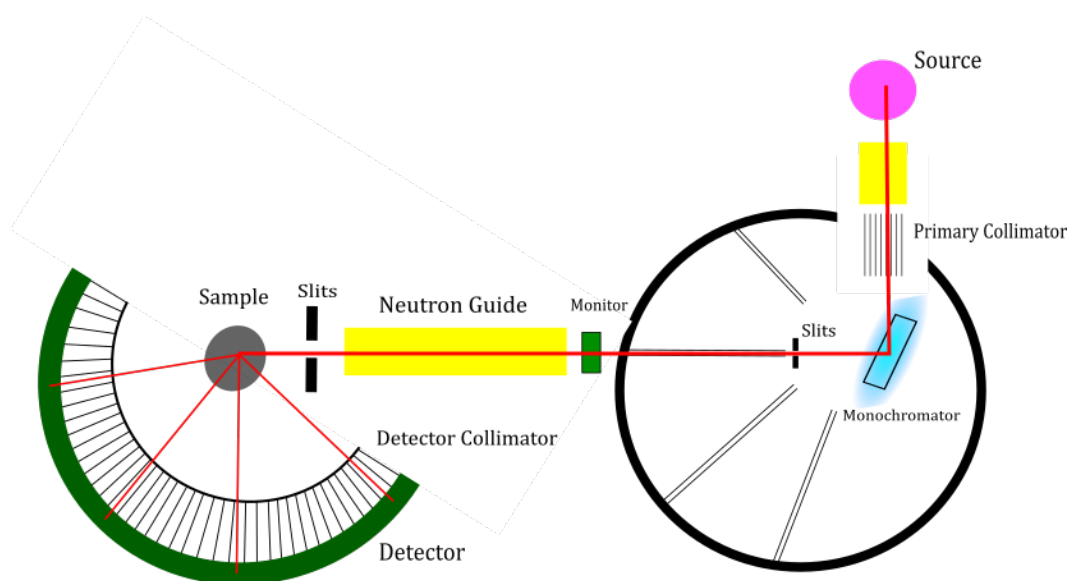
Figure 23 – Illustration of D20. The neutrons are generated at the source and are first passing the primary Collimator. The wavelength is selected by the monochromator. Then the neutrons are guided through two slit systems to the sample. The second monochromator in front of the detector is optional.

The neutrons are generated at the source in 17.5 m distance to the monochromator. Then they are passing the α_1 collimation focusing the beam with a horizontal angular divergence from $27'$ to $10'$. At the monochromator a wavelength between 0.82 Å and 2.41 Å can be selected with one the three monochromator types. For high beam intensities the take-off angles my be varied from $26°$ to $30°$ and from $42°$ to $46°$ for Cu. High resolution is obtain by using the Ge Monochromator at an take-off angle between $63°$ to $120°$. The beam is then defined vertically and horizontally by two slit system. The position sensitive detector covers a 2Θ range of $156.6°$ with 48 black-glass plates consisting of 32 cells filled with three bar ^3He and one bar CF_4. It provides an intrinsic resolution of about 3 mm at a detection efficiency of 60%. The resolution function is plotted in Figure 18. Optionally a radial oscillating collimator can be mounted in front of the detector [48].

The Instrument is highly flexible due to its multiple operation modes. The high neutron flux allows to measure sample with a low total scattering power but the lower resolution,

especially at scattering angles above $110°$, increases the uncertainty for the position of the peaks to a large extend.

5.4   High Energy Materials Science Synchroton Beamline HEMS
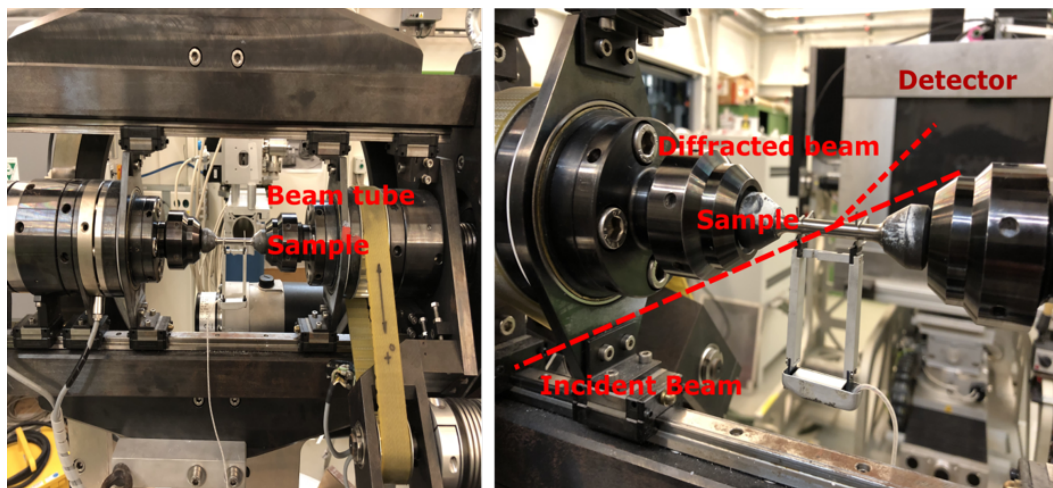
Figure 24 – Image of HEMS. The beam is scattered at the sample and scattered into the 2D Detector. The maximum available range of the scattering angle depends on sample detector distance and is chosen individually during each experiment. Covering larger detection angles leads to loss in resolution because the distance between the detector is lowered.

The High Energy Materials Science Beamline (HEMS) at DESY is build for high energy x-ray diffraction using energies between 30 keV and 200 keV. It can deliver a maximum flux of $7 \cdot 10^{11}$ ph/s at 100 keV at a source brilliance of 10^{18} ph/s / 0.1% bw/mA. The high flux combined with fast detector systems allows dynamic in-situ studies of processes like phase transitions or continuous loading experiments in samples. The beamline energy resolution varies between 5 eV and 250 eV at a beam energy of 80 keV [49].

The main beam optics of HEMS consists of two bent Si(111) Laue crystals with a $35.36°$ asymmetric cut, triangularly shaped with a base of 35 mm, a length of 89 mm and each 1.25 mm thick. The fixed exit with a horizontal deviation of 21 mm keeps the beam at a high of 1400 mm above the floor level. The energy is tuned with a double crystal monochromator in horizontal scattering geometry. The focusing optics allow spot sizes from 1x1 mm^2 down to 2x30 μm^2.

At the heavy load end station (EH3) the sample positioning is performed by a PI hexapod with a load capacity of 1 t and 1 μm resolution. The position ranges from $+202$--237 mm for x, ±204 mm for y and ±100mm for z. The maximum rotation angle of the table is $\pm180°$.

A total of 6 different 2D detectors are available for data acquisition. The most suitable detector for tensile experiments is the Perkin Elmer XRD 1621 Flat Panel with a field of view of 410x410 mm^2. The pixel size is 200x200 μm^2 giving a spatial resolution of 200 μm.
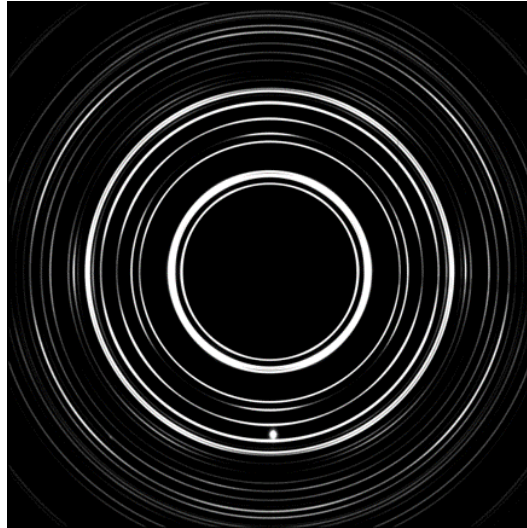
Figure 25 – The collected 2D-Data from HEMS. Full Debye Scherrer rings are collected during a measurement.

The angular resolution as well as the 2Θ-range depend on the used setup, e.g. the selected sample detector distance. On the detector portal it has 5 degrees of freedom for rotation and translation. The read-out time is 66 ms and the typical collection times are between 0.1 and 8 s.

Using synchroton radiation for the investigation of mechanical properties is typically resulting in very low scattering angles, which allow to cover full Debye Scherrer rings for the detector. The rings contain information of the strain development of every ψ orientation at the once for each loading step. Additionally, due to the high brilliance the measurement time for each pattern is approximately $1 - 2$s allowing measurements with continuous loading resulting in low measurement times. On the other hand the continuous loading introduces additional uncertainties for the applied stress and additional difficulties arise because depending on the measurement intervals a manual evaluation of collected experimental data is getting impossible due to a lack of time and the successful evaluation mainly depends on the quality and degree of automatisation.

5.5 Rotatable Tensile Rig

In typical neutron diffraction experiments only parts of the Debye-Scherrer rings are collected at the detector as shown in Figure 27. To measure the entire elasticity tensor the strains must be measured in as many directions as possible. To achieve this the load axis of the sample has to be oriented in the Euler space to cover as many orientation with respect to the measurement direction as possible.

As shown in Figure 26 the tensile rig designed at the Heinz Maier-Leibnitz Zentrum which has been used for the experiments is able to orient its load axis in all three angles of Euler
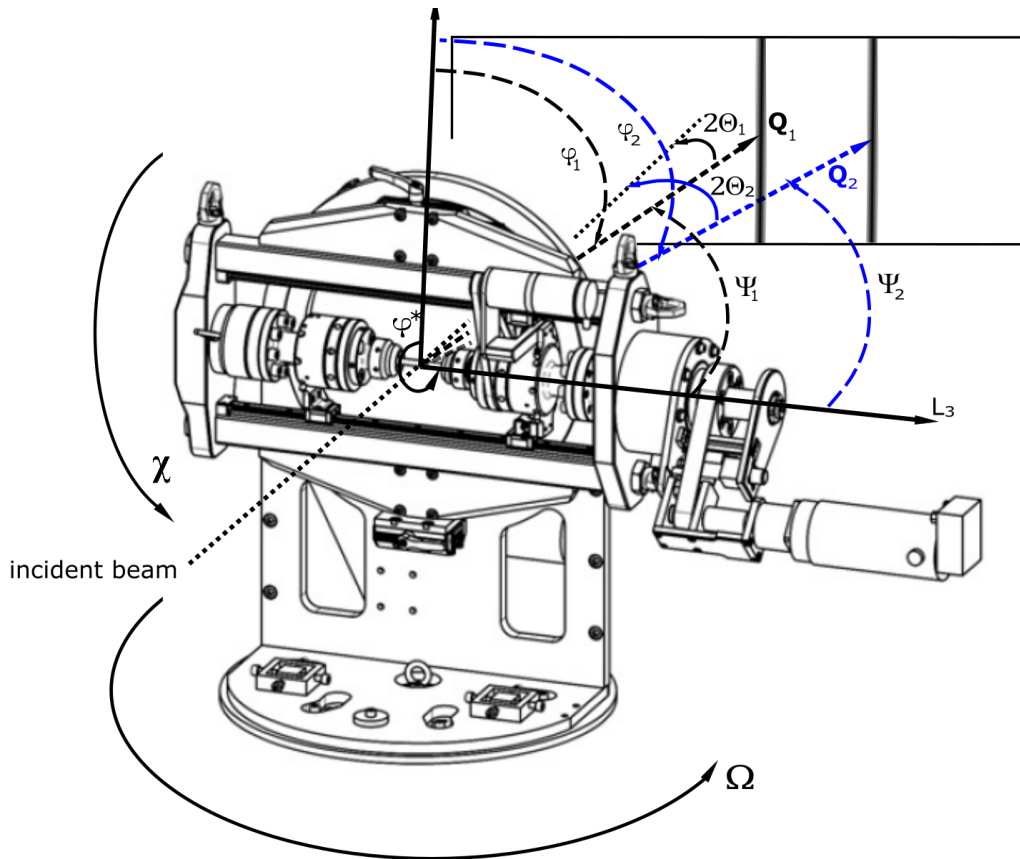
Figure 26 – The measurement geometry for neutron experiments. The χ- and φ-rotation rotations are the same standards as for an eulerian cradle. The Ω-rotation is achieved via the rotation of the sample table where the rig is mounted. The load axis is defined as L_3 and its angle to measurement vector defines the angle ψ. φ is defined by the angle between L_1 and the scattering vector. On the tensile rig, i. e. the sample frame, L_1 is defined as shown in the illustration for $\varphi^* = 0$ [42].

space χ, Ω and φ*. The Ω angle is covered by the turnable sample table on which the rig is mounted. The Ω angle ranges between $0°$ and $90°$, depending on the definition either of which is set parallel or perpendicular to the beam. χ can be varied between $90°$ and $180°$ where $90°$ is defined as the horizontal and $180°$ as vertical alignment of the load axis. For φ* any angle between $0°$ and $360°$ may be selected and $0°$ is defined by the sample while setting up the measurement [50].

The load axis is able to put compression or tensile forces up to 50 kN on the sample. There are two different designs available, the first is able to apply additional torque up to 100 Nm but is unable to rotate φ. The second design allows the φ* rotation but is unable to torque. The maximum travel distance between the crossbar is 50 mm and 75 mm for design 1 and 2, respectively [50].
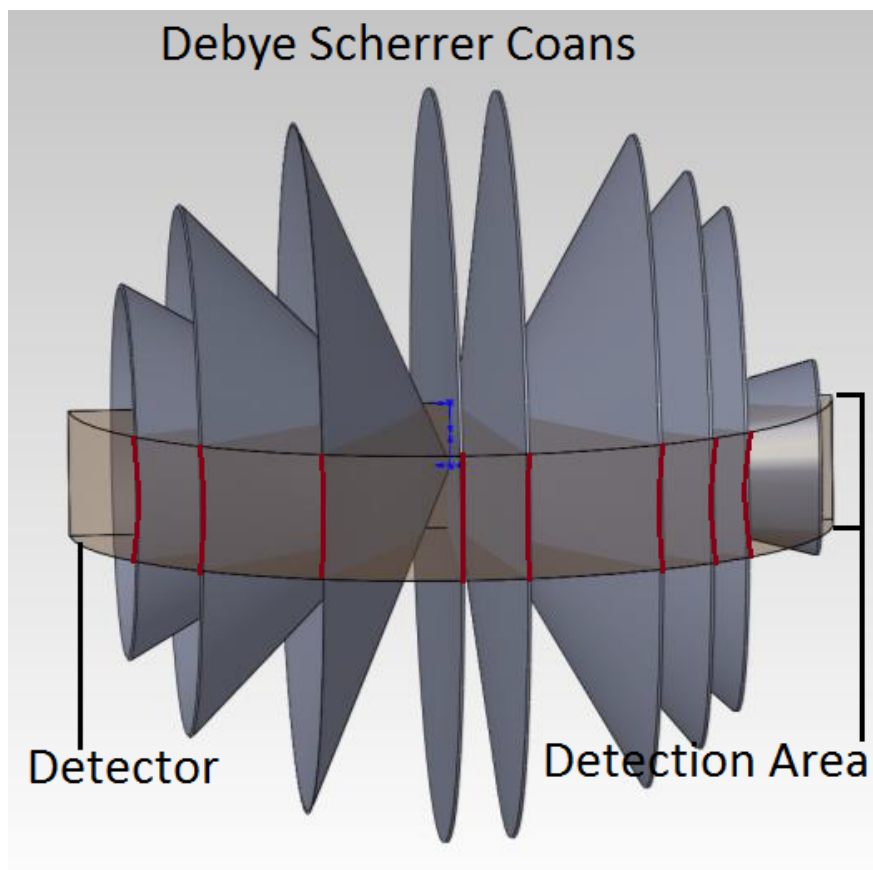
Figure 27 – Illustration of the Debye Scherrer rings and the detector collecting parts of them.

5.6   Materials and Samples

This section provides all important information on the samples. Three families of alloys have been measured in the scope of the work. To ensure the quality of the data treatment and the accuracy of the obtained results four different ferrous metals have been investigated. For the investigation of the mechanical behavior these types of materials are specially suited for developing new methods. Due to extensive prior research and wide availability of literature data. The further development of this method allows to measure single-crystal elastic constants on dual-phase alloys with distinct different elastic properties. This method was finally applied to a dual-phase titanium alloy containing a h.c.p. and b.c.c. phase. The results are compared to measurements performed on two single phase titanium alloys. The last sample investigated is heavily irradiated Zr4 which is compared to literature data derived from non-irradiated Zr4. A full list of every sample measured is provided in table 7.

The sample geometry used for the tensile tests DIN 50125 is given in the Appendix. The macroscopic Young's modulus of each ferrous sample was measured in three independent tensile test. For each test the stress was ramped up to 300 MPa in 0.1 MPa steps. Most of the neutron measurements where done with a diameter of 8mm and the synchrotron experiments were done with 6mm in diameter, Figure 28.

Table 7 – A full list of every sample investigated for this work.

Sample	Composition (wt%)	Experiment	Instrument	Phase
Ferritic Steel S235JR	Fe	T. D.*	SPODI, STRESS-SPEC	I m $\bar{3}$ m Single
Austenitic Steel X 5 Cr Ni 18–10	Fe 10Ni 18Cr max. 0.07C 1Si 2Mn 0.045P 0.015S 0.11N	T. D.	SPODI	F m $\bar{3}$ m Single
Duplex Steel X2CrNiMoN 22–5–3	Fe 22Cr 5Ni 3Mo 0.15N	T. D.	SPODI	I m $\bar{3}$ m, F m $\bar{3}$ m Dual
ADI	Fe 3K 3Si	T. D.	SPODI	I m $\bar{3}$ m, F m $\bar{3}$ m Dual
Ti 64	Ti 6Al 4V	M.**, T. D.	AMSL***, D20	HCP Single
Ti 6246	Ti 6Al 2 Sn 4 Zr 6Mo	M., T. D., EBSD	AMSL, HEMS, LMU	HCP, I m $\bar{3}$ m Dual
Ti 38644	Ti 3Al 8V 6Cr 4Zr 4Mo	M., T. D.	AMSL, D20, HEMS	I m $\bar{3}$ m Single

*Tensile Diffraction
**Microscopy
***Advanced Materials Science Lab

5.6.1   Ferrous samples

The validation of the measurement principle and the accuracy of the evaluation was shown on different ferritic (b.c.c.) and austenitic (f.c.c.) steel and cast iron samples. The diffraction studies of these samples were carried out on SPODI at a monochromator angle of $155°$ using Ge(511) for a wavelength of 1.5483 Å:

> **Ferritic structural steel S235JR** is very simple to fabricate and widely used in construction. For the elastic measurements on SPODI the Ω-angle was set to $45°$ and two loadings were applied, 0 kN and 5 kN, according to 0 MPa and 176.929 MPa at a sample diameter of 8 mm. Each load was measured for seven different χ-orientations: $0°$, $15°$, $30°$, $45°$, $60°$, $75°$ and $90°$. Second in situ measurements during plastic deformation have been performed on STRESS-SPEC. Three detector positions were used to cover the (110), (200) and (211) peak for four χ-orientations at $0○$, $30°$, $60°$ and $90°$. The maximum stress reached during the second experiment was 600 MPa. Four steps were measured in elastic region and 15 in the plastic region reaching a total sample strain of 2.8%.

> **Austenitic stainless steel of AISI type 304 (X5CrNi 18–10)** is the most commonly used stainless steel. The experiments were performed at a constant Ω-angle of $45°$ while totally 10 different χ-orientations were measured for each load step beginning at $0°$ increasing to $90°$ in $10°$ steps. 0 kN, 4 kN and 7 kN were applied to the sample with a diameter of 8 mm corresponding to an applied stress of 0 MPa, 141.543 MPa and 247.700 MPa.

Duplex steel (X2CrNiMoN 22–5–3**)** consists of two phases one austenitic and one ferritic phase and combine easy casting methods with a good corrosion resistance. All measurements were performed at a constant Ω-angle of $45°$. For each load step diffraction patterns for 5 different χ-orientations were collected at $0°$, $22.5°$, $45°$, $67.5°$ and $90°$. 4 load steps of 0 kN, 3.33 kN, 6.67 kN and 10 kN were applied to the sample with a 8 mm diameter resulting in an applied stress of 0 MPa, 117.776 MPa, 235.906 MPa and 353.682 MPa.

Austempered ductile iron (ADI) is a specially heat treated ductile iron. Due to its microstructure the mechanical properties are better than most other iron or steel compositions. For the measurements 4 load steps were applied from 0 kN to 15 kN in 5 kN steps. For each load step diffractions patterns were collected at $0°$, $22.5°$, $45°$, $67.5°$ and $90°$ χ-angle with a constant Ω-angle of $45°$.
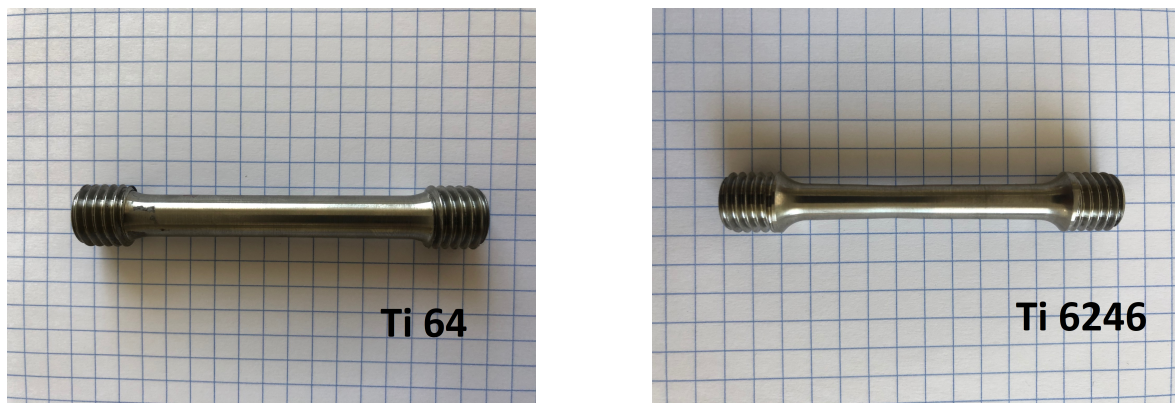
Figure 28 – Two tension samples of Titanium with diameters of 6mm are shown. Ti64 on the left and Ti6246 on the right. The shape was manufactured based on the DIN norm shown in the Appendix for a sample diameter of 6mm.

5.6.2   Titanium Samples

Further investigations where performed on three titanium samples with different phase compositions for the α (hexagonal) and β phase (b.c.c.).

Microstructure investigations   to determine the grain size and form were carried out with an optical microscope. The samples where cut along and perpendicular to rolling direction and embedded according to figure 29. Titanium is known for its extreme ductility which produces long chips when machine cut therefore silicon carbide cut-off wheels were used and to avoid heat damage water cooling was applied during cutting. After embedding the samples a two-step grinding is performed on the surface. For plane grinding a MD-Mezzo
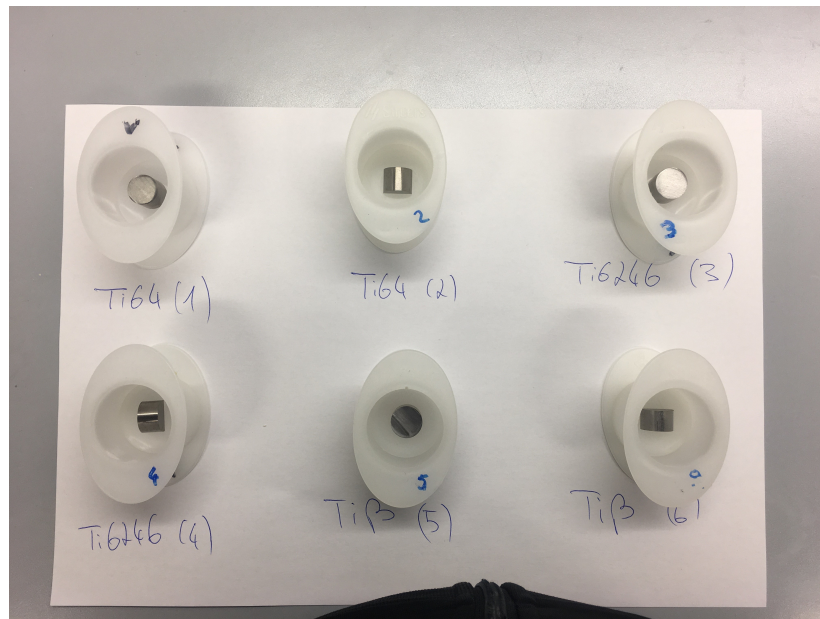
Figure 29 – The image shows the the cut samples before embedding. The next steps are grinding and polishing.

disk with a Diamond size #220 abrasive is used. The rotation speed is set to 300 rpm with an applied force to the surface of 25 N. The grinding is performed under water suspension until the surface is plane. Titanium is known for its extreme ductility. This causes the surface to smear out during the fine grinding and polishing of surface. During the fine grinding this cannot be completely avoided, see figure 30 β-Ti. Therefore only one step of fine grinding with a hard surface, MD-Plan with 9 μm diamond abrasive, is applied before polishing. The rotation speed is reduced to 150 rpm at 15 N applied Force on the specimen. The fine grinding is performed for 5-10 minutes with a DiaPro Largo 9 suspension. This will remove all major and most of minor scratches while the smear-out is reduced to a minimum. A chemical-mechanical polishing is used to remove the minor scratches and smearings from the fine grinding. The chemical is applied as suspension OP-S which is a mixture of colloidal silica and H_2O_2 hydrogen peroxide (30 %). The reaction of the chemical works slow enough that all reaction products of the titanium and H_2O_2 are removed and no corrosion effects remain. In this way small layers of the surface are removed while keeping it free of any mechanical deformation. As surface a MD-Chem with 0.04 μm size collodial silica abrasive was used. The rotation speed of the samples was set to 150 rpm with a force of 10-20 N on the samples. The polishing time varied from 5 to 15 minutes depending on the results of the fine grinding. Etching improves the contrast of the images greatly by coloring coloring the individual phases differently. The most common etchant to color the β phase brown is Kroll's reagent.

- 100 ml water
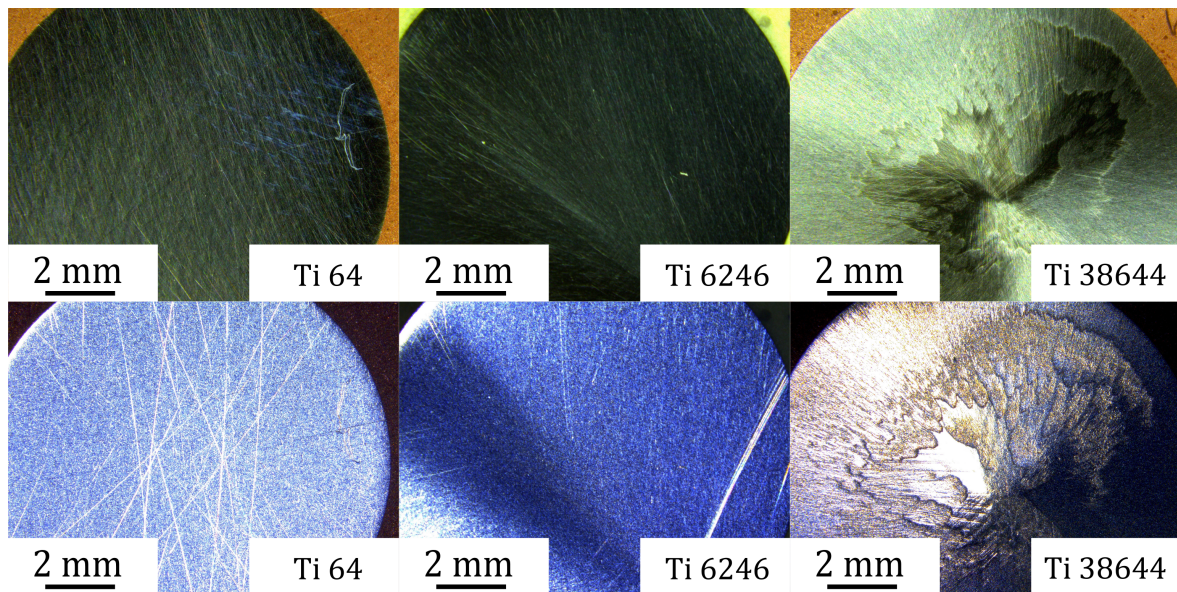
Figure 30 – Images of the samples after fine grinding at a scale of 2 mm. The upper row is made with white light while the lower row is taken under polarized light. The images show Ti64 on the left, in the middle Ti6246 and Ti38644 on the right. After the fine grinding the best result was achieved for Ti6246 and the worst for Ti38644 due to heavy smearing.
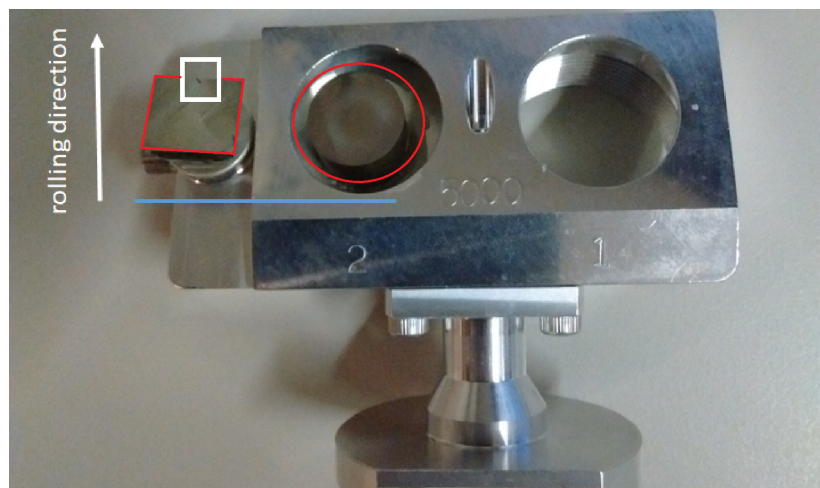
Figure 31 – An illustration of the cutting direction. The Ti6246 sample was cut along and perpendicular to the rolling direction.

- 1-3 ml hydrofluoric acid

- 2-6 ml nitric acid

During diffraction experiments the texture of the sample was measured on Stress-SPEC using the Ge(311) monochromator, setting the wavelength to 1.68 Å. Each reflection intensity was measured from $0°$ to $360°$ in $5°$ steps in φ and seven different orientations in χ.

Ti-6**Al**-4**V (Ti**64**, near-**α **alloy)** is a high strength titanium alloy and is considered as

the "workhorse" alloy for aerospace applications. This alloy offers a very good strength, toughness up to $400°$ C combined with good fabricability. The ODF was calculated from the reflections $\{002\}$, $\{100\}$, $\{101\}$, $\{103\}$ and $\{112\}$. The macroscopic Young's modulus was determined using 5 different sets of tensile testes, three elastic tests up to $1\,061$ MPa in 0.3 MPa/s steps and two tests were performed until rupture at a constant strain rate of 0.001% per second. Elastic diffraction measurements were performed on D20 at ILL in Grenoble with an constantly set ω angle to $43.5°$ on 8 mm diameter samples at a constant wavelength of 1.544 Å. The stress was varied in three steps 4 MPa, 199 MPa and 398 MPa. The χ angle was varied from $0°$ to $90°$ in $10°$ steps. No ϕ rotation was applied to the sample. A large amount of reflections was used for the evaluation of elastic data, totally 13 different crystallographic directions ranging from $\{100\}$ to $\{203\}$

Ti-3**Al**-8**V**-6**Cr**-4**Zr**-4**Mo (β-Ti, β-alloy)** has a high corrosion resistance due its cubic b.c.c. phase and very high strength but has a lower elastic modulus. Two Tensile tests up to 600 MPa at a stress rate of 0.01 MPa/s were used to determine the Young's modulus and two stress-strain curves until rupture were collected at a constant strain rate of 0.001 %/s The ODF was calculated from the reflections $\{100\}$, $\{110\}$ and $\{111\}$. This sample was measured on D20 with the same wavelength, ω angle and no ϕ rotation as Ti64. The sample diameter was 8 mm and the stress varied in four steps: 0 MPa, 199 MPa, 398 MPa and 597 MPa. The evaluation of the elastic properties was based on 5 different crystallographic directions

Ti-6**Al**-2**Sn**-4**Zr**-6**Mo (Ti**6246**, α- and β-alloy)** is a very high strength two phase titanium alloy but with lower toughness than Ti64 but it can be operated at higher temperatures. The phase composition, texture, elemental composition was measured by EBSD and EDX. Preparation for electron backscatter diffraction (EBSD) and energy-dispersive X-ray diffraction (EDX) was performed by mechanical cutting and polishing. The EBSD images of the Ti6246 sample where taken on two different surfaces one along and one perpendicular the rolling direction as shown in figure 31. After cutting, plane grinding was performed with an MD-Mezzo surface followed by a single fine grinding with a 9 mm diamond suspension abrasive on an MD-Largo surface. The first polishing was performed with an MD-Chem surface and a 0.04 mm collodial silica abrasive and a final step of ion polishing with a Hitachi IM4000PLUS cross section ion polisher operated at 5 kV and 200 mA for 60 min with sample oscillation. EBSD maps were measured on a Hitachi SU5000 field-emission scanning electron microscope equipped with an Oxford Instruments NordlysII EBSD detector and an ULTIM MAX EDX detector. The employed acceleration voltage was 20 kV. EBDS and EDX signals were collected simultaneously with the sample inclined by 70 towards

the EBSD detector. Data evaluation was performed with the Oxford Instruments AZTec and CHANNEL5 software. The elastic measurements have been performed on P07 HEMS at DESY using a Perkin Elmer detector setup and samples of 6 mm in diameter. The photon energy was set to 98.25 keV resulting in a wavelength of 0.12619 Å. The detector distance was set to 138 cm. At that range 16 peaks are collected for the α phase and 5 for the β phase. ω is set to a position where the load axis is perpendicular to the photon beam. No φ or χ rotation is used during the experiment because at these scattering angles full Debye-Scherrer rings are collected. For the evaluation the rings are sliced into pieces of $10°$ from $0°$ to $180°$ and assigned to their corresponding χ value. The stress was driven continuously to 882 MPa at a speed of $5 \frac{\text{N}}{\text{s}}$. The rings were collected over 2s corresponding to an error of 0.35 MPa. For acquiring of the DEC and the single crystal elastic constant over 500 load steps were evaluated leading to a total of $9\,000$ diffraction patterns. After reaching the desired stress in the elastic regime the experimental mode was changed to strain mode. During this mode of operations the tensile rig adjusts the applied sample stress to reach a constant strain rate. The plastic regime was investigated up to a total sample strain of about 18% at a constant strain rate of $0.02 \frac{\%}{\text{s}}$. The instrument and detector settings remained the same as for the elastic regime. The collection time of the detector remained at 2s resulting in a systematic error of 0.04% for the sample strain values.

6   Data Treatment

The elasto-plastic analysis of the diffraction data is performed using a self-designed software. The basic concept of this software is to store all relevant data for the analysis of the material centrally and to derive the elasto-plastic properties with as few analysis steps as possible. Furthermore, after all basic mechanical parameters are set the program is able to predict the stress strain behavior of the material and contains a set of tools for the analysis of the anisotropy, load transfer, texture and activated slip system along different crystal orientations. The elasto-plastic simulation includes the stress-strain behavior of differently oriented grains

Figure 32 – Flow chart of the program developed for the strain-data treatment. Black lines indicate the storage, for example "Diffraction pattern" is stored at "Sample Data". Blue lines indicate that the inclusion of this data in the evaluation is optional. Red lines show the requirements to derive specific parameters. For example to derive the single crystal elastic constants the strain data is required. Green lines indicate an alternative way for calculation, for example the single-crystal elastic constants may be calculated by the strains directly, they can also be determined using the DEC.

in the sample and their plastic shear rate caused by the activation of different slip-systems. Furthermore, it includes the average stress-strain behavior of the material.

Figure 32 shows a flow chart illustration of the software. The core of the program consists of the class **Sample Data** which stores all relevant information of the sample.

- The phase composition of the sample is stored in a separate class called **CODData**.

It stores all cell parameters, the composition of the phase and its symmetry group. Additional parameters regarding the phase fraction and microstructure are stored for the multiphase analysis. For each phase it can be selected whether it is the matrix or the inclusion. The geometry of the inclusion can be set to either spherical or ellipse type.

- Multiple tensile tests of different sample geometries are attached to the sample class. They contain the applied force, the measured extension, the cross-sectional area of the sample, the applied stress and the resulting strain. For diffraction experiments carried out during the tensile test it is possible to synchronize automatically the diffraction data with the tensile data.

- The ODF (Orientation Distribution Function of grains) is attached to **Sample Data** and is loaded via a file which contains in the first three columns the Euler angles and in the fourth the m.r.d. values. The texture can be added optionally during any stage of the analysis.

- The yield surface including its slip systems is pre-added to each phase during its invocation. The yield strength and hardening parameters of each individual slip system can be edited by hand. Optionally, the system may be turned off during the simulation. The values of the yield strength are either derived directly from the measured diffraction data or imported from literature.

6.1   Strain data

The basic data class stores all important data needed to derive all elastic properties. It consists of a measured strain, which is associated to a Bragg peak (hkl), the orientation ϕ and ψ with respect to the measurement vector $\mathbf{Q}$ and the applied macroscopic stress in L_3-direction. The data can either be added directly via an ASCII file, with the formatting given in the Appendix or it can be retrieved straight forward by fitting 1D-diffraction patterns. An example of this feature is given in Figure 33. The peaks are automatically scanned while adding the pattern data to the sample. Two options can be selected for the peak search. The first estimates the position of the peaks based on the given wavelength and the second one applies a peak finding algorithm and determines the position of the peaks independent of the given crystal structure. The applied stress and the sample orientation is entered for each diffraction pattern individually. The Bragg peaks can be described by three different peak functions, Gaussian, Lorentzian and Pseudo-Voigt[2] where the last is set as standard with 90% Gaussian fraction fraction, close to the average fraction obtained on SPODI . The position, FWHM and the exact Gaussian fraction is obtained from the pattern data

---

[2]Pseudo-Voigt is a linear combination of Gaussian and Lorentzian.
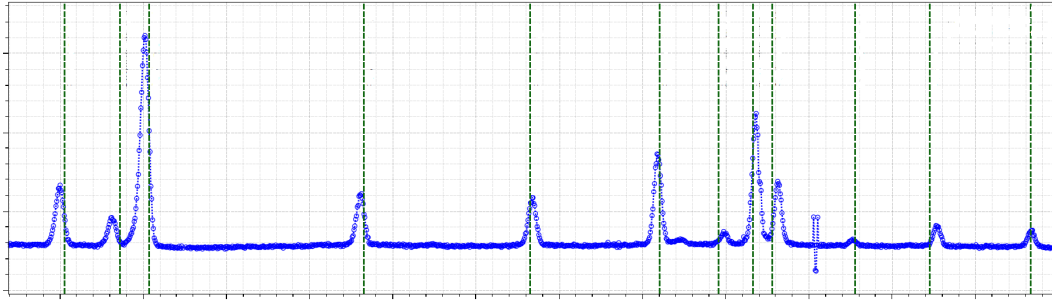
Figure 33 – A diffraction pattern of Ti64 collected on D20. The vertical lines indicate the position of the peaks estimated by the lattice parameters and used wavelength.

by a Levenberg-Marquard fitting algorithm. For this purpose the width of the peaks in the patterns is estimated by the instrument resolution function of the given instrument. All overlapping peaks are grouped together and their parameter are optimized simultaneously to minimize χ^2, see figure 34.

To obtain all strain values are calculated relative to the reference position of the lowest applied stress, i. e. $\epsilon = \frac{d-d_0}{d_0}$. This way the non-linearities sometimes observed in equation (25) are minimized since existing phase stresses are taken into account which do not change during elastic deformation.

6.2 Single-Crystal Elastic Constants and Load Transfer in Dual Phase Alloys

The program allows to use two different routes to derive the single-crystal elastic constants. As indicated in figure 32 the single-crystal elastic constants may be derived from the strain data directly or via minimizing the differences in the DECs. The DECs are derived by sorting the data according to match equation (19) which is implemented in its rewritten form shown in equation (84). The y-values of the data points are given by the measured strain divided by the applied stress and the x-values are calculated from the orientation ψ. An example of the data and the fit is given in Figure 35 [42].

$$\frac{\overline{\epsilon_{33}}}{\sigma_{33}} = s_1 + \frac{1}{2}s_2 \cos^2(\psi) \tag{84}$$

To avoid additional non-linearities caused by plasticity induced micro stresses in equation (84) only values of the elastic deformation should be evaluated for the fit. The texture of the sample is taken into account by weighting the strain values according to the m.r.d. value of the corresponding orientation. The different models for the grain-to-grain interaction are implemented through equations (29), (30), (31), (31) (34), (36) and (49). The fitting is performed by a Levenberg-Marquard χ-minimization algorithm. As in case of the DEC the texture is taken into account by weighting either the DEC or the strain values according to

Figure 34 – Screenshot of the peak fitting window during the evaluation. On the left in the red box there is a list of peaks contained in regions. The selected region is shown in the plot while the blue line indicates the fitted curve. In addition each peak can be adjusted manually in the green box. Each fit is performed in an own thread, therefore a large number of region can be fitted simultaneously. By adding a diffraction pattern to the sample data each pattern is searched for peaks, these are combined into regions and automatically fit for their positions. A special algorithm improves the starting values each time a peak is fitted.
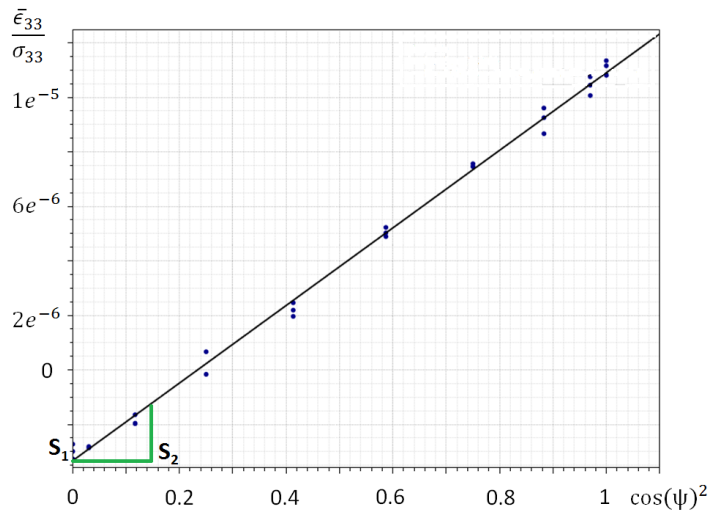
Figure 35 – This screenshot taken during the evaluation shows an example fit of the DEC of the (220) Bragg reflection in the β-phase of titanium.

the m.r.d. values of the covered orientations.

The self consistent calculation of the single-crystal elastic constants including the load transfer is shown in Figure (37). First the stress-strain data for the phases are set, from the
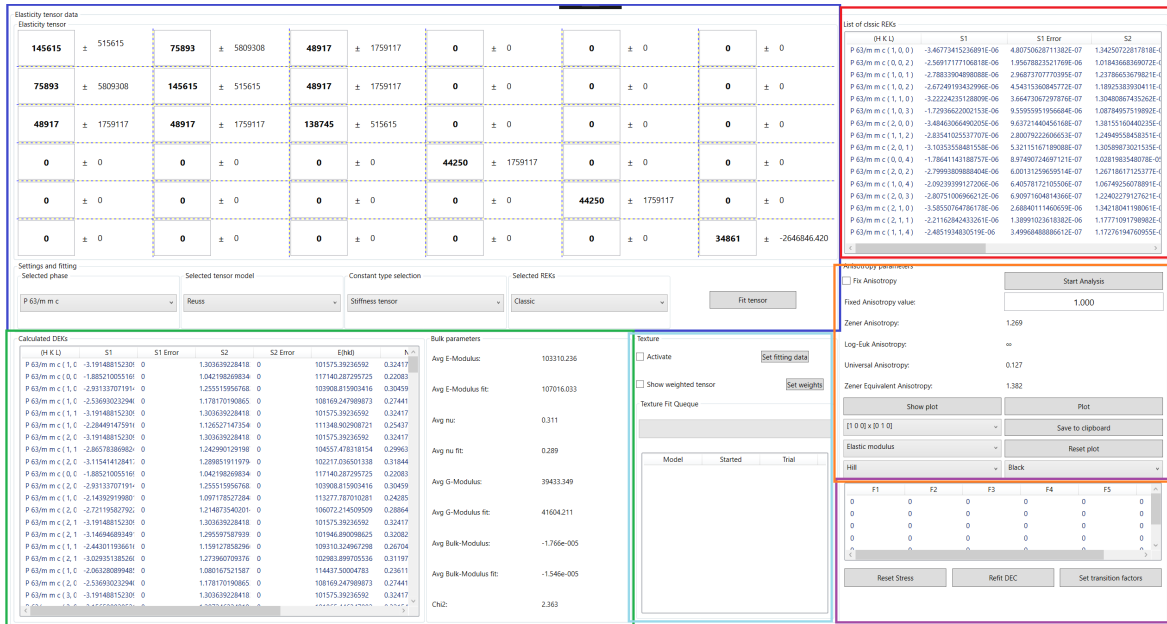
Figure 36 – Screenshot of the evaluation of the single-crystal elastic constants. On the top left in the blue box the fit constants and on the right the DECs are shown. Below the settings for the analysis such as the displayed phase, the grain-to-grain interaction model or whether stiffnesses or compliances should be displayed are selected. Below in the green box the DECs predicted by the selected model are shown. On the right average values of Young's, shear and Bulk modulus are given according to the used grain-to-grain interaction model where fit indicated the values obtained by the measurement. In the red box each experimentally obtained DEC is listed. In the orange box the analysis of the anisotropy is performed where in the case of cubic crystal symmetries multiple fits of the elastic constants for different fixed values of A are performed and saved as ASCII or .xlsx. The plot settings for parameters such as the Young's and shear modulus along different crystal direction are found here, too. In the right corner inside the purple box the transition factors for the phases are displayed if a load transfer analysis is applied.

data the elastic constants are derived either directly or via the DEC. The load transfer of the phases is calculated by equation (54) and the stress-strain data is adjusted according to the transition factors. The calculation is repeated until a satisfying convergence of the transition factors is reached and the stress in the phases does not change anymore.

6.3 Elasto-Plastic Self Consistent Modeling (EPSC)

The software also allows to predict plastic stress-strain behavior and here all elastic properties described in the previous section are needed for the evaluation. The program is designed to synchronize straining data obtained by diffraction experiments, tensile test and EPSC modeling. This design allows the comparison of each aspect of EPSC modeling to experimental parameters on the corresponding length scale: Diffraction experiments yield the lattice strains at a given macroscopic stress which corresponds to the average elastic strain of all crystallographic directions perpendicular to the scattering planes. This in turn reveals

Calculate the transition values f_i
and reset the stress-strain data
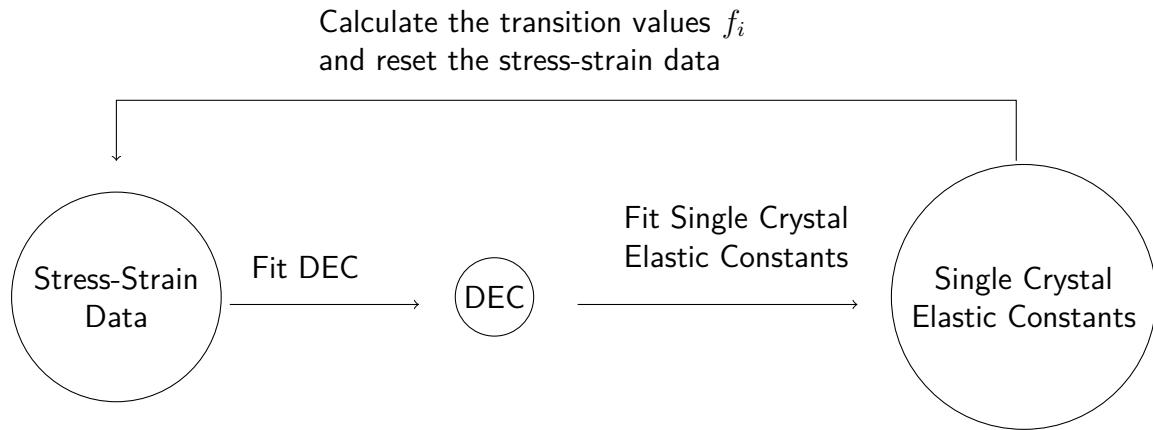
Figure 37 – The scheme for the self-consistent calculation single-crystal elastic constants accounting for the load transfer.

the stress state of the diffracting grains and therefore allows to compare the diffraction data to the forecast stress-strain values of oriented grains through the EPSC simulation. On the other hand tensile tests show the macroscopic stress-strain behavior. This covers the elastic and plastic strain caused by all grains of every orientation caused by an uni-axial tensile or compression force. The measured values are then compared to average stress-strain results of the simulation.

There are only few input parameters required for EPSC modeling. The elastic behavior is completely described by the single-crystal elastic constants. The plastic behavior is characterized by the activation of different slip systems in the corresponding grains. This requires the input of the slip-systems which are defined by the given crystal structure. The forecast of the slip activation during loading depends on the yield strength and hardening of every slip system. Different methods exist to calculate the shear stresses acting on a crystallographic plane. The software supports three basic slip criterion: von Mises, Tresca and a standard projection of the stress tensor on the plane along the slip direction. The software is able to track the hardening for each grain orientation individually or uses calculated average values for every grain among all orientations. The orientations used during the EPSC simulation are stored individually in a list. This allows to use any texture input desired which can be modified to match possible texture changes during plastification. To compare the simulation results to different types of experiments, the software handles diffraction and tensile data and offers a wide range of plotting options as described in Figure 38.

The main recipe of the EPSC scheme implemented is shown in Figure 39 and was given by Hutchinson in 1970 [22]. The program supports four data input types, the stress and strain tensors or their rates, respectively. The simulation input is split up into individual calculation steps for each stress or strain state reached during the simulation. For each of which a self-consistent loop is calculated until the tensor $\overline{L}$ converges as indicated by red in Figure 39. Based on the previous deformation history a new set of potentially active
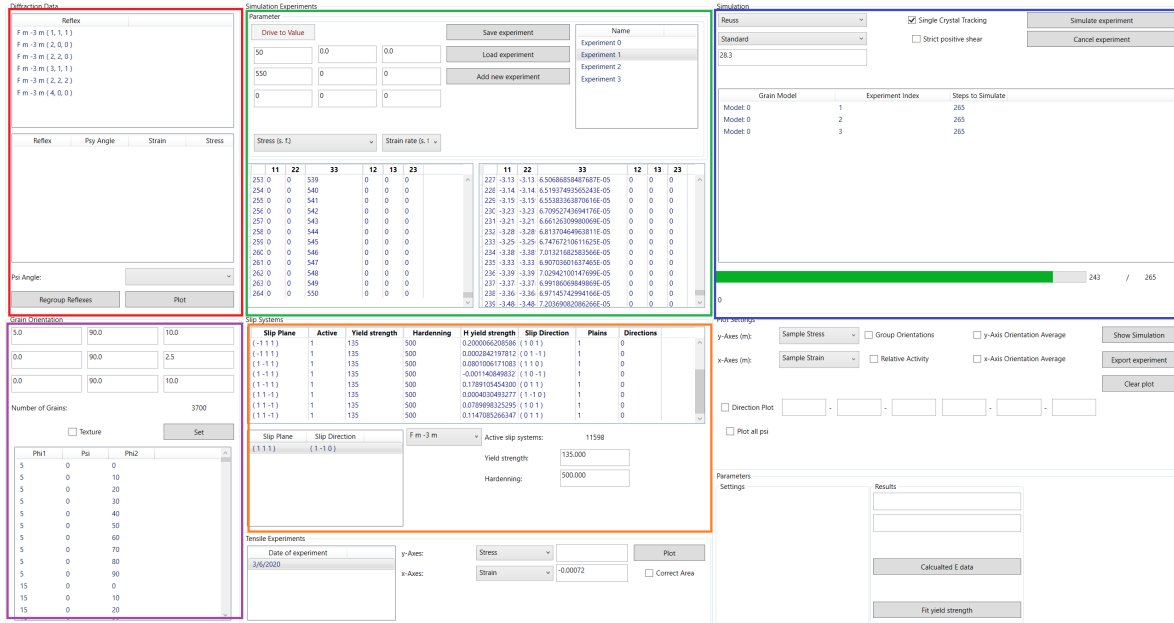
Figure 38 – The image shows a screenshot of the settings and options of the EPSC Modeling. "Diffraction Data" in the red box contains the strain data obtained by the input diffraction patterns. The upper "ListView" contains a list of peaks measured for different lattice planes and ψ-orientations and allows according plots. "Simulation Experiments" in the green box contains a management of different input values for the EPSC simulations. Below the input matrix two "ComboBox" allow are detailed view of the input and output parameters of the modeling. The EPSC simulations are organized by a queuing system in "Simulation" in the blue box. Every task contains the single-crystal elastic constants, shear conditions and other different options. The tasks are executed from top to bottom and the progress is shown together with some statistics of the modeling. The lower half of the window contains the grain orientation management found in "Grain Orientation" marked by the purple box. All grain orientations can be modified or added here. This allows the input of any type of texture for the EPSC simulation. The slip families of the grains are managed in "Slip Systems" in the orange box it contains the yield strength and hardening of every slip system of each phase used during the modeling.

slip systems is created for each predefined input state. The list of potential slip systems are chosen from all available slip systems of this crystal symmetry according to which slip system satisfies equation (68). From this set the active systems meeting the requirement (69) are determined in the loop indicated by the orange line. In this loop all important parameters to describe the plastic deformation are calculated as shown in section 4.9. For each orientation $\mathbf{L}$ in equation (73) is calculated using equation (76). At this stage of the calculation all parameters necessary to derive $\mathbf{A}$ and $\mathbf{B}$ in equation (80) for the grain are given. Finally, the yield change of the available slip systems is updated according to the yield change given by equation (71).

After every parameter for each grain is determined, equations (81) or (82) are solved depending on how many phases are present. The obtained average values are compared to the values of the last cycle until the change is small enough to meet a user defined convergence
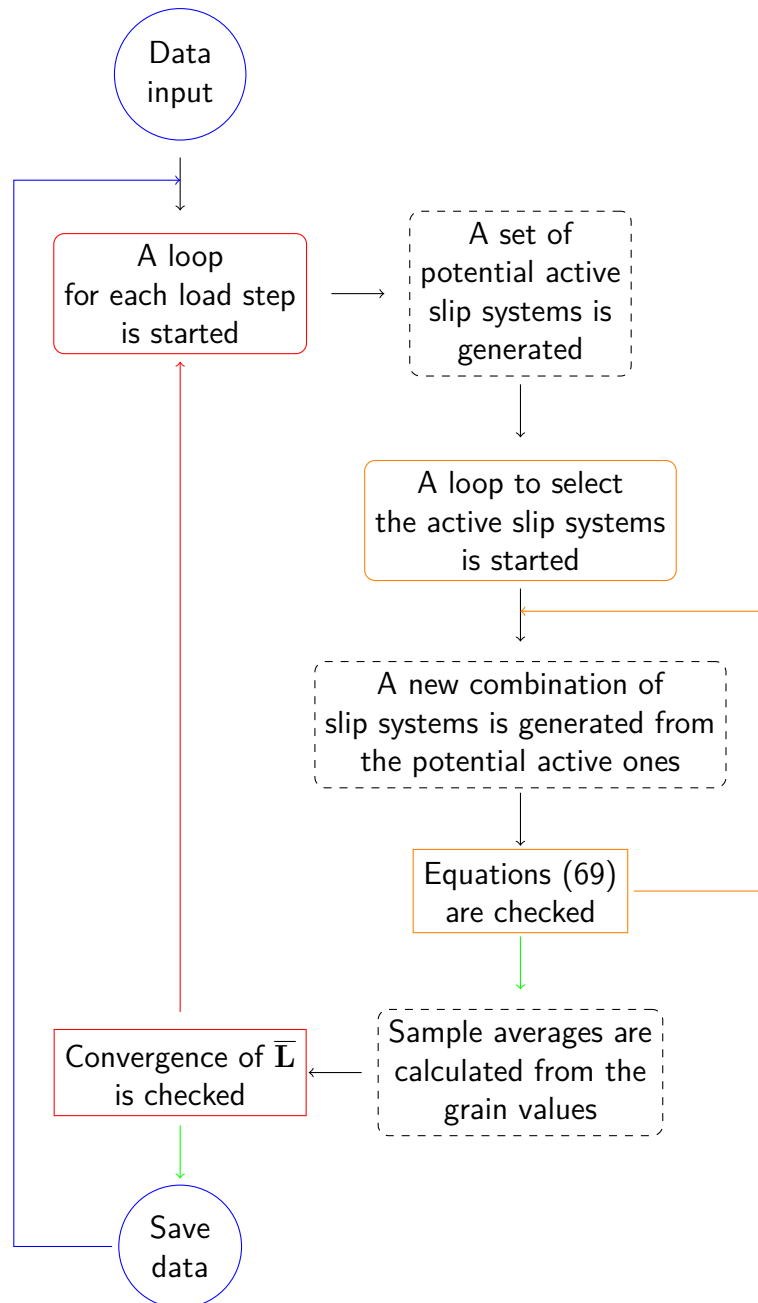
Figure 39 – The EPSC modeling scheme needs a list of second order stress or strain tensors as input parameters. They represent according stress or strain states of the sample. The scheme consists of two loops. The first iterates as long as $\overline{\overline{L}}$ converges self-consistently and does not change from iteration to iteration. The second inner loop ensures that only the correct combination of slip systems is active.

criterion. The stress-strain data of the simulation is finally stored to the "Elasto-Plastic Experiment" class and a new circle for the next input step is initiated as indicated by the blue line.

6.4 Estimation of Uncertainties

The previous sections described the necessary evaluation steps from measuring the lattice distances under load, calculating the strain values and assigning the experimental parameters to fit the DEC and finally the single-crystal elastic constants. How the data is supplemented with critical resolved shear stresses and potential slip families and ultimately used to predict the plastic stress-strain behavior under load.

The main source of uncertainty arises from the measurement of the exact scattering angle to determine the lattice distance or lattice strains for each experimental step.

$$\Delta\epsilon = \sqrt{\left(\frac{\Delta d}{d_0}\right)^2 + \left(\frac{d}{d_0^2} \cdot \Delta d_0\right)^2} \tag{85}$$

Considering each individual peak shift in the elastic region not to be larger than $5 \cdot 10^{-3}$, by assuming $\frac{d}{d_0} \approx 1$ equation (85) reduces to:

$$\Delta\epsilon = \sqrt{2} \cdot \left(\frac{\Delta d}{d_0}\right) \tag{86}$$

The error of the strain is therefore directly proportional to the diffraction instrument resolution. Each additional measured load step beyond the instrument resolution only contributes to the statistical confidence of the overall solution.

Error sources during the measurement such as the angles provided to orient the load axis and measurement vector $\mathbf{Q}$ are considered to be negligible because the accuracy of the positioning during the experiment causes overall deviations to the parameters orders of magnitude smaller than the typical errors of the measured strains.

The only input parameter during the experiment of significant importance is the applied load to the sample. Depending on the experiment mode, neutron diffraction with long measurement times and stepwise ramping up the applied load and synchroton diffraction with rapid measurement times and continuous loading, different types of errors are encountered. During neutron diffraction experiments the gravitational forces changes the applied force by about 0.5% depending on the orientation of the load axis. Additionally, after reaching the plastic regime the long measurement times cause an additional load drop to keep the strain constant for each measurement step. In the case of continuous measurements the deviation of the stress $\Delta\sigma = t_D \cdot \sigma_A$ depends on the collection time of the detector t_D and the applied stress rate σ_A. This error decreases with higher applied loads as $\Delta\sigma$ remains constant for all applied loads.

The errors of the DEC are calculated by the covariance matrix obtained during the fit. By calculating the strains from the first load step the gravitational offset is fully taken into account and non-linearities in the $\cos^2$-functions are reduced reaching an average error

of about 6-8% for the fitted DEC in this work depending on the instrument resolution. During the continuous measurement the error increases by about 1% on average due to the additional uncertainties during loading caused by collection time of the detector.

In a similar way the errors of the single-crystal elastic constants are derived from covariance matrix of the strain or DEC fit. The quality of underlying data defines the accuracy of the fit and therefore the same principles as for the DEC are applying to the single-crystal elastic constants as well. The margin of error for the single-crystal elastic constants varied in this work between 8% and 12%. The observed errors for c_{44} were found to be higher by 1-2% on average than those of the other two constants in cubic crystal lattices due to the accessibility during the experiments as later discussed.

Another more important error arises from the applied models and averaging methods. In general all different models for calculating the single-crystal elastic constants show consistent values and in most cases do not vary above the found uncertainties. As discussed in more detail in the following section the best indicators for the optimal model are the present microstrucure and predicted anisotropy. The same applies for the EPSC modeling. In this case the obtained errors are mainly caused by the applied calculation model therefore the errors are estimated by comparison to experimental data and directly visible in the plots.

7 Results

In the first part of this section the technique and its accuracy is tested on well-known ferrous metals. These metals offer the opportunity to investigate two different cubic phases, namely the ferritic and austenitic phase. Their wide spread use in modern industry leads to high standards and sophisticated manufacturing techniques which ensures a comparable high quality even in complex dual-phase alloys. Here also it turned out that the data storage and methods described in section 6 showed a high flexibility for automation. This reduces the potential for mistakes and grants fast evaluation times even for large data sets.

The second part shows how single-crystal elastic constants and their associated mechanical properties are derived from a dual-phase titanium alloy. The different elastic properties of the containing phases - in particular the significant lower stiffness of the β-phase - goes along with a large relocation of stress from the softer β to the harder α phase. The amount distributed is quantified and used during the evaluation to gain knowledge of all eight elastic constants from both present phases in a single diffraction experiment. To ensure the quality the obtained results are compared to corresponding values measured on single-phase alloys.

All grain-to-grain interaction models contain certain assumptions which enables to derive an analytical solution during the averaging over the different grain orientations. It has to be ensured during the measurement that the average strain observed is of statistical significance which Matthies concluded is reached by measuring a couple thousand different grain orientations [28]. In diffraction studies the elastic strains are measured over an average of different single-crystal domains. The number of grains measured depends on the size of the grains and the illuminated sample volume. Typically neutron experiments are illuminating large volumes of the sample in order of cm^3 and therefore for most materials the statistical significance of approximately 1000 grains contributing to the peak is exceeded by several orders of magnitude. In the case of photon experiments the beam size is in the order of only 1 mm which can reduce the statistical nature of the strain measurements to near single-crystal behavior. This is reached if the grains a larger than 50-100 μm depending on the texture, sample shape and maximum beam size. The orientation distribution function of the grains influences the measured intensities of Bragg peaks but not their positions. The number of measured grains during the diffraction experiment is considered to be constant for the different measurement directions because the grains are not reorienting during elastic deformation [42].

The elastic constants of all measured samples were evaluated using all available grain-to-grain interaction models, expect the interaction model proposed by Voigt [9]. This model showed multiple results or did not converge without constraints. Therefor the results are only shown once for the structural steel S235JR. The grain-to-grain interaction model introduced by

Reuss [11] has been found to be the most stable with the shortest time to convergence of less then 10 fitting cycles. Equation (45) in the proposed interaction model by Kroener [16] leads to invalid results which had to be sorted out during the fitting, thus increasing the average conversion time. The additional direction dependence modification introduced by de Wit doubles the average number of needed cycles compared to the interaction model of Kroener and in rare cases converged into multiple results. The load transfer approach described in section 4.7 could be applied to all models without affecting their performance or accuracy. The self-consistent routine shown in Figure 37 typically converged after 4 to 7 cycles independent of the interaction model used.

7.1   Ferrous Metals

This section provides values on the DECs and the single-crystal elastic constants of four different ferrous metals: Ferritic steel, austenitic steel and two dual-phase alloys. The obtained results show an excellent agreement with existing literature and the differences in the different grain-to-grain interaction models are discussed in detail. The influence of anisotropy on the mechanical properties are shown and its importance to the evaluation as a measure which interaction model to use is highlighted. These investigations were performed to check the applied methodology and to validate software performance and accuracy.
In the second part of this section the EPSC modeling is used to describe the plastic behavior of S235JR. The results of the modeling described in section 4.9 and 4.10 implemented as shown in section 6.3 are presented and discussed for their abilities and accuracy.

7.1.1   Diffraction Studies and Elastic Modeling

The neutron diffraction patterns used for the analysis of the elastic properties of all ferrous metals were obtained on the instrument SPODI. A close-up of the austenitic $\{111\}$ and the ferritic $\{110\}$ peaks of duplex steel is given in figure 40 as an example. The instrumental resolution was sufficient to resolve the peak shift caused by the applied stress.
Usually a good indicator for the quality of the experimental data is given by the evaluation of the DEC. Possible non-linearity of the data and the deviations of $\frac{\bar{\epsilon}_{33}}{\sigma_{33}}$ at specific orientations $\cos(\psi)^2$ increase the uncertainty of derived single-crystal elastic constants. Besides experimental issues non-linearity might be caused by strong texture and/or strain gradients. However, we are using the first strain state as a reference during the evaluation, thus texture effects as well as strain gradients obviously are canceling out in the elastic regime as seen in figure 41. On the other hand in dual-phase alloys with different stiffness between the phases additional phase stresses caused by load relocation can induce significant non-linearities in the $\cos(\psi)^2$ curve. An example of this specific behavior will be discussed in detail in the titanium section.
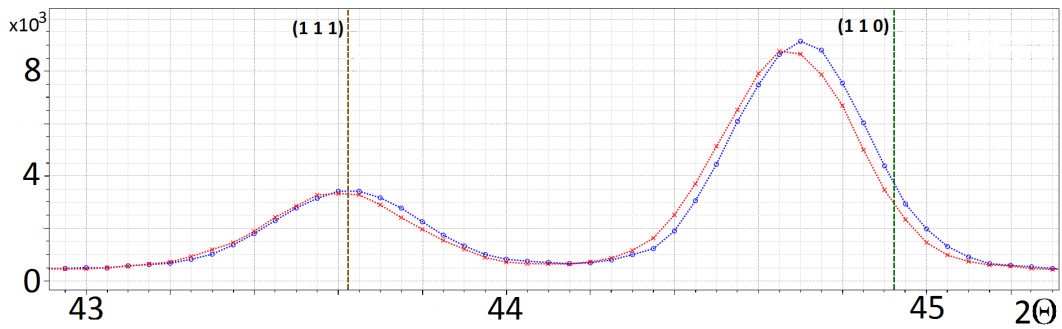
Figure 40 – A close-up of the austenitic $\{111\}$ and the ferritic $\{110\}$ reflection of X2CrNiMoN at zero load in blue and 3.33 kN load in red corresponding to an applied stress of 118 MPa. The shift in the peaks between the loading steps is clearly large enough to be detected even visually.

The DEC for the ferrous metals are given in table 8, a total of 6 and 5 peaks could be evaluated for the austenitic and ferritic phase, respectively. An example fit of the $\{220\}$ and the $\{111\}$ reflection of duplex steel is given in figure 41.
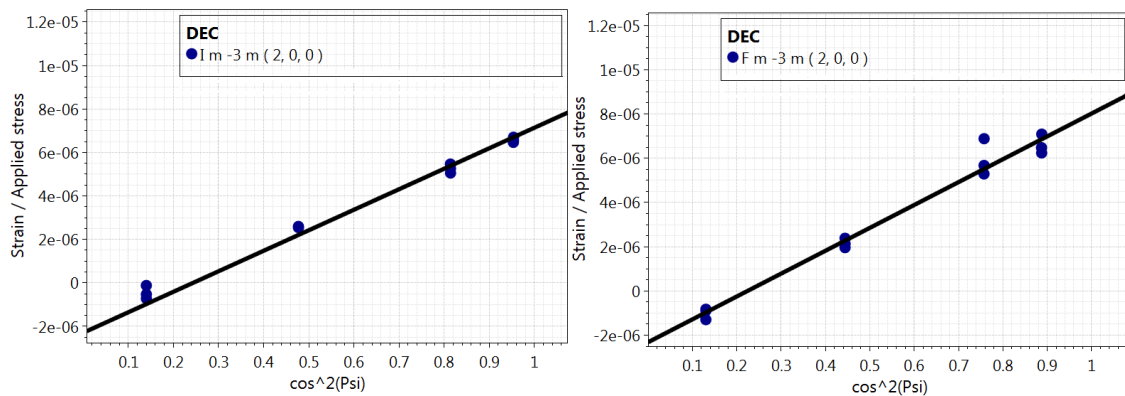
Figure 41 – The images show an example fit of the DEC of the ferritic $\{200\}$ reflection on the left and of the austenitic $\{200\}$ reflection on the right of duplex steel

The single-crystal elastic constants of the ferritic phase obtained from the measurements in S235JR are shown in Table 9 for all implemented grain-to-grain interaction models. Most interaction models agree reasonably to each other, with the exception of Voigt and De Wit models. As discussed earlier Voigt converges into multiple results therefore finding the global minimum during the fit is impossible. This is probably the reason no literature references to this modeling are found. The orientation dependence in shear modulus of the de Wit approach, shown in equation (49), causes restrictions to the stress-strain states. Certain parameters lead to only negative solutions for the shear modulus in equation (45) or multiple valid solutions. However, in both cases the algorithm converges into the last valid result after reaching these undefined states. Using Hill's approach the elastic constants derived in this work $c_{11} = 230.0$ GPa, $c_{12} = 121.0$ GPa and $c_{44} = 120.8$ GPa show very good agreement to values obtained by Finkel [32], $c_{11} = 232.0$ GPa, $c_{12} = 125.8$ GPa and

Table 8 – The DEC for different orientations measured in the austenitic and ferritic phase of various ferrous metals.

	s_1*	$\frac{1}{2}s_2*$	s_1*	$\frac{1}{2}s_2*$	s_1*	$\frac{1}{2}s_2*$
I m $\overline{3}$ m	S235JR		Duplex Steel		ADI	
(1, 1, 0)	−1.0373	4.9776	−1.8302	7.6875	−1.2303	6.2330
(2, 0, 0)	−1.6360	6.7086	−2.3079	9.4342	−1.9831	8.7780
(2, 1, 1)	−1.2021	5.6412	−1.6572	7.4323	−1.0482	6.0217
(2, 2, 0)	−1.1672	5.5656	−1.8992	7.7236	−1.3980	7.1732
(3, 1, 0)	−1.6403	7.2495	–	–	−1.8139	7.1732
F m $\overline{3}$ m	AISI type 304		Duplex Steel		ADI	
(1, 1, 1)	−0.8770	4.8730	−1.1020	5.5534	−0.9063	5.7919
(2, 0, 0)	−2.1914	8.7626	−2.3275	10.339	−2.1701	9.3606
(2, 2, 0)	−1.1597	5.7837	−1.2109	6.1637	−1.3393	6.8607
(3, 1, 1)	−1.5396	6.9464	−1.8176	7.8696	−1.6518	8.6992
(2, 2, 2)	−0.9210	5.0774	−1.1930	5.9382	−1.2099	5.9297
(4, 0, 0)	−2.0420	8.3331	–	–	–	–

* Unit given in 10^{-6}

Table 9 – The single-crystal elastic constants and the bulk properties of S235JR measured on SPODI [42].

Model	c_{11}^1	c_{12}^1	c_{44}^1	E^1	G^1	μ^2	ν	A*	$\frac{c_{12}}{c_{11}}$
I m $\overline{3}$ m									
Voigt[3]	199	142	90	235	82	−12.10	0.436	3.1	0.71
Reuss	240	118	106	214	84	−7.51	0.276	1.7	0.49
Hill**	230	121	121	210	82	−7.57	0.278	2.2	0.53
Kroener	229	129	109	207	80	−7.86	0.288	2.2	0.56
DeWit	184	89	120	203	84	−5.51	0.219	2.5	0.49
Matthies**	224	129	112	216	85	−7.24	0.27	2.5	0.57
Literature									
Martin Finkel [32]	232	126	115	220	86	−8.20	0.289	2.2	0.54
Gnäupel-Herold et al. [8]	225	122	121	217	86	−8.05	0.283	2.4	0.54
Adams et al. [5]	240	136	121	–	–	–	–	2.3	0.60
Kim et al. [6]	232	135	116	212	82	–	0.289	2.4	0.58

[1] Units are given in GPa

[2] Units are given in $\frac{1}{\text{TPa}}$

[3] For this model the fitting routine does not converge to a single solution

* The anisotropy is calculated after Zener [13]

** The anisotropy was fixed for this fit

Table 10 – The results of AISI type 304 (X5CrNi 18-10) austenitic stainless steel measured on SPODI. The texture data were measured on STRESS-SPEC [42].

Model	c_{11}[1]	c_{12}[1]	c_{44}[1]	E[1]	G[1]	μ[2]	ν	A**	$\frac{c_{12}}{c_{11}}$
F m $\overline{3}$ m									
Reuss	226	108	100	202	80	-7.85	0.271	1.7	0.48
Reuss*	225	107	100	202	80	-7.77	0.269	1.8	0.47
Hill	210	115	138	202	80	-7.85	0.271	2.9	0.55
Hill*	209	114	140	202	80	-7.77	0.269	3.0	0.55
Kroener	208	136	116	192	74	-8.97	0.300	3.2	0.65
Kroener*	205	139	124	194	75	-8.89	0.299	3.8	0.68
DeWit	212	130	121	204	80	-8.30	0.284	2.9	0.61
DeWit*	212	130	122	204	80	-8.27	0.284	3.0	0.61
Matthies	214	121	135	202	80	-7.85	0.271	2.9	0.56
Matthies*	213	120	136	202	80	-7.80	0.270	2.9	0.56
Literature									
Martin Finkel [32]	207	121	119	202	79	-9.76	0.296	2.8	0.59
Ledbetter et al. [4]	209	133	121	197	76	-8.27	0.290	3.2	0.64
Ledbetter et al. [3]	205	138	126	–	–	–	–	3.8	0.67

[1] Units are given in GPa

[2] Units are given in $\frac{1}{\text{TPa}}$

* For the fitting of the elastic constants the DEC texture adaptation was used

** The anisotropy is calculated after Zener [13]

$c_{44} = 115.2$ GPa, and obtained by Gnäupel-Herold [8], $c_{11} = 224.9$ GPa, $c_{12} = 122.2$ GPa and $c_{44} = 120.7$ GPa, using a similar steel and the same interaction model [42].

The agreement of Kroener's model is examplarily shown on austenitic steel AISI type 304 (X5CrNi 18-10) presented in Table 10. The values published by Ledbetter were obtained by ultra-sound measurements on single crystals [4] yielding $c_{11} = 209.0$ GPa, $c_{12} = 133.0$ GPa and $c_{44} = 121.0$ GPa were in good agreement compared to the values obtained in this work of 208.0 GPa, 135.7 GPa and 116.3 GPa for the isotropic approximation [42].

The results of the dual-phase alloy X2CrNiMoN 22-5-3 are shown in Table 11. The load transfer between given phases increases with increasing difference in the elastic properties. In case of the investigated dual-phase alloy the small differences in the single-crystal elastic constants resulted in a load transfer of only 0.3 %, not enough to change the elastic constants significantly. The high carbon amount in ADI forms a graphite phase of approximately 10 volume % besides the ferritic and austenitic phase. The graphite grains are shaped in form of nodules with Young's and shear moduli of essentially zero leading to an immediate plastic deformation on any amount of stress. Therefore the graphite phase was not considered for evaluation of the load transfer. The results presented in Table 12 are the effective elastic

Table 11 – The single-crystal elastic constants of X2CrNiMoN 22-5-3 duplex steel, the dual-phase stainless steel alloy measured on SPODI. The texture data were taken on STRESS-SPEC [42].

Model	c_{11}^1	c_{12}^1	c_{44}^1	E^1	G^1	μ^2	ν	A**	$\frac{c_{12}}{c_{11}}$
I m $\overline{3}$ m									
Reuss	227	121	70	165	63	−11.7	0.323	1.3	0.53
Reuss*	228	121	70	165	62	−11.8	0.324	1.3	0.53
Hill	218	125	81	165	63	−11.7	0.323	1.8	0.58
Hill*	219	125	79	165	62	−11.8	0.324	1.7	0.57
Kroener	221	126	76	167	63	−11.5	0.324	1.6	0.57
Kroener*	210	137	87	164	62	−12.1	0.331	2.4	0.66
DeWit	214	126	79	165	63	−11.7	0.323	1.8	0.59
DeWit*	206	117	78	164	62	−11.4	0.314	1.8	0.57
Matthies	217	126	82	166	63	−11.7	0.322	1.8	0.58
Matthies*	219	125	79	165	63	−11.8	0.324	1.7	0.58
Literature									
Martin Finkel [32]	210	108	83	177	69	−9.9	0.296	1.6	0.51
Kim et al. [51]	222	144	114	194	74	−11.8	0.317	2.9	0.65
F m $\overline{3}$ m									
Reuss	203	103	89	177	70	−9.62	0.284	1.8	0.51
Reuss*	208	107	88	178	70	−9.75	0.288	1.7	0.51
Hill	189	110	129	177	70	−9.62	0.284	3.3	0.58
Hill*	194	114	125	178	70	−9.75	0.288	3.1	0.58
Kroener	198	109	105	190	75	−7.85	0.272	2.4	0.55
Kroener*	189	120	120	190	74	−8.17	0.279	3.5	0.63
DeWit	222	154	112	186	71	−1.10	0.324	3.3	0.70
DeWit*	221	156	110	183	69	−11.40	0.328	3.4	0.70
Matthies	197	117	119	178	70	−9.66	0.286	3.0	0.59
Matthies*	201	119	116	179	70	−9.74	0.290	2.8	0.59
Literature									
Martin Finkel [32]	189	110	125	198	79	−9.61	0.285	3.2	0.58
Kim et al. [51]	207	134	114	188	72	−12.29	0.311	3.1	0.65

[1] Units are given in GPa

[2] Units are given in $\frac{1}{\text{TPa}}$

* For the fitting of the elastic constants the DEC texture adaptation was used

** The anisotropy is calculated after Zener [13]

constants with a 10 volume % graphite phase present [42]. All tables reveal discrepancies in c_{44} for the different interaction models resulting in larger deviations of the Zener anisotropy A [13] and the $\frac{c_{12}}{c_{11}}$ ratio. c_{44} is related to the shear stresses/strains and is only indirectly accessible during tensile/compression diffraction experiments by covering the strains for different orientations. Torsion experiments as suggested by Woraczek et al. could improve the accuracy [52, 42]. However, in a systematic study of the single-crystal elastic constants on different monocrystals of austenitic stainless steels and Fe-Cr-Ni alloys Ledbetter found that the values $A = 3.53$ and $\frac{c_{12}}{c_{11}} = 0.635$ remain nearly constant [4]. Both parameters are suited to serve as orientation which model fits the investigated alloy microstructure best and will ultimately lead to the most accurate results. A similar behavior is observed in the case of duplex steel where A varies significantly from 1.3 to 3.5. This has a large impact on the elastic properties. The left image in figure 42 shows the shear modulus of the austenitic phase while the right images shows the Young's modulus of the ferritic phase along different lattice directions for different grain-to-grain modelings. For both phases Kroener's grain-to-grain interaction model returns values for the Zener anisotropy closest to 3.53, the value published by Ledbetter. Relying upon Ledbetter's study leads to the conclusion that the most accurate elastic constants in duplex steel were obtained by Kroener's model. In the ferritic phase c_{11} was measured to 210 GPa, c_{12} to 137 GPa and c_{44} to 87 GPa and in the austenitic $c_{11} = 189$ GPa, $c_{12} = 120$ GPa and $c_{44} = 120$ GPa. In ADI the values obtained for A and the $\frac{c_{12}}{c_{11}}$ ratio differ significantly from the values found by Ledbetter. Therefore the influence of the of graphite phase in ADI is considered to be significant.

The influence of the texture on single phase materials during the evaluation is exemplarily shown on austenitic steel. The pole figures of the texture are shown in the work of Finkel [32]. The material is fiber textured an shows m.r.d values between 0.4 and 4. Taking into account the texture yield values of 204.8 GPa, 138.9 GPa and 124.2 GPa, for the respective single crystal elastic constants c_{11}, c_{12} and c_{44}. Similar results are found for the dual-phase X2CrNiMoN steel and ADI the average deviation varied from 0.5 % to about 3 % only, thus remaining below the uncertainties of the predicted constants. All tables reveal the average deviation of the single-crystal elastic constants due to texture remains below 1 GPa for all grain-to-grain interaction models. Therefore assuming that the grain orientations are randomly distributed over the Euler space is adequate for the investigation [42].

Table 12 – The single-crystal elastic constants of austempered ductile iron consisting of ferrite, austenite and graphite measured on SPODI. The texture data were measured on STRESS-SPEC [42].

Model	c_{11}^1	c_{12}^1	c_{44}^1	E^1	G^1	μ^2	ν	A**	$\frac{c_{12}}{c_{11}}$
I m $\overline{3}$ m									
Reuss	232	107	88	195	76	−8.24	0.281	1.4	0.46
Reuss*	218	103	92	191	75	−8.23	0.274	1.6	0.47
Hill	220	113	104	195	76	−8.24	0.281	2.0	0.51
Hill*	204	110	120	191	75	−8.23	0.274	2.6	0.54
Kroener	228	104	90	197	77	−7.67	0.274	1.5	0.46
Kroener*	231	101	90	200	79	−7.24	0.266	1.4	0.44
DeWit	217	116	102	198	78	−8.00	0.279	2.0	0.53
DeWit*	216	115	102	198	78	−7.98	0.278	2.0	0.53
Matthies	220	114	105	195	76	−8.16	0.280	2.0	0.52
Matthies*	202	112	126	192	76	−8.06	0.270	2.8	0.56
Literature									
Martin Finkel [32]	201	124	108	185	72	−	−	2.8	0.62
F m $\overline{3}$ m									
Reuss	203	92	85	179	71	−8.59	0.269	1.6	0.46
Reuss*	204	94	85	179	71	−8.73	0.272	1.5	0.46
Hill	190	99	109	179	71	−8.59	0.269	2.4	0.52
Hill*	191	100	108	179	71	−8.73	0.272	2.4	0.52
Kroener	200	88	85	182	72	−7.65	0.259	1.5	0.44
Kroener*	205	91	84	182	72	−7.93	0.266	1.5	0.45
DeWit	184	105	103	179	71	−8.84	0.273	2.6	0.57
DeWit*	183	104	103	178	70	−8.82	0.272	2.6	0.57
Matthies	193	101	105	179	71	−8.48	0.268	2.3	0.52
Matthies*	195	102	104	179	71	−8.62	0.271	2.3	0.53
Literature									
Martin Finkel [32]	192	102	96	180	71	−	−	2.1	0.53

[1] Units are given in GPa

[2] Units are given in $\frac{1}{\text{TPa}}$

* For the fitting of the elastic constants the DEC texture adaptation was used

** The anisotropy is calculated after Zener [13]
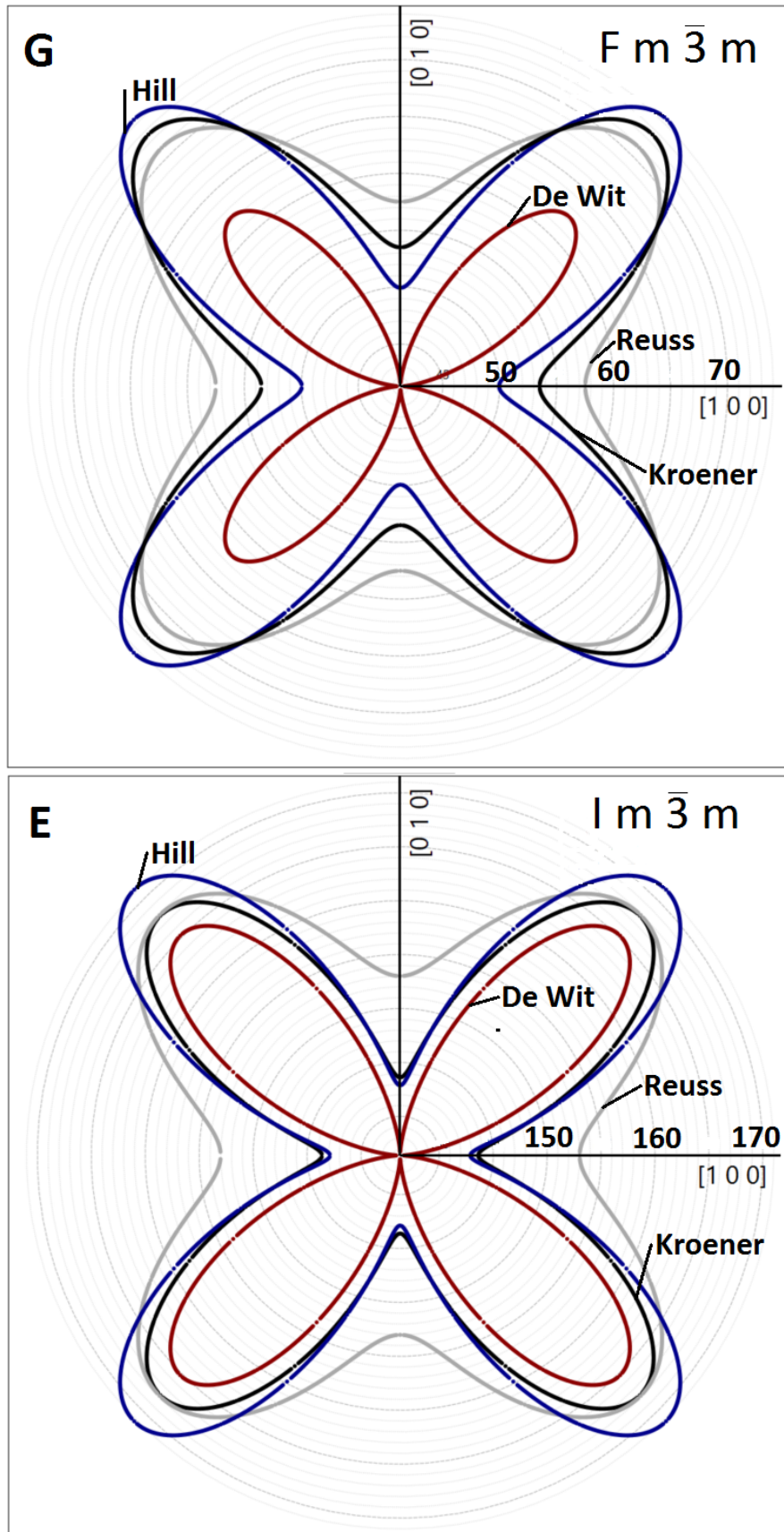
Figure 42 – The images show different elastic moduli of duplex steel along different lattice directions. On the top the shear modulus of the austenitic phase F m $\bar{3}$ m and on the bottom the Young's modulus of the ferritic phase I m $\bar{3}$ m is shown. The colors indicate the grain-to-grain interaction model used, the elastic constants are listed in table 11.

7.1.2 Elasto Plastic Self Consistent Modeling

EPSC modeling as described in section 6.3 is applied to predict the plastic behavior of the ferritic steel S235JR measured on STRESS-SPEC. This evaluation is performed to test the accuracy of the implemented model and show the potential for further extensions because of the extensive research already performed on ferritic structural steels it is best suited for accuracy and model testing. A full overview of the material is given in section 5.6. The averaging methods applied during the EPSC modeling are perfectly suited to calculate average lattice strains in the same way as diffraction techniques measure the average lattice strain along specific crystal directions. This reveals the stress state of each average grain including the stress state of orientations and lattice directions unavailable for diffraction experiments. This means the EPSC simulation complements the experimentally covered χ-orientations and gives access to the full state of stress in any direction of the sample or grain. Naturally, the averaging provides much faster evaluation times as common Finite Element Method modelings but at the cost of modeling freedom in terms of available sample geometry and precision.

Potential sources of uncertainties during the experiments are discussed for their influence on the overall results. Plastic deformation occurs when the applied macroscopic force surpasses a critical amount and remain constant over time. In this case the deformation is driven by small changes in the stress states of each grain interacting with each other. This means during non-continuous loading experiments additional strains will be introduced into the investigated sample. Depending on the scattering power of the sample a single diffraction pattern of a loading state can take from one to two minutes up to more than half an our. Other potential uncertainties arise from counting statistics and uncertainties of the tensile rig during the application of load, both of which are comparably small and any efforts to obtain better statistics beyond average counting statistic in the diffraction peaks will increase the experimental time significantly more than the gain of accuracy.

Figure 43 shows an example on how the applied force changes during the measurement of a load step to keep the macroscopic strain constant during the measurement in strain controlled mode. As illustrated the stress decreases by more than 20 MPa for covering four χ orientations during the experiment. Thus, the total uncertainty introduced by keeping the macroscopic strain constant during the measurement of each loading is about 25 MPa or 5%. The reason for this is the gravitational force acting on the force measurement device during rotation of the tensile rig as shown in Figure 26, the force is reduced by moving into horizontal position or increased the other way around by approximately 100N or about 2-4 MPa depending on the sample diameter.

In consequence during each loading step additional macroscopic plastic strains are introduced into the sample after reaching the plastic deformation during the measurement. This leads effectively to larger strains measured after reaching the yield stress resulting in a higher
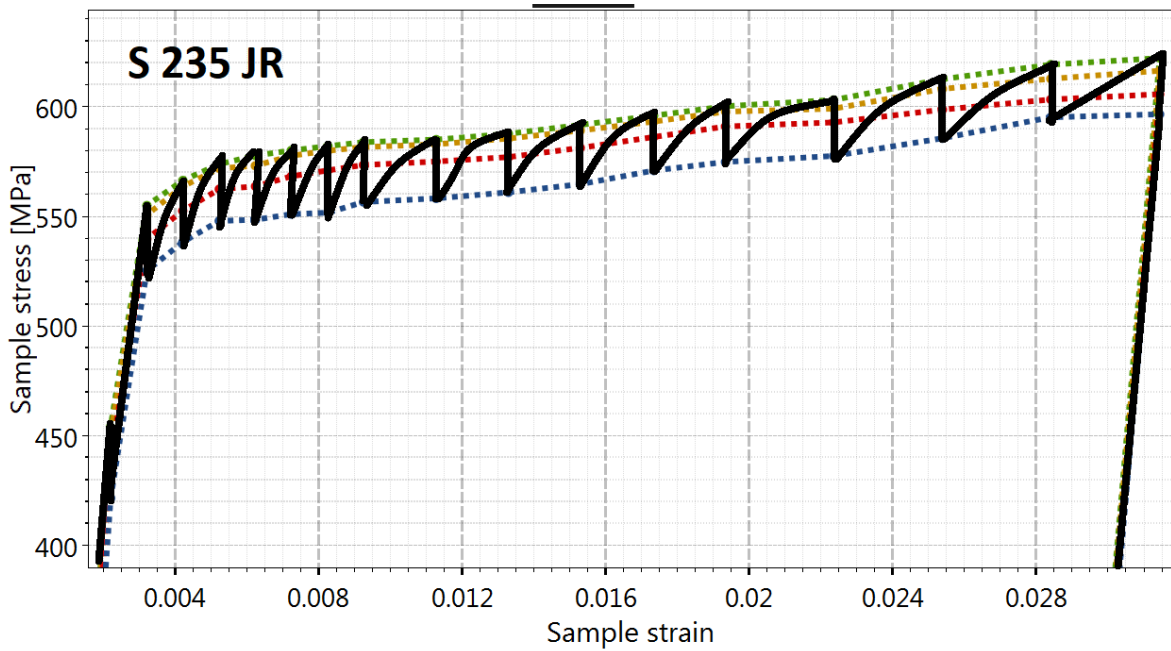
Figure 43 – The image shows the experimental macroscopic stress-strain curve in black of the (110) peak of S235JR for different χ orientations. The green line shows measured stress-strain curve for the horizontal sample position which was measured first. After each measurement the sample was tilt by additional $30°$ in χ and measured until the lateral contraction was reached indicated by the blue line. To keep the macroscopic strain constant at the input value during the measurement the stress is automatically reduced constantly by the tensile rig.

Table 13 – Input parameter for the different slip families of the EPSC simulation.

Slip Family	Yield Strength (MPa)	Hardening
$(110)\ [1\bar{1}1]$	225	100
$(211)\ [11\bar{1}]$	235	75
$(321)\ [\bar{1}11]$	410	500

curvature for the stress-strain behavior on sample level, especially at late deformation states. The theory and experiments show alike that by introducing plastic strains into any material will increase its total yield strength, thus the sample will show higher yield strength earlier into the experiment than expected. In other words after exceeding the yield stress the macroscopic stress-strain curve will appear to yield larger stress and in later stages of deformation it will show a higher strain rate than during continuous loading experiments. Figure 44 shows the effects compared to the EPSC modeling on the macroscopic stress-strain curve obtained during the diffraction experiment in horizontal position, it is identical to the blue line in Figure 43.

As described in section 4.9, the basic implementation of the EPSC modeling requires only few input parameters. At first the SCEC. In addition, each slip system is characterized by its yield stress and hardening parameters For the simulation of S235JR exhibiting s b.c.c. crystal structure three slip families were used to describe the deformation behavior. The

79
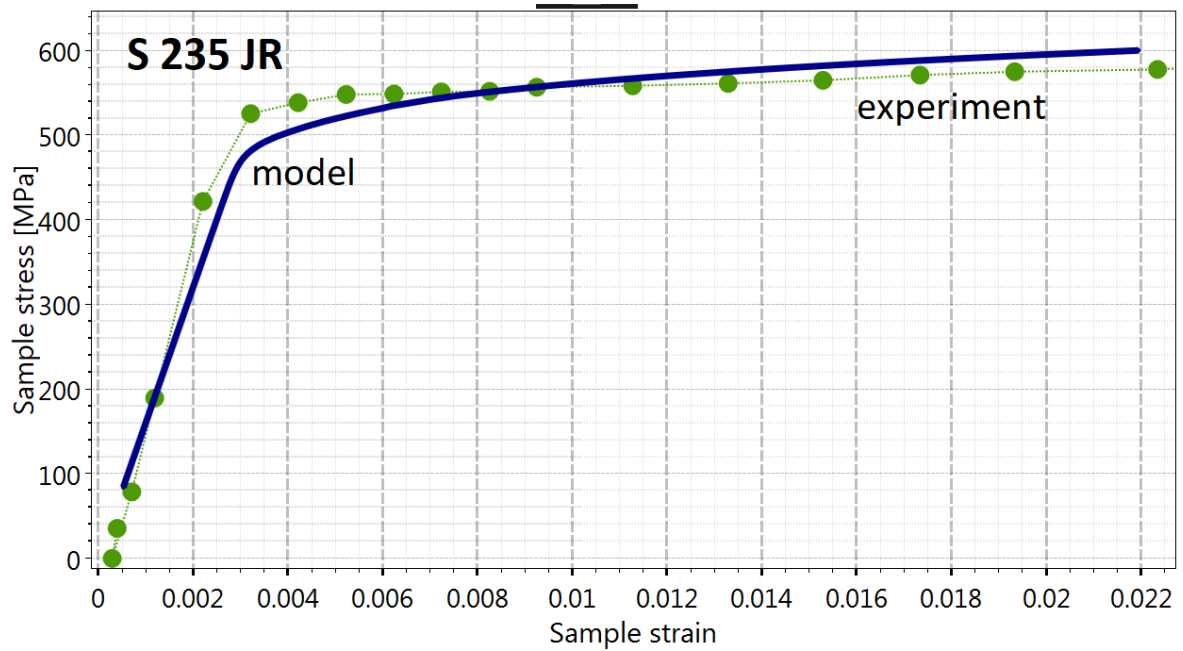
Figure 44 – The green dots are the measured macroscopic stress-strain values. The blue line shows the EPSC simulation. As expected the yield stress increases faster for the measurement than the prediction.

specific values of the yield strength and hardening for each slip family are listed in table 13. As the name S235JR suggests its yield strength of 235 in MPa is encoded into the name. At first 235 MPa were assumed for each slip family and later these values were refined to match the diffraction and macroscopic stress-strain relations best. The higher yield stress of the (321) slip plane is due the Schmid factor of the slip family. Figure 45 shows the slip activity over the macroscopic stress in which the (321) slip plane is activated first followed by (110) and (211). The slip activity in this context is defined as the ratio of active slip systems of one slip family compared to every possible-active slip system. The single-crystal elastic constants obtained by the Reuss grain-to-grain modeling from table 9 were used. They offered the best description of the elastic regime and the second best in the plastic regime compared to simulations with elastic constants obtained by other grain-to-grain interaction models. The best description in the plastic regime was achieved with constants obtained from the Hill model but the Young's modulus is underestimated. The main reason for the better agreement in the elastic regime is due to the averaging process which in this implementation essentially breaks down into the same assumptions as Reuss suggested while remaining below the yield stress. On the other hand the EPSC model follows the Hill approximation for the plastic regime during the grain-to-grain averaging.

Figure 44 shows the EPSC simulation together with measured macroscopic stress-strain relation. There is a mismatch between the Young's moduli of about 7%. Nevertheless the values show a reasonable agreement. The main discrepancies are found at the beginning of the plastic regime between 400 MPa and 550 MPa. In this regime the simulated values

are showing higher strain values than those from the diffraction data. As mentioned before additional hardening is introduced to the sample during the measurement. However, the model shows discrepancies beyond the hardening in the early plastic region which need to be improved in the calculation scheme. Lowering the yield stress of (321) and increasing the hardening values by several orders of magnitude better result may be achieved on macroscopic scale. This change in parameters however is causing strain rate drops in later stages of the estimated deformation. These drops are physically not reasonable and causing issues on grain scale which further suggests an unaccounted deformation mechanism. From Figure 44 the largest mismatch of the strain rate is found at around 1% strain but it rapidly adjusts to the correct strain rate resulting in slightly higher yield strength of approximately 20 MPa in this case. In comparison the applied force varied during each load step by about 25 MPa for the different χ and lattice orientations.

The next part focuses on the obtained microscopic data which includes measurements
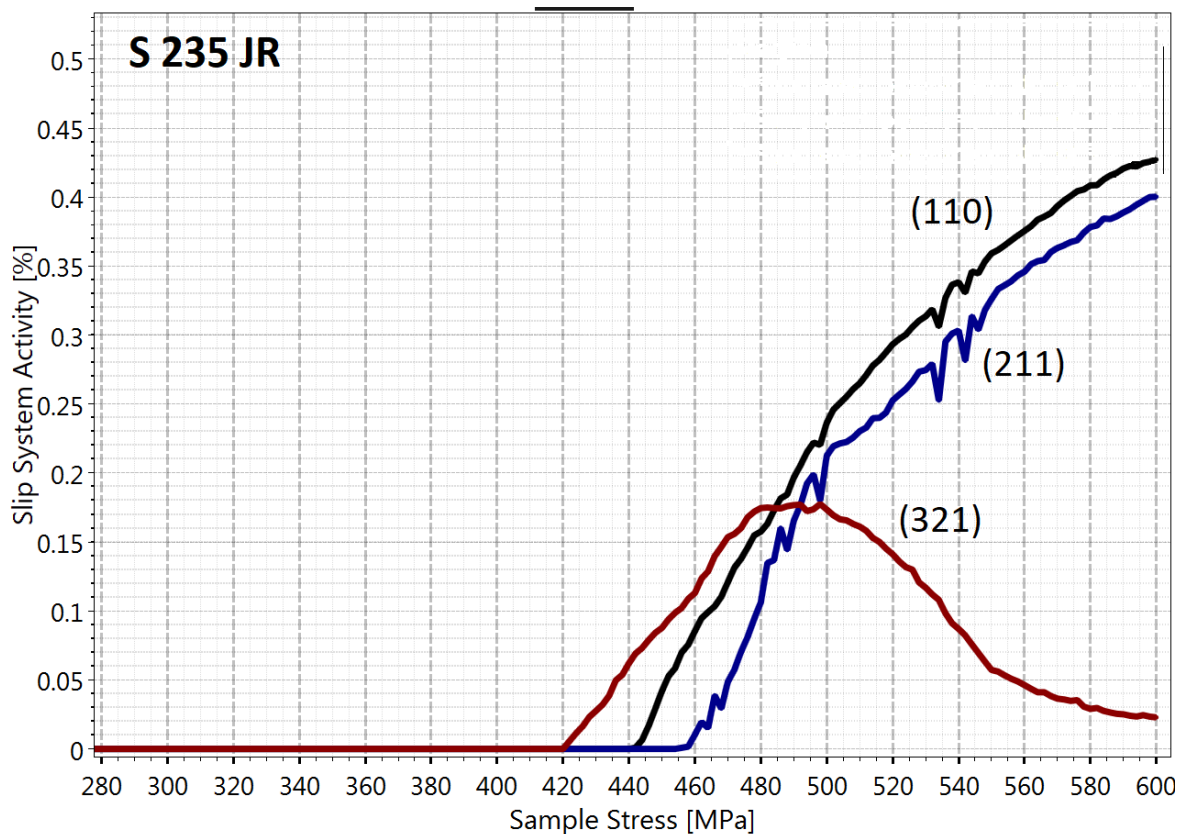
Figure 45 – The red line shows the (321) slip family which is activated first. Followed by the (110) slip family and finally family (211) is activated. The macroscopic strains are mainly caused by the slip on (110) and (211).

on the lattice straining during plastic deformation along lattice directions accessible by diffraction. This grants access to the activated slip systems and to the average stress state of the sample and grains during the measurement. Figure 45 shows the slip system activity during plastic deformation depending on the applied macroscopic stress. First the (321)

slip family is activated causing only a small increase in the sample strain rate at the early plastic deformation stage. 30 MPa later the (110) slip family is getting more and more active causing the first strong increase in the sample strain rate at the midpoint. The last slip family activated is (211) which starts to take over the (321) slip family due to a higher resolved shear stress on the individual slip systems. Therefore the (321) slip family starts to decrease its activity after 500 MPa. This take over process slows the increase in the strain rate down causing the earlier mentioned discrepancy in the strain rate at 1% strain. The slip family (211) is increasing the strain rate even further where the stress-strain curve is almost horizontal. In summary the (110) and (211) is mainly responsible for the plastic strains observed while the (321) slip family only causes small strains in the early stage of the deformation.

The upper image of figure 46 shows the longitudinal expansion for the (110), (200) and (211) planes. The experimental data shows the largest lattice strains, respectively stress, for the (200) planes and the (110) and (211) planes are located with about two thirds lower strains. The lower maximum strain in the (110) and (211) planes is caused by lower deformation resistance along these lattice directions. This behavior is typical for unstable b.c.c. phases because closest packed crystal structures are more preferable [53, 54]. Martensitic phase transformations from an open b.c.c. lattice structure to closest packed hexgonal or f.c.c. structures are achieved by a simple combination of displacements [53, 55]. For example the b.c.c. to hcp transition established by Burgers [56]: $(110)_{bcc}||(00.1)_{hcp}$ and $[\bar{1}11]_{bcc}||[\bar{2}10]_{hcp}$ is achieved by two equivalent shears of $(1\bar{1}2)[\bar{1}11]$ and $(\bar{1}12)[1\bar{1}1]$ deforming the b.c.c. octahedron into a hcp structure [55]. The EPSC model predicts the lattice strains of the (200) well within the uncertainties but shows some deviations by entering the plastic area. The experimental data shows a rather smooth transition into the plastic regime while the model predicts a more defined entry. By lowering the yield values of (321) and increasing its hardening by two orders of magnitudes a similar result may be achieved. This indicates further improvement of the modeling as suggested by Lorentzen where the EPSC model was improved by taking into account the stress pile-ups on boundaries for cyclic loading. This could improve the match to experimental neutron data because it accounts for the stres release during the measurement [57]. Hounkpati and Freour suggested further improvements on the modeling of intergranular strains at grain boundaries in presence of a small fraction of a second phase on β titanium alloys, their recent work could give access to improved results, as well [58]. The strains are predicted higher for (110) and (211) which indicate the models prediction is more isotropic than the measured diffraction data.

The lateral contraction for the same (110), (200) and (211) plains are shown in the lower image of figure 46. While the (110) and (211) plains are predicted well, the strains for the (200) show a difference. While the trend is captured well, the experimental data above
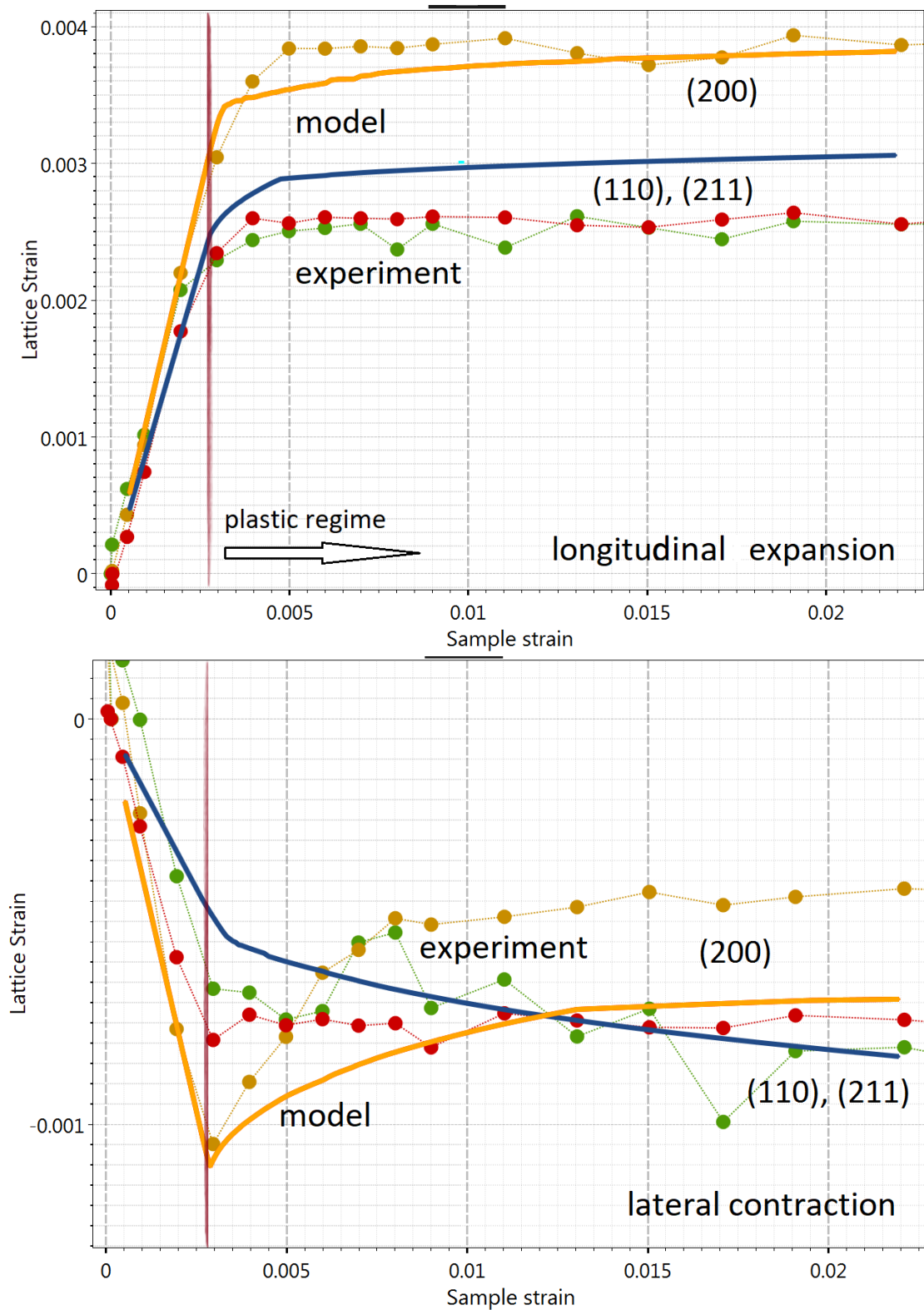
Figure 46 – In the upper graphic shows the longitudional expansion and the lower shows the lateral contraction. The red dots indicate the (110) plane which is the essentially identical to the (211) plane indicated by green. Yellow dots indicate the (200) plane. The lines are predicted by the EPSC model and yellow represent the (200) plane while blue indicates the (110) and (211) planes. The model predicts the trends well, for example the reduction of stress on the (200) plane after entering the plastic regime. However, it predicts a more isotropic behavior than the experimental data shows.

the elastic limit shows only two thirds of the strains predicted by the model. In conclusion the anisotropy for plastic strains is not captured well by the model. Other improvements as suggested by Kneer who relied on Kroener introduce a model which could improve the predictions regarding the anisotropy which was later used by Matthies to improve the averaging between Voigt and Reuss [16, 17, 29].

In the literature Daymond et al. applied a similar EPSC scheme during the investigation of a ferritic steel containing a small amount of graphite [59]. The ferritic steel shows a higher hardening rate as S235JR and enters the plastic regime about 50 MPa later. The literature values on stress-strain curve show essentially the same behavior at different hardening rates, after reaching the critical yield stress, the strain are evolving faster than observed during the experiment. In later stages of deformation the simulation reaches a maximum deviation at 0.8 % and catches up to the experiment again in the late stage of plastic deformation [59]. Comparing the findings obtained by diffraction to this analysis we again find the same behavior for each plane (110), (200) and (211). While the planes (110) and (211) are acting in the same way, (200) shows the lowest Young's modulus and highest yield during the tensile testing. Considering the lateral contraction the α-iron shows a similar decrease along (200) as this work shows with the difference that the effect in α-iron phase is more distinct [59].

In summary the EPSC framework predicts the observed deformation well and reproduces the observed stress states. In compliance with available literature the calculated macroscopic deformation shows minor discrepancies to the experiment at the beginning of the plastic regime. But contrary to the macroscopic prediction the lattice strains of the model and experiment match well in the early plastic regime but show a more isotropic straining in the late plastic regime along the (200) direction than experimentally observed in figure 46.

7.2 Titanium Alloys

A new self-consistent algorithm was used to incorporate the stress-distribution among present phases into the evaluation of multi-phase alloys. This section explains how the new method is applied to determine the single-crystal elastic constants of a dual-phase titanium alloy. It provides a detailed analysis of the morphology and texture. This analysis is needed to provide the necessary input parameters of the phases, the grain shape and phase fraction, for the calculation. Since no literature data of this alloy is known the accuracy of this evaluation is tested against the obtained single-phase values from a near α-alloy Ti64 and a pure β-alloy Ti38644 and show a very high level of consistency after applying the algorithm. The elastic values of the corresponding phases again are compared to available literature data [42].

7.2.1 Morphology and Texture
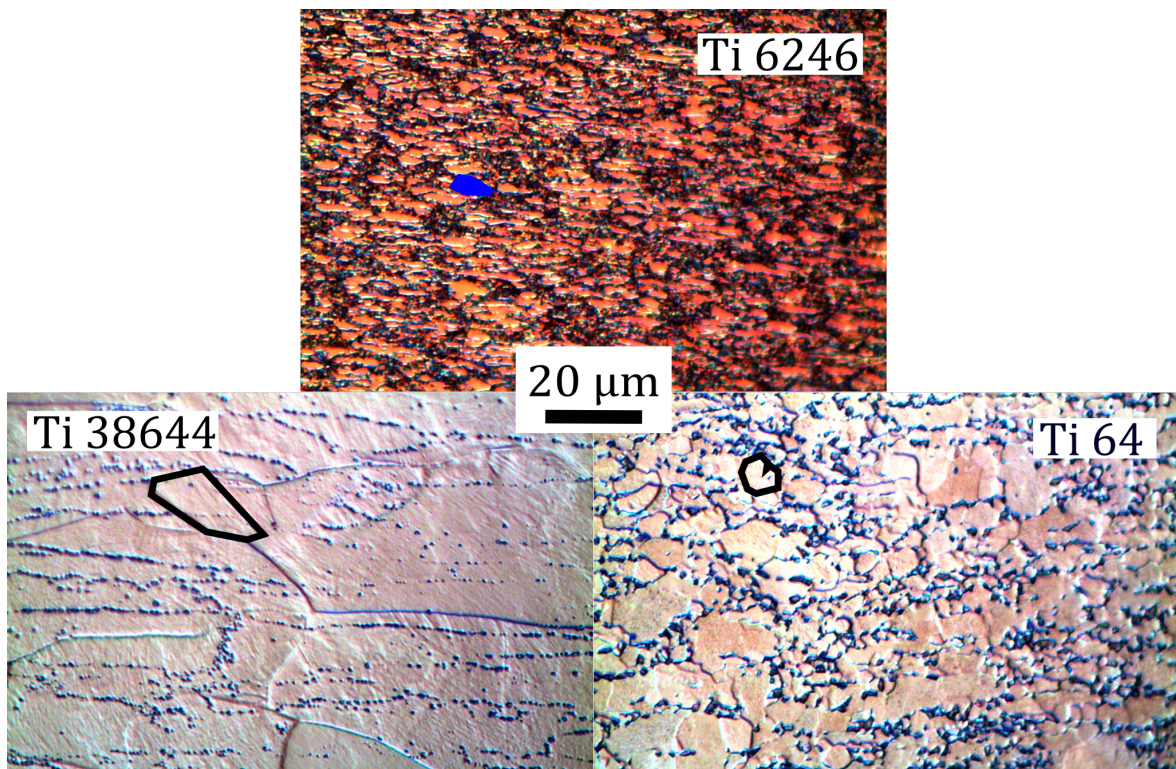
Figure 47 – Images of the surface of Ti64, Ti6264 and Ti38644 after etching all on the same scale. On the top Ti6246 is shown after 10s of etching. The lower left image shows Ti38644 after 30s of etching and the lower right image shows Ti64 after 20s of etching. The etching times are adjusted to reach the highest contrast to estimate the grain size. Example Grains are marked for each sample.

The morphology of the samples have been investigated with an optical microscope. Figure 47 shows a selection of images from the surface of Ti64, Ti6264 and Ti38644 after different etching periods. The average grain size is found to be about 15 μm for Ti64 and roughly 30

μm in large spherical grains for Ti38644. The α phase of Ti6246 shows grain sizes of about 5 μm while the β phase contains much larger grains averaged to be 20 μm, see figure 48.
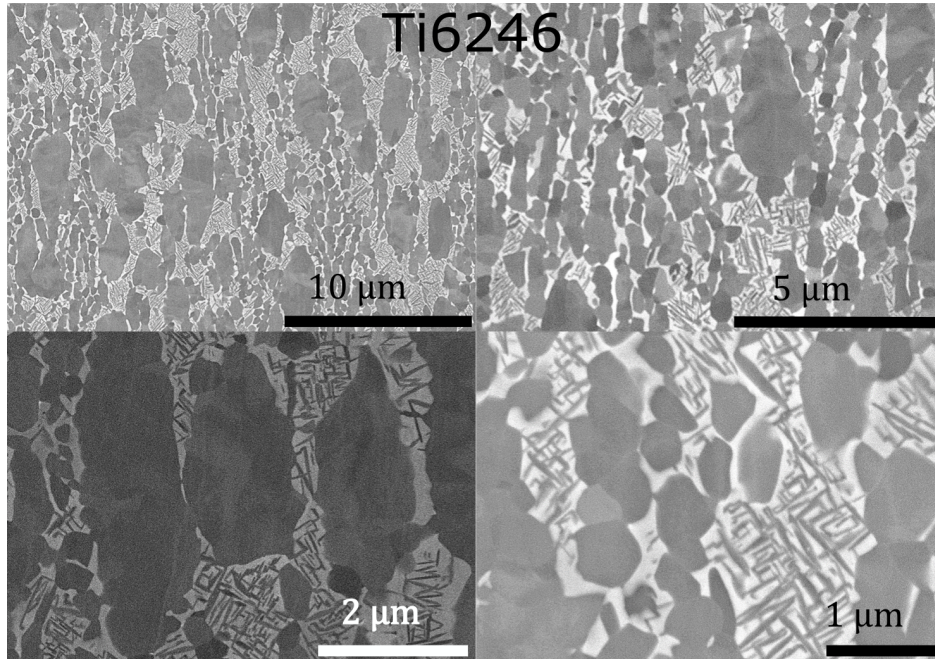
Figure 48 – Images of the surface of Ti6264 after ion polishing at four different scales: 10 μm at 5 keV, 5 μm at 3 keV, 2 μm at 3 keV and 1 μm at 5 keV.

Additional investigations on Ti6246 were done using EBSD and EDX. The sample surface was prepared with an additional step of ion polishing and different images of the surface along and perpendicular to the rolling direction were taken at different scales. Figure 48 shows the surface perpendicular to the rolling direction at four different scales, 10 μm, 5 μm, 2 μm and 1 μm.
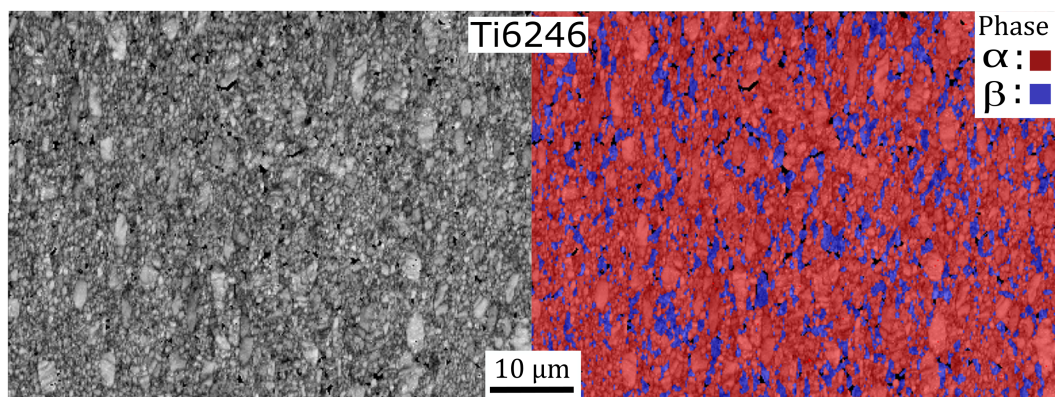
Figure 49 – An example image of the band contrast and the phase composition of Ti6246. The α phase is easily distinguished from the β phase resulting in high band contrast over all phases, left picture. On the right hand side the phase composition is shown, red corresponds to the α phase, while blue indicates the β phase
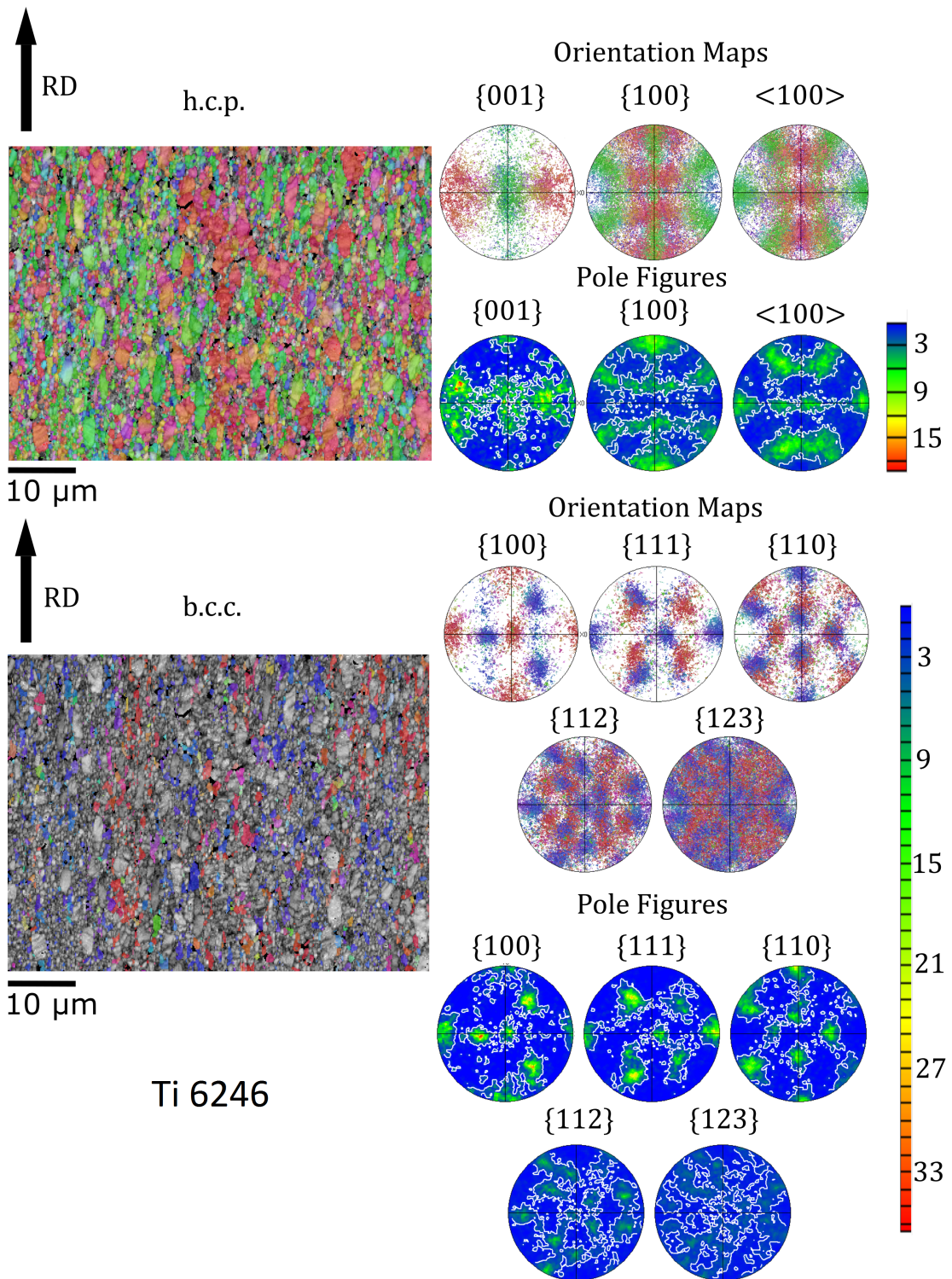
Figure 50 – The images on left show the color-coded orientation of the α phase and below the β phase acquired by EBSD. Next to these images on the right side the upper image shows the projection of the measured data. Below the pole figures of the {100}, {111}, {110}, {112} and {123} for α- and {001}, {100} and $\langle 100 \rangle$ for the β directions are shown.

The EDX analysis was carried out in standardless mode. The α phase is easily distinguished from the β phase resulting in high band contrast over all phases, see figure 49, left picture. The measured grain size 4.5 μm and almost 25 μm of the α and β phase agree well with the values measured optically. The β phase shows large spherical grains while the α phase contains small needle like grains. On the right hand side of figure 49 the phase composition is shown, red corresponds to the α phase and accumulates to a fraction of 78.4%, while blue indicates the β phase with 20.1%. The missing 1.5% could not be associated to any phase resulting in a phase fraction of 79.6:20.4 α:β. These values show excellent agreement to the values 78.4:21.6 evaluated from obtained diffraction patterns using Rietveld analysis (MAUD and FullProf suite) [60, 61].
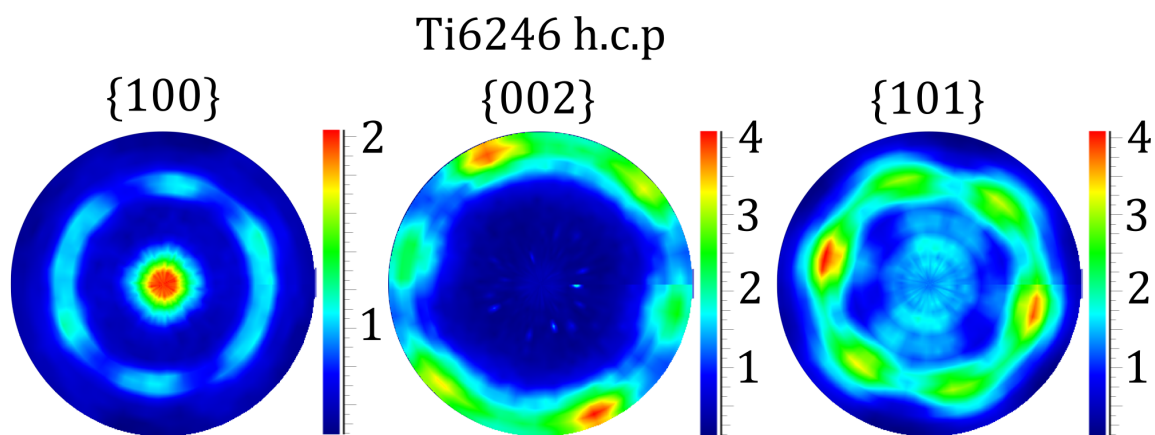
Figure 51 – The pole figures measured according to the orientations shown in figure 50 . The measurements were made on STRESS-SPEC [42]

Figure 50 shows the orientations of the grains in this section for the α phase, upper left, and β phase, lower left. The upper left shows the projection of the measured orientations and below shows the calculated pole figures. For the α phase the pole figures of $\{100\}$, $\{111\}$, $\{110\}$, $\{112\}$ and $\{123\}$ and for the β phase $\{001\}$, $\{100\}$ and $\langle 100 \rangle$ are shown. The overall texture is small never exceeding a m.r.d. value of 4 but the orientation along the rolling direction shows the largest values. Figure 51 shows a bulk measurement of the texture with neutrons on the instrument STRESS-SPEC. The pole figures are ordered according to direction and in both recordings the rolling direction shows the largest m.r.d. values. The neutron data for the respective β phase of the same measurement could not be evaluated because due to the low phase fraction and low scattering power.

The EDX shows the expected elemental composition, table 14, only the Al is slightly lower than expected. The doping of Al, Zr and Sn is homogeneous but Mo forms islands of approximately 7 μm of poor Mo content surrounded by Mo rich regions. The Mo content in the poor regions reaches a maximum of 2.8 wt% while even dropping to zero over large areas. In the Mo rich regions on the other hand the Mo content on average exceeds the average

Table 14 – The EDX results of Tl6246 show the overall composition compared to the Mo rich and poor regions. The other elements were homogeneously distribution over the measured sections [42].

	Overall			Mo poor regions	Mo rich region
	Weight %	σ	nominal	Weight %	Weight %
Ti	82.87	0.03	82	83-87.5	78.7-80.0
Mo	5.84	0.02	6	0-2.8	6.6-8.3
Al	5.39	0.01	6	5.6-6.5	4.6-5.1
Zr	3.84	0.02	4	3.5-3.6	3.9-4.0
Sn	2.06	0.01	2	1.8-2.4	1.9-2.1

overall value and varies between 6.6 and 8.3. An example section of the Mo distribution is given in figure 52. The Mo does not pile up in any specific phase nor does it have any other visible connection to the microstructure.
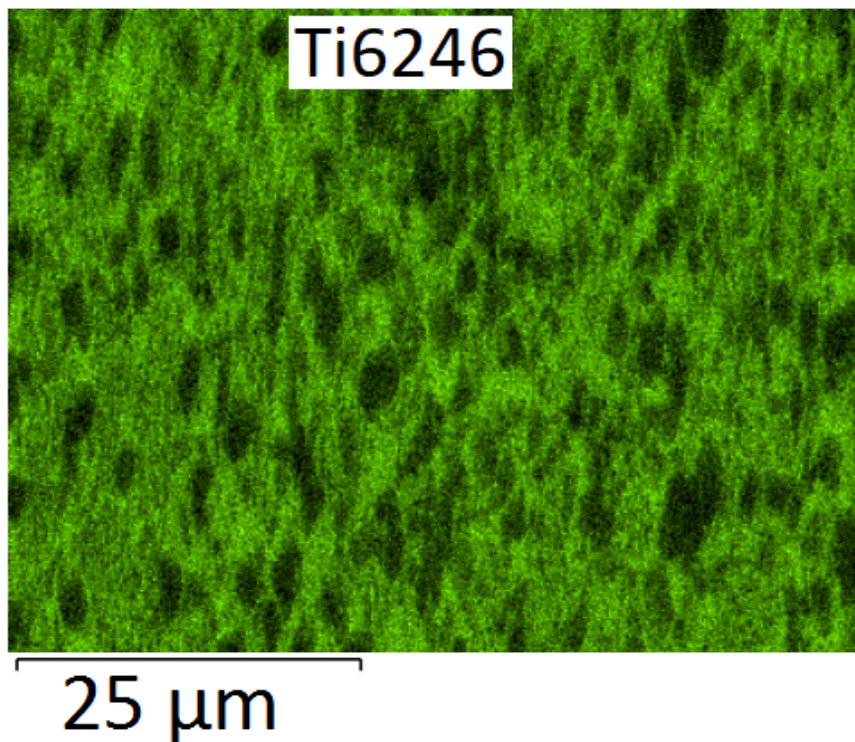
Figure 52 – The image shows the Mo distribution among a measured section from black where no Mo is found to green where high amounts of Mo are found [42].

7.2.2 Diffraction Studies

Diffraction studies of Ti64 and Ti38644 for the determination of single-crystal elastic constants were carried out on D20 (ILL, Grenoble), an example pattern of Ti64 is given in

figure 53. The dual phase alloy Ti6246 was measured with a synchroton experiment on the HEMS Beamline (Desy, Hamburg). The large grain size of the β phase in the dual phase alloy leads to only a couple of thousand illuminated grains. Effects of the low grain statistics are observed on the Debye Scherrer rings in figure 54. However, the estimated number of grains involved in the scattering process is higher than the predicted minimum amount of a couple thousands by Matthies [28] and the quality of the data reduction to 1-D Data sets in slices of $10°$ remained unaffected. The lowest intensity reflections have areas above 1000 counts and the peak position could be determined on average with an uncertainty below $0.0005°$.

The stress interval between the pattern during the continuous loading measurement was
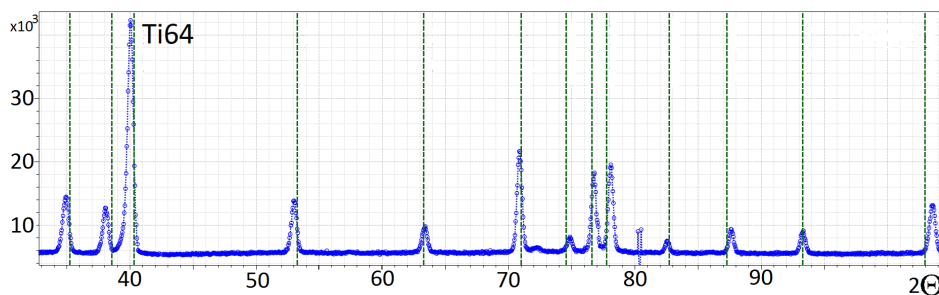
Figure 53 – A diffraction pattern of Ti64 measured on D20. 13 peaks of the α-phase where investigated during the experiment. No peaks from the β-phase could be observed.
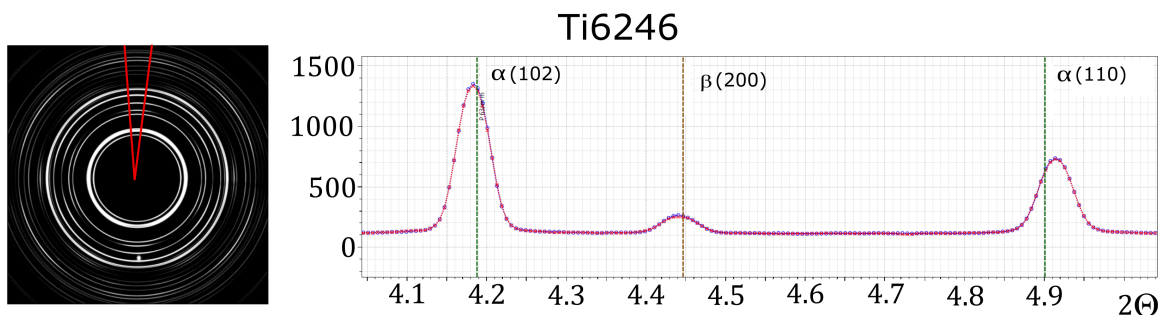
Figure 54 – A raw image of the data collected by the Perkin Elmer detector of Ti6246 measured on HEMS Beamline. The discontinuities in the β-phase are due to low grain statistics and texture. However, this does not affect the data reduction. The diffraction patterns on the right show the summation over the slices with lowest intensities in the β-phase. The peak shift is about $0.005°$.

set to 200 N. For such low stress rates the peak shift is about $0.005°$ and well above the uncertainties. Five DEC of the β phase and 16 of the α-phase could be evaluated and are listed in table 15. In total for the dual phase alloy about $94\,500$ peaks were evaluated. An example of the DEC obtained from the single and dual phase alloys is given in figure 55. The fit of the single phase alloys appears to be linear with no larger deviations over the different loading directions. The quality of the DEC in Ti6246 show minor non-linearities in

Table 15 – The DEC for different lattice planes measured in Ti38644, Ti64 and Ti6246.

	s_1*	$\frac{1}{2}s_2*$	s_1*	$\frac{1}{2}s_2*$
I m $\bar{3}$ m	Ti38644		Ti6246	
(1, 1, 0)	−3.483	14.897	−3.261	12.871
(2, 0, 0)	−4.983	18.437	−3.865	15.142
(2, 1, 1)	−3.725	14.659	−1.825	12.356
(2, 2, 0)	−3.319	14.241	−2.709	12.436
(3, 1, 0)	−4.426	16.402	−3.700	14.681
P 6(3) /m m c	Ti64		Ti6246	
(1, 0, 0)	−4.219	15.603	−3.468	13.425
(0, 0, 2)	−2.322	10.535	−2.569	10.184
(1, 0, 1)	−3.118	13.330	−2.788	12.379
(1, 0, 2)	−2.811	12.577	−2.672	12.379
(1, 1, 0)	−3.589	13.757	−3.222	13.048
(1, 0, 3)	−2.441	11.723	−1.729	10.878
(2, 0, 0)	−3.145	12.762	−3.485	12.495
(1, 1, 2)	−3.378	13.467	−2.835	12.495
(2, 0, 1)	−3.237	12.806	−3.103	13.059
(0, 0, 4)	−2.053	10.222	−1.786	10.282
(2, 0, 2)	−2.957	12.747	−2.800	12.672
(1, 0, 4)	−2.333	11.911	−2.092	10.675
(2, 0, 3)	−2.824	12.377	−2.808	12.240
(2, 1, 0)	–	–	−3.586	13.422
(2, 1, 1)	–	–	−2.212	11.777
(1, 1, 4)	–	–	−2.485	11.728

* Unit given in 10^{-6}

the data but due to the large number of peaks used for the evaluation the uncertainties remained small.

Tables 16, 17 and 19 reveal quite similar results for the different model assumptions. In addition, the values obtained for the $\alpha + \beta$ alloy Ti6246 agree quite well, especially if the load transfer is taken into account, with the corresponding data for the α phase in Ti64 and the β phase in Ti38644, respectively [42]. Table 16 also includes the results of Howard & Kisi (1999) on the Ti64 alloy determined by the Reuss (1929) approach, as well as values obtained by ultrasonic studies on single crystals of pure Ti measured by Fisher & Renken in 1964.

Good agreement with ultrasonic data was found in the hexagonal phases for c_{11} and c_{44}. The largest deviation between the results presented in this work and earlier work is found for c_{33}, and minor deviations in the c_{12} and c_{13} elastic constants. In hexagonal systems the behaviour in the ab plane is completely isotropic owing to the requirement for the $c_{66} = \frac{c11 - c12}{2}$ elastic constant. As c_{11} and c_{12} are determined accurately, this also gives access to the shearing parameter c_{66} . On the other hand, hexagonal systems show additional anisotropies regarding the c axis which influence the precision of parameters c_{12} and c_{13}. Similar elastic constants for α phases in different titanium alloys can be expected owing to the low quantity of alloying elements, shown already by the comparison of Howard & Kisi (1999) with pure titanium [31, 42].

In figure 56 the fitted single crystal elastic constants are shown for different grain-to-grain
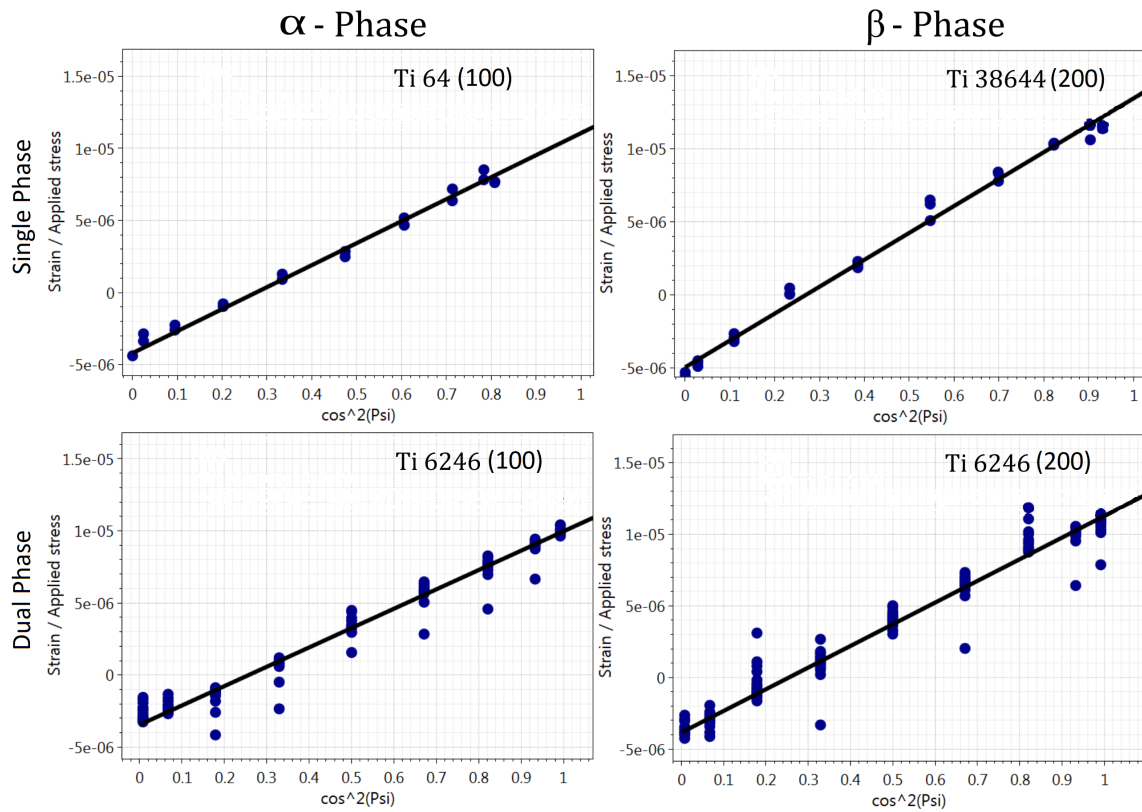
Figure 55 – The DEC of the single-phase alloys are compared to those of the dual-phase alloy. For the α phase the (100) plane and for the β phase the (200) plane is shown.

Table 16 – The single-crystal elastic constants of Ti64 measured on D20. Texture data were measured on STRESS-SPEC [42].

Model	c_{11}^1	c_{33}^1	c_{12}^1	c_{13}^1	c_{44}^1	E^1	G^1	μ^2	ν
P 6(3) /m m c									
Reuss	149	142	81	54	42	104	40	-16.9	0.303
Reuss*	150	137	83	53	42	103	40	-17.0	0.302
Hill	168	144	108	39	44	104	40	-16.9	0.303
Hill*	176	134	118	38	46	103	40	-17.0	0.302
Matthies	160	148	99	45	44	104	40	-16.9	0.302
Matthies*	173	136	113	41	45	103	40	-16.9	0.299
Howard & Kisi [31]	154	173	82	61	45	114	43	-15.9	0.307
Fisher & Renken [1]	162	181	92	69	47	116	44	-16.6	0.319

[1] Units are given in GPa

[2] Units are given in $\frac{1}{\text{TPa}}$

* For the fitting of the elastic constants the DEC texture adaptation was used

interaction and with applied texture weightings. Only minor influence of the additional texture analysis is observed in case of Hill's and Matthies grain-to-grain interaction model.

Table 17 – The single-crystal elastic constants and macroscopic values of Ti38644 measured on D20 and literature values of other titanium alloys containing a stable β phase [42].

Model	c_{11}^1	c_{12}^1	c_{44}^1	E^1	G^1	μ^2	ν	A*	$\frac{c_{12}}{c_{11}}$
I m $\overline{3}$ m									
Reuss	125	70	38	86	32	−23.91	0.337	1.4	0.56
Hill	120	73	45	86	32	−23.91	0.337	1.9	0.61
Kroener	120	69	39	88	33	−22.39	0.329	1.5	0.58
DeWit	117	72	43	86	32	−23.63	0.334	1.9	0.62
Matthies	120	73	45	86	33	−23.76	0.336	2.0	0.61
Freour et al.[34]	174	116	41	96	35	−25.16	0.382	1.4	0.67
Ledbetter et al.[62]	98	83	38	44	15	−64.61	0.418	4.50	0.83
Petry et al.[2]	134	110	36	55	19	−50.93	0.422	3.00	0.82
Raghunathan et al.[63]	140	128	50	36	13	−89.24	0.424	8.33	0.91
Raghunathan et al.[63]	165	118	45	89	32	−27.82	0.389	1.92	0.72
Hounktpati et al.[58]	154	110	42	84	30	−29.73	0.388	1.91	0.71

[1] Units are given in GPa, [2] Units are given in $\frac{1}{\text{TPa}}$

*The anisotropy is calculated after Zener [13], **Forged, ***Forged and aged
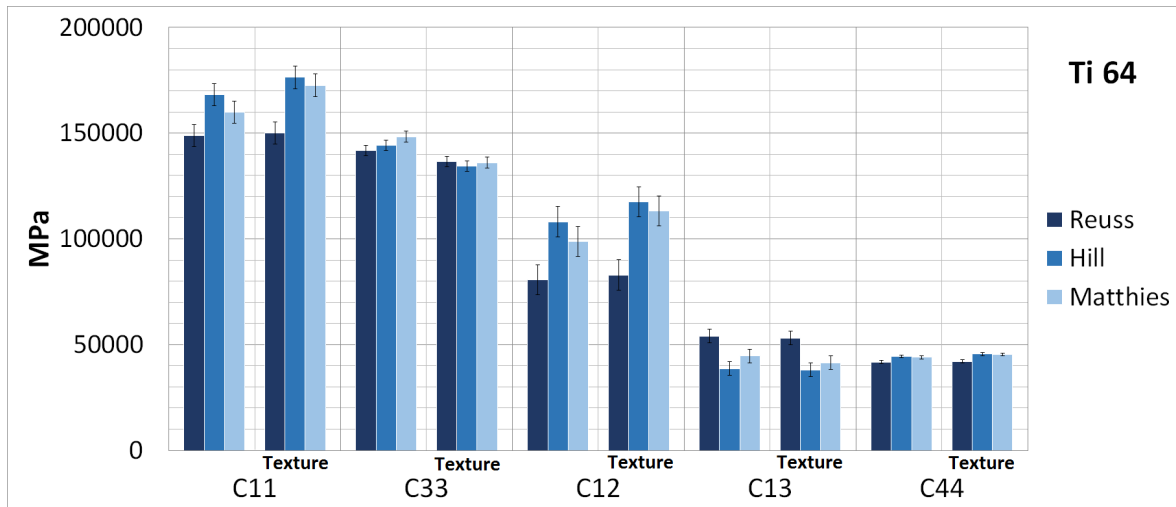
Figure 56 – Five different single crystal elastic constants are shown. Three grain-to-grain interaction models were applied and a texture weighting was tested. The texture only shows a small difference regarding Hill's and Matthies grain-to-grain interaction model.

It increases c_{11} and c_{12} and decreases c_{33} and c_{44}. Even though the effects are not large the texture may considerably influence the mechanical properties if occurring in a sharp, very distinct way, as for example experienced during additive manufacturing. Hounkpati et al., 2016 provided a comparison of single-crystal elastic constants for different β-alloys measured with different techniques in various conditions [58]. Significant variations in the elastic properties for β phases can be found in the literature, table 17. However, the results

Table 18 – A summary of the materials and techniques to investigate the elastic properties of the β-phase of titanium.

Name & Group	Composition w%	Phase	Method
Freour et al.[34]	Ti - Al 5 - Cr 4 - Zr 2 - Mo 4 - Sn 2	α, β	XRD
Ledbetter et al.[62]	pure Ti	β	Ultrasound
Petry et al.[2]	pure Ti	β	Phonons
Raghunathan et al.[63]	Ti- V 10- Fe 2- Al 3	β	Synchroton
Hounkpati et al.[58]	Ti - Mo 15 - Nb 3 - Al 3 - Si 0.2	α, β	EPSC

found in this work varied only little by applying different grain-to-grain interaction models, as shown in figure 57. In the literature two sets of constants were found in pure Ti alloys under elevated temperatures. First Petry et al. measured the phonon dispersion relation on in-situ grown b.c.c. Ti at 1020 °C in 1991 [2]. Later Ledbetter et al. reported a different set obtained via resonant ultrasound spectroscopy at 1000 °C in 2004. He could only access c_{11} and c_{12} directly and therefore calculated c_{44} by assuming different values for the Zener anisotropy [62]. Both Petry et al. and Ledbetter et al. obtained similar values regarding c_{44} which agree to values obtained in this work. The main differences are observed for c_{11} where Petry et al. show a better agreement with the results of the current work. On the other hand for c_{12} better agreement is achieved to the measurements of Ledbetter et al.. The previous measurements suggest a high Zener anisotropy value at high temperatures. All measurements performed at room temperature on the other hand show a significantly lower anisotropy. Except the measurement performed by Raghunathan et al. on forged Ti–10V–2Fe–3Al which shows an incredible high Zener anisotropy bigger than 8 resulting in a very low Young's modulus of only 36 MPa for this kind of material. Leading to the conclusion that higher temperature causes more anisotropic mechanical behavior of the β-phase in Ti. Another cause for the reduced anisotropy may be in the alloying elements. Ledbetter et al. and Petry et al. report Zener values of 4.5 and 3.0 on pure Ti while measurements on alloyed Ti report values near 2.0. To determine the exact contribution of either temperature or alloying on the anisotropy a more detailed study is needed to be performed. At room temperature Freour et al. estimated the single-crystal elastic constants of the β-phase by applying an explicit three-scale inverse self consistent model onto the dual phase Ti-17 alloy [34]. Elasto-plastic self consistent investigations have been performed by Hounktpati et al. on the dual phase alloy Ti-β21S. Both of which show quite high values for c_{11} and c_{12} compared to values obtained for Ti38644. The values of c_{11} agree much better to values measured in the dual phase alloy Ti6246 without taking into account the load transfer indicating that the calculation schemes used by Freour et al. and Hounktpati et al. are influenced by the second present phase and lead to "effective" single-crystal elastic constants.
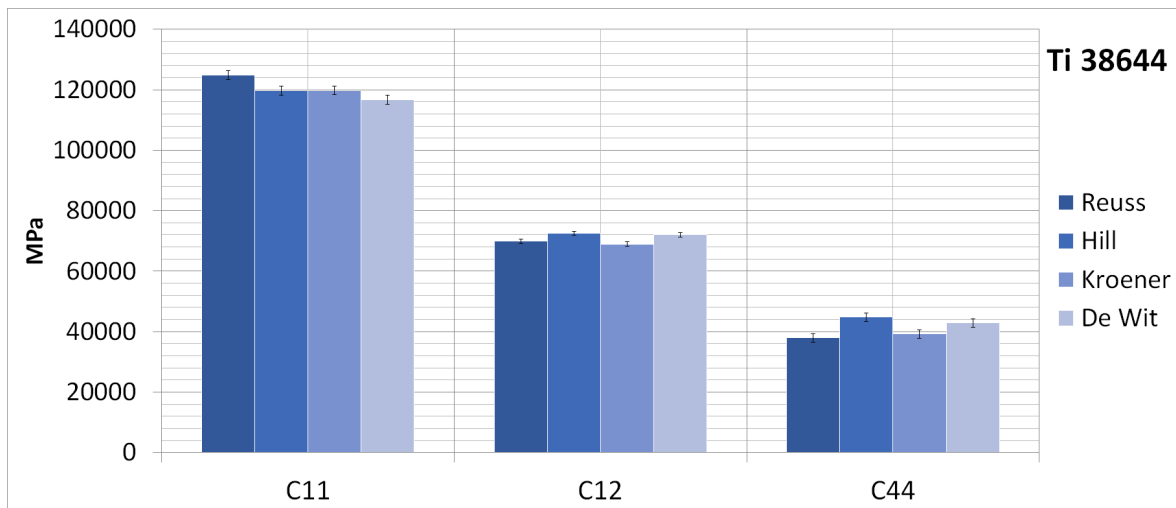
Figure 57 – All single crystal elastic constants of the β phase are shown for different grain-to-grain interaction models. The difference of the single-crystal elastic constants between the different interaction models is very small.

From the literature and the results of this work it can be concluded that the differences in the single-crystal constants arise from the presence of a second phase while the alloying elements contribute little to the observed discrepancies.

The load partitioning applied to the Ti6246 sample indicates a significant load transfer from the β phase to the α phase. The stress in the β phase is reduced by 11 % and transferred to the α phase, increasing its stress by 3 % (note that the smaller increase is mainly due to the ratio of phase fractions of around 1:4). The single-crystal elastic constants corrected for load transfer are shown in table 19.   Figure 58 reveals the impact of the load transfer approach on the resulting elastic constants in Ti6246. A clear shift of the values towards those of the single phase alloys can be observed [42]. In particular the load transfer corrected values for the β-phase in Ti6246 almost match the corresponding values in Ti38644. The impact of the load transfer in the β phase for the Reuss (1929), Hill (1952) and Matthies et al. (2001) models yields a change of about 10 % in most cases, whereas for the Kroener (1958) and de Wit (1997) models the changes in the elastic constants remain below 5 %. As illustrated c_{11} of the β phase was shifted from 143.8 to 124.3 GPa, c_{12} from 78.9 to 66.3 GPa and c_{44} from 43.1 to 37.8 GPa for the Reuss model. The single-phase values of 124.9, 69.9 and 38.0 GPa for the same model almost match the 'load-transfer-corrected' ones. Similar behaviour is also observed for all other models. Especially the obtained bulk properties match the single phase values more accurately, decreasing the Young's modulus in the β phase to 88 GPa. Owing to the lower increase in stress in the α phase the changes remain rather small, but the results achieved with the load transfer model match the single-phase values more consistently. The comparatively small changes in the elastic constants when using the Kroener (1958) and de Wit (1997) models are supposedly due to the assumption of inclusions in a matrix, which is essentially the same assumption as used for the load

Table 19 – The single-crystal elastic constants of Ti6246 which consists of a hexagonal α- and b.c.c. β-phase measured on P07 HEMS [42].

Model	c_{11}^1	c_{33}^1	c_{12}^1	c_{13}^1	c_{44}^1	E^1	G^1	μ^2	ν
P 6(3) /m m c									
Reuss	146	139	76	49	43	103	39	-17.7	0.311
Reuss*	150	144	78	51	46	106	41	-17.2	0.311
Hill	164	140	103	35	48	103	39	-17.7	0.311
Hill*	168	146	105	35	50	106	41	-17.2	0.311
Matthies	157	143	96	39	48	103	39	-17.5	0.309
Matthies*	162	149	98	40	50	106	41	-17.0	0.309
I m $\overline{3}$ m									
Reuss	144	–	79	–	43	99	37	-20.5	0.335
Reuss$^+$	124	–	66	–	38	88	33	-22.6	0.329
Hill**	138	–	82	–	50	99	37	-20.5	0.335
Hill$^+$	120	–	69	–	43	88	33	-22.6	0.329
Kroener	132	–	72	–	44	99	38	-19.0	0.320
Kroener$^+$	129	–	74	–	37	88	32	-23.7	0.342
DeWit	128	–	75	–	48	99	37	-19.6	0.323
DeWit$^+$	125	–	78	–	43	91	34	-22.6	0.338
Matthies**	138	–	81	–	50	100	37	-20.4	0.335
Matthies$^+$	119	–	69	–	43	88	33	-22.6	0.329

[1] Units are given in GPa

[2] Units are given in $\frac{1}{\text{TPa}}$

$^+$ Calculated with load partitioning

** The anisotropy was fixed for this fit

transfer.

7.2.3   The Plastic Deformation of Ti6246

The plastic deformation of Ti6246 has been investigated during the same diffraction experiment on the HEMS beamline by extending the tensile test beyond the elastic regime. As described earlier the small scattering angles of the synchroton radiation allows to capture full Debye Scherrer rings during a continuous measurement. This eliminates additional uncertainties caused by adjusting the load applied to sample to keep the strain constant during the collection at different sample orientations as shown in figure 43.

The macroscopic stress-strain relation in figure 59 shows a maximum yield of 1 300 MPa which is reached early on during the deformation at about 1% total strain. After reaching the maximum yield the total yield stress drops by 2% and remains nearly constant until more than 10% strain is introduced into the sample. The macroscopic behavior suggests
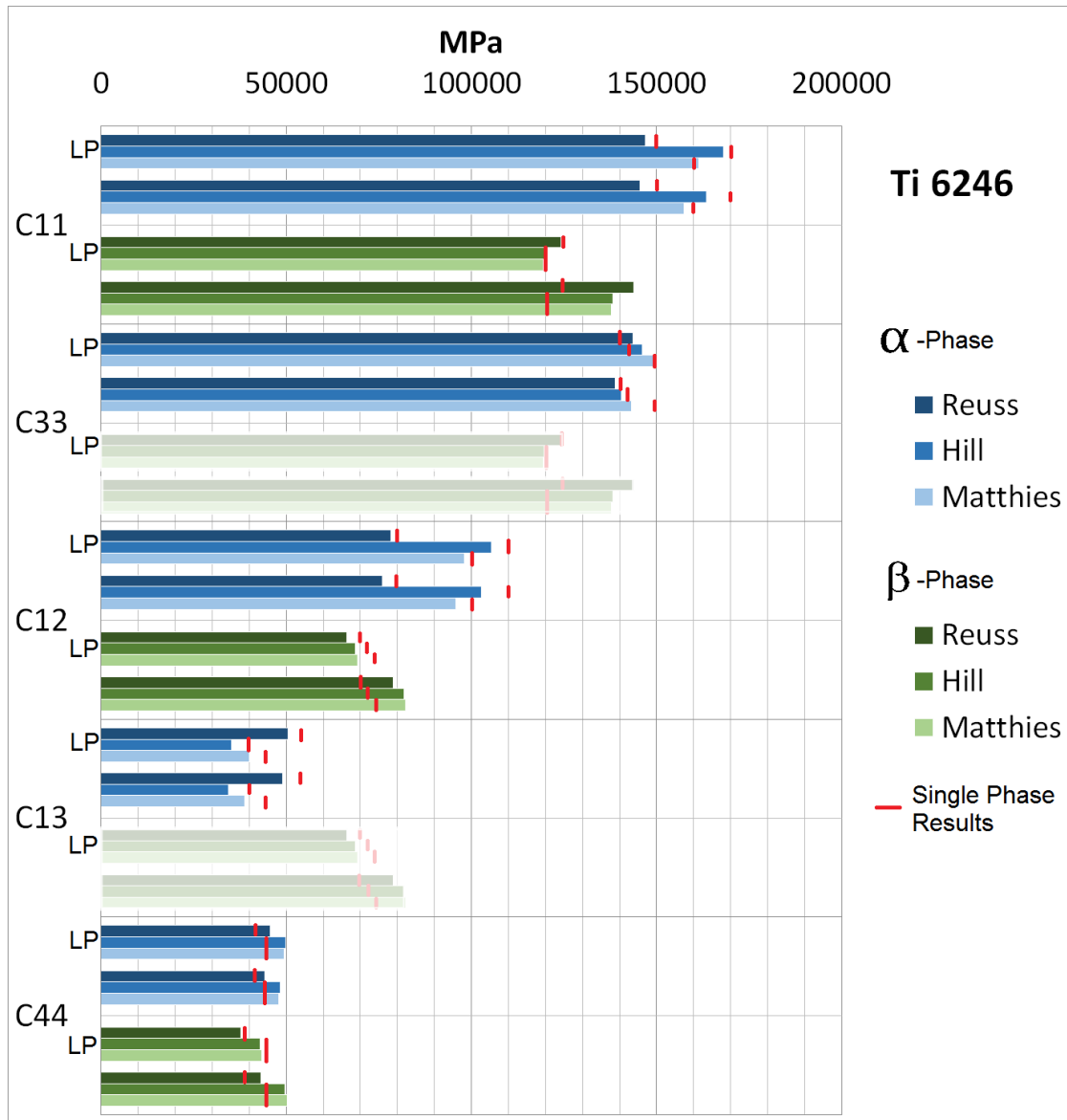
Figure 58 – The single-crystal elastic constants of the α- and β-phase os Ti6246 are compared to the results obtained from the corresponding single-phase measurements. For each single-crystal elastic constant two sets of columns are shown to compare the effective constant to the values obtained by applying the load transfer which is indexed by LP. The values measured in the corresponding single phase alloys are marked by red. For both phases a significant better agreement agreement to corresponding values is achieved by applying the load transfer.

that strain hardening is either very small or not present during the plastic deformation of Ti6246 indicating perfect plasticity or even strain softening.

The individual lattice strains of the α-phase planes (100), (002) and (101) and of the β-phase planes (110), (200) and (310) are shown in figures (60) and (61). The lattice strains of the longitudional expansion in the β-phase evolve more pronounced than those of the alpha-phase after reaching the plastic regime, indicating a larger load transfer between

Figure 59 – The macroscopic stress-strain of Ti6246 consisting of an α- and β-phase. The plastic regime starts after the applied load reached more than 1 100 MPa. The maximum yield is about 1 300 MPa. It is reached at the beginning of the plastic regime at about 1% strain. The macroscopic stress remains nearly constant until the strain reaches 10% and drops later as the diameter of the sample gets significantly smaller.

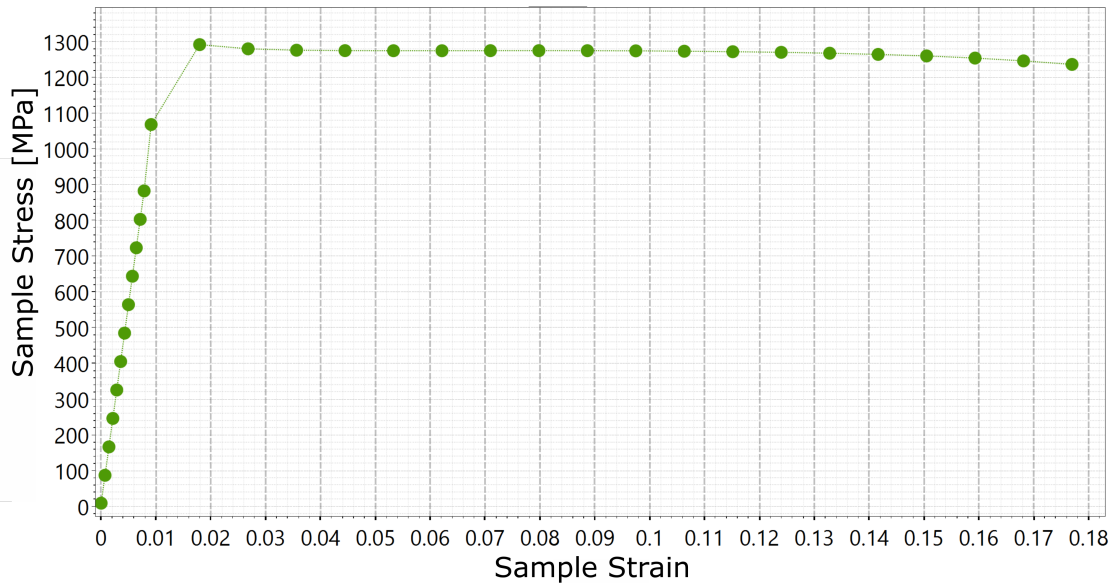different lattice directions in this phase. For the (002) peak of the α-phase the average strain is growing by 0.001 while the (200) peak of the β-phase increases by more than 0.002. Contrary to the β-phase the other lattice strains of the α-phase are decreasing by approximately 10% at the beginning of the plastic deformation suggesting that parts of the stress redistribution during the elastic loading is reversed at this point. After the stress redistribution in the α-phase is complete the strains of lattice plains are continuously growing until the macroscopic strain reaches more than 11% and the applied macroscopic stress is reduced significantly to keep the total strain rate constant. This behavior shows that during the early stages of deformation stress is piling-up in the average grains of both the α and β-phase. In the late stages of plastic deformation, above 11% macroscopic strain, the stress pile-up stops with one exception on each phase, the (002) peak of the α-phase which increases the stress in two steps and the (110) peak of the β phase, first decreasing the lattice strains and in the second phase increasing them again. This feature is most visible for the lateral contraction as shown in figure 61.

The refinement of the diffraction patterns at different deformation stages shows that the change in the peak area is only caused by the microstructural changes concerning the orientation of individual grains. Figure 62 shows the evolution of the peak area for different peaks during the plastic deformation. The increase of the area in the α-phase is mainly caused by twinning even if the β-phase grains prohibit twinning, but in the case of Ti6246 a large volume fraction of the α phase is not neighboring the β phase. The strong decrease of
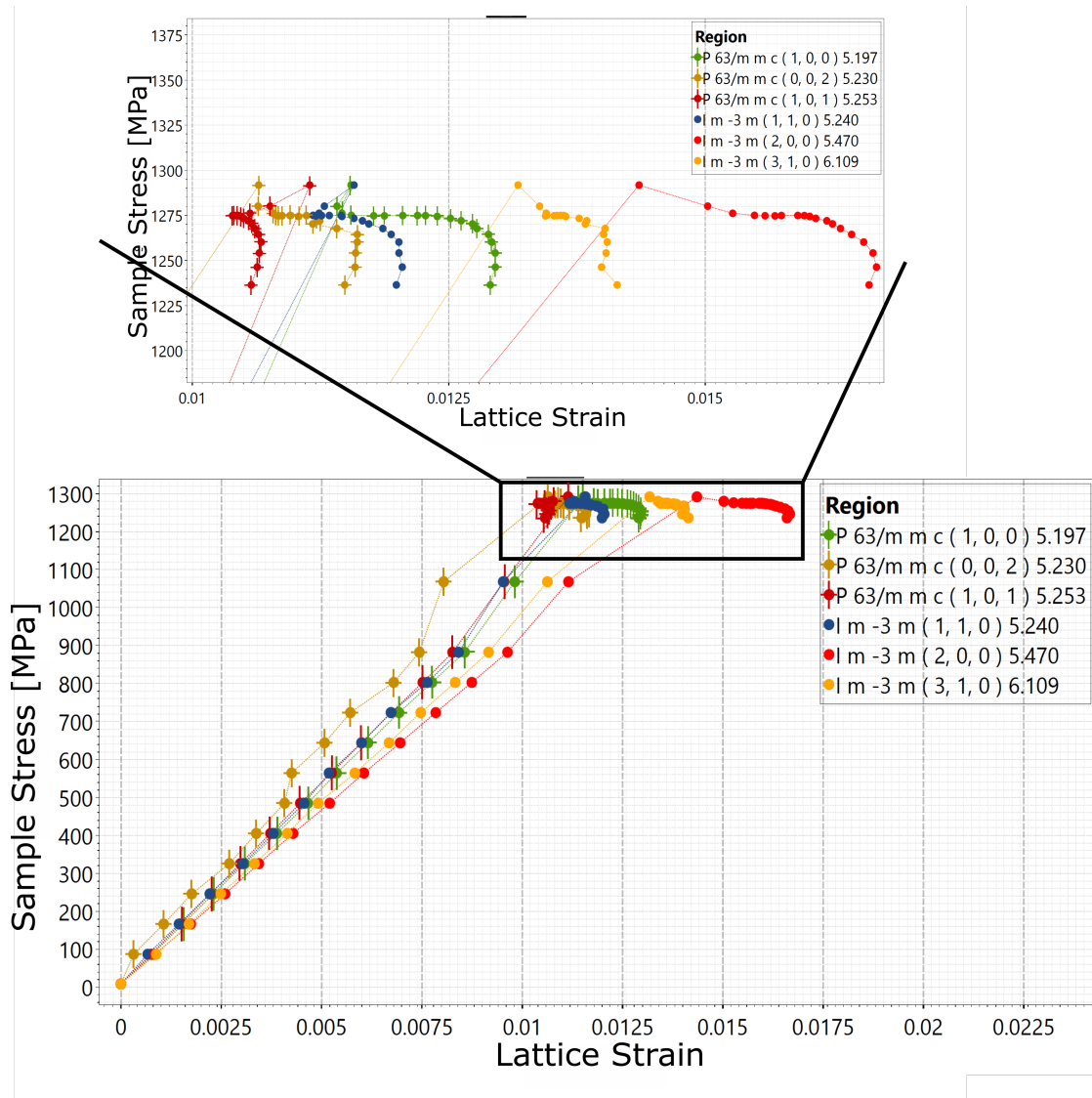
Figure 60 – The lattice strains of three peaks of the α- and β-phase. The (200) peak of the β-phase shows the largest lattice strains in the elastic regime and the strongest evolution of lattice strains after entering the plastic regime. The lattice strains caused by elastic deformation are getting smaller showing that the stress reduces for the (200) lattice plains during plastic deformation indicating a load transfer to other lattice directions.

the peak areas for β-phase is caused by microstructural changes resulting in a reorientation of the large grains or by parts of it after critical slip families are activated causing a stress relief by slip transfer in the late deformation stages. As the data obtained for the lattice strains suggest a large quantity of dislocations are piling-up in β-phase increasing the stress in this phase significantly. Figure 63 shows the increase in the Full Width at Half Maximum (FWHM) of the peaks over the sample strain. The FWHM in diffraction is coupled to micro strains, point-defect density and dislocation density if the microstructural effects are excluded. Because the grain size of both phases exhibits $1\mu m$ as shown in figure 48 the increase in the β-phase is mainly caused by dislocation pile-ups caused by the plastic deformation as
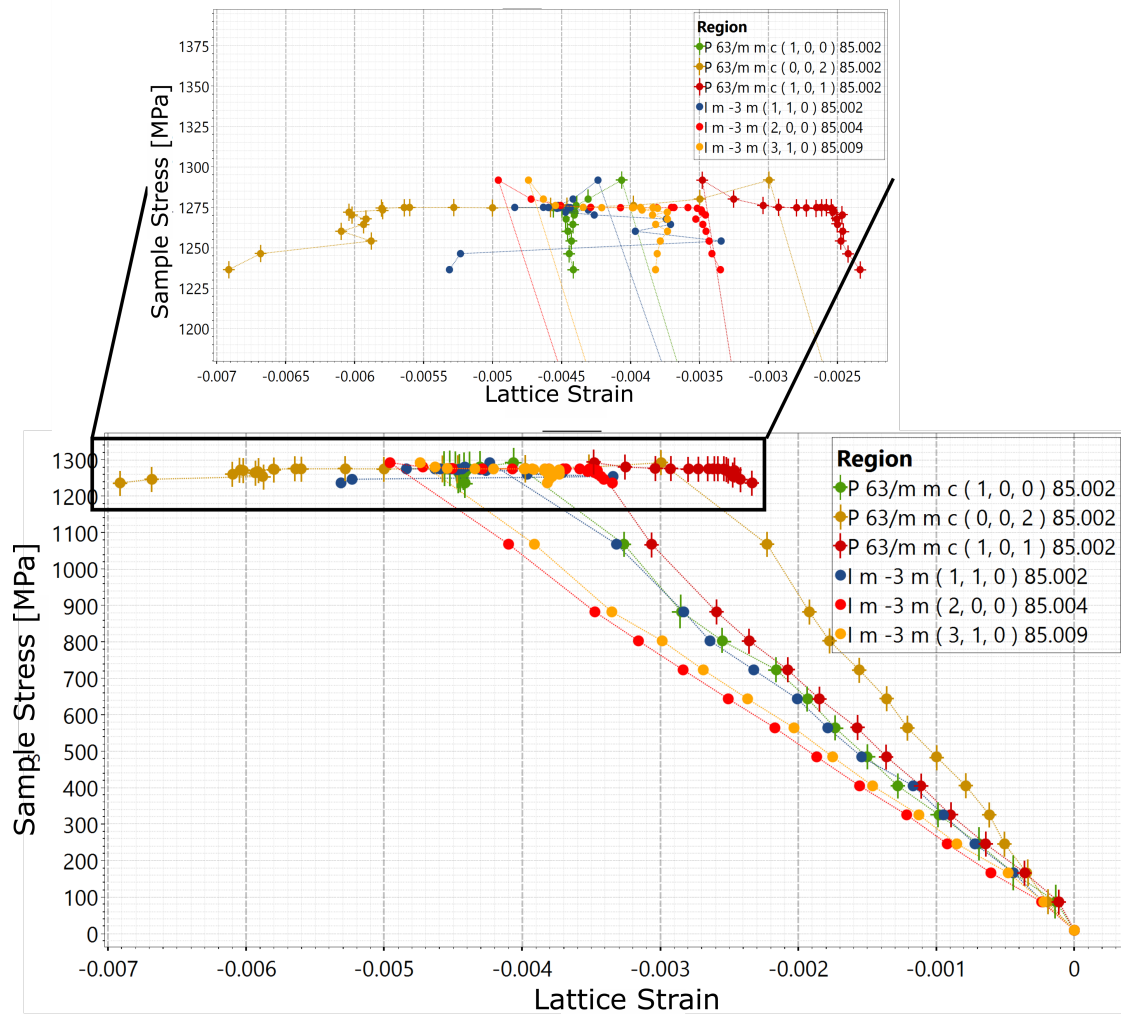
Figure 61 – The effects obsverved during the lateral contraction are very similar to those observed from linear expansion but are more pronounced. The lattice strains of the same three peaks of the α- and β-phase are shown. The effects on the (200) peak of the β-phase are mopre pronounced. The lattice strains caused by elastic deformation are getting smaller after entering the plastic regime showing that the stress reduces for the (200) lattice plains by introducing more plastic strains.

reported earlier in the literature [64]. The increase is large enough to accumulate significant quantities of stress in the grains decreasing their total yield. The effect on peaks measured in the α-phase is significantly smaller. They show only a small increase over all different stages of plastic deformation.

Figure 48 shows a microstructure typically formed by a slow cooling process from high temperatures on titanium alloys containing β-stabilizing elements. The α-phase forms from the β-phase in basket-weave structures with distinct alignment to the surrounding β-colonies. The orientation relation originates from the Burgers orientation relationship between the two phases, $\{110\}\beta/(0001)\alpha$ and $<1\bar{1}1>\beta/<11\bar{2}0>\alpha$ characterizing the transformation from the β- to the α-phase [65]. This microstructure promotes slip transfer across grain
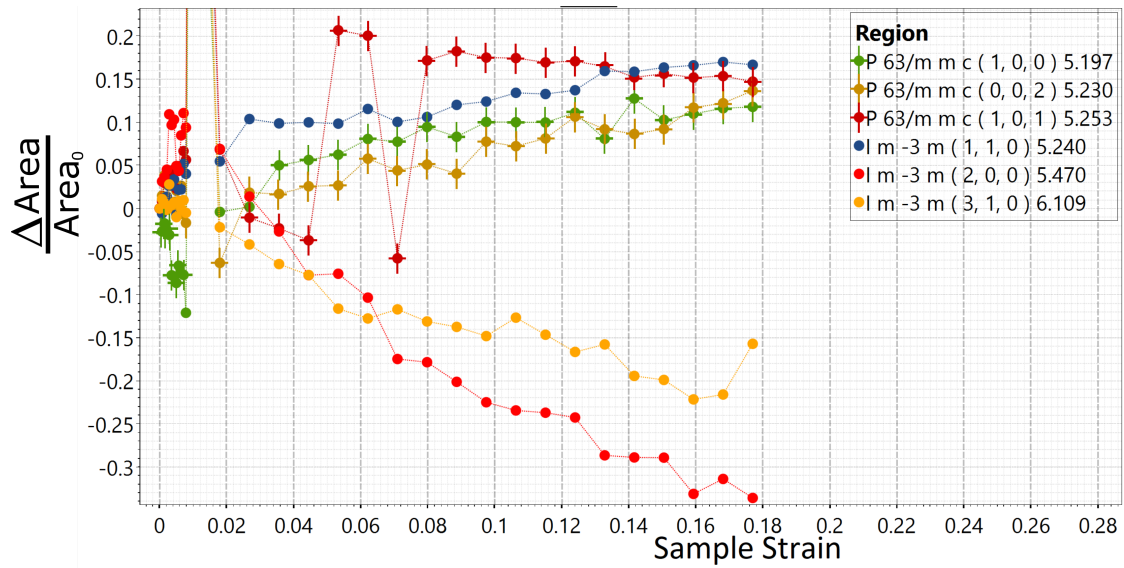
Figure 62 – The area increase of the observeg peaks over the sample Strain. The b.c.c. phase shows a light decrease of the peak are along the (200) and (310) lattice directions. The only increase is observed along (110). During the same time the area of the peaks is increasing suggesting strong microstructural changes during the deformation in the β-phase. The increase in the peak area for the α-phase is mostly caused by twinning.
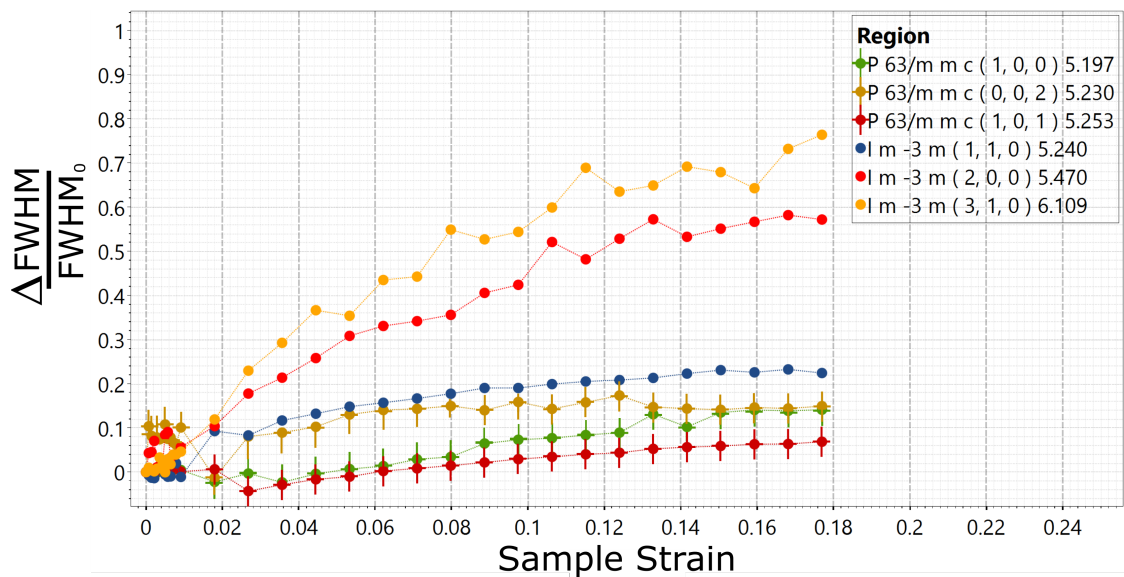
Figure 63 – The FWHM increase of the observed peaks over the sample strain. The b.c.c. phase shows a strong increase of the peak are along the (200) and (310) lattice directions resulting in large pile-up of dislocations. During the same time the area of the peaks is decreasing suggesting strong microstructural changes during the deformation in the β-phase due to additional stress.

boundaries as it sets the angle of intersection lines of possible active slip planes.

Figure 64 shows the lattice strain over the macroscopic strain of three lattice planes of the α- and β-phase of Ti6246 for the longitudinal expansion. The evolution of the lattice strains of the $\{110\}$ plane of the β-phase is very similar to the (0001) lattice plain of the
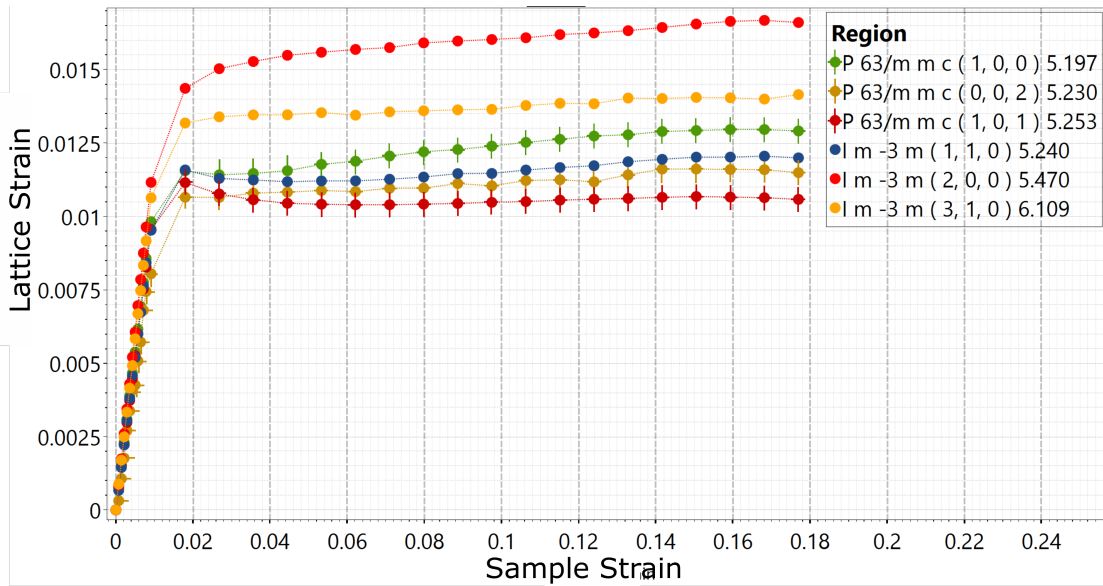
Figure 64 – The lattice strains of three peaks of the α- and β-phase for linear expansion. The β-phase shows higher average lattice strains than the α-phase. The strains of the$\{110\}$ lattice plane of the β-phase is very similar to the (0001) plain of the α-phase. It is getting smaller after entering the plastic regime and remaining constant until the macroscopic strain reaches 9% indicating slip activity during this period. The strains then increase again until 15% after which slip activity increases again.
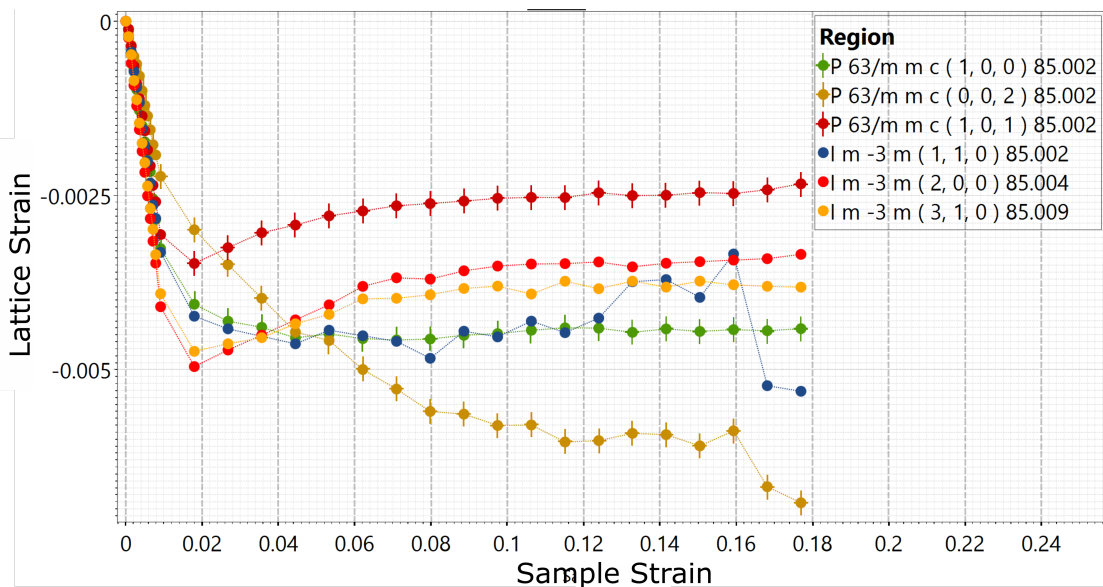
Figure 65 – The lattice strains of three peaks of the α- and β-phase for the lateral contraction. The β-phase behaves differently compared to iron because the lattices strains of the (110) plane are getting smaller in late deformation stages. The α-phase shows the largest contraction along the c-direction. The strain evolution of the (002) lattice plane shows a large increase during early plastic deformation indicating a yield strength along this crystal direction.

α-phase indicating a similar slip activity along these orientations. The lattice strain evolution also shows that the α-phase shows basal slip during all stages of deformation and prismatic

slip starting only at late stages of deformation above 15% macroscopic strain.

Besides the correct alignment of individual grain slip transfer only occurs if the correct set of slip systems is activated in both phases at the same time minimizing the Burgers vector of grain boundary dislocations. The lattice strain evolution in the case of Ti6246 shows that the average stress along specific lattice directions is getting smaller in the late stage of deformation after the prismatic slip systems of the α-phase are activated. This indicates the slip transfer is caused by prismatic slips of the α-phase crossing to the (110) slip plane of the β-phase. A similar behavior is reported in the near α alloy Ti6246Si by Joseph et al. [64].

The lateral contraction of the lattice planes is shown in Figure 65. The stress pile-up in the early stages of plastic deformation causes pressure along the c-axis of the α-phase resulting in a large lattice strain rate of the (002) plane until the macroscopic strain reaches 13%. The β-phase behaves differently to the investigated b.c.c. iron phase. The decreasing strains along the planes (110) may be caused by the prismatic slip systems activated in the α-phase.

8 Conclusion

Diffraction techniques were used to determine the mechanical behavior of multi-phase alloys. A technique for the measurement of single-crystal elastic constants introduced by Gnäupel-Herold et al. was further developed to account for texture and possible stress distributions among different phases present in the material. The properties derived from the elastic measurements are further used as input to treat plastic deformation within the Elasto Plastic Self Consistent (EPSC) framework. In order to evaluate the diffraction data a special evaluation software was developed. The software was first tested for its accuracy and performance on ferrous metals. The technique was then applied to investigate different titanium alloys used in aerospace industry. The single-crystal elastic constants of the α and the β phase are measured on different single phase alloys and discussed with literature. The dual phase titanium alloy Ti6246 was investigated for its elastic deformation behavior and compared to the results achieved by single-phase measurements and for its plastic deformation behavior.

The software developed to evaluate the obtained experimental data is capable to determine the Diffraction Elastic Constants (DEC) and single-crystal elastic constants of materials consisting of f.c.c., b.c.c., h.c.p crystal structure or any combination of them. For this purpose the classical stress analysis is applied in reverse via fitting the elastic constants from measuring the lattice strains at specific applied stress states of the sample. The specific microstructures of the engineering materials investigated are taken into account by selecting one of five implemented grain-to-grain interaction models introduced in the theory section of this work. To account for the texture the software introduces weightings based on an input Orientation Distribution Function (ODF) for the different crystallographic directions measured during the diffraction experiment. The stress distribution in dual phase materials is calculated based on the elastic constants and assumed microstructure of each individual phase using a self-consistent approach based on Eshelby's inclusion theory. A natural extension to the elastic analysis via diffraction is offered by the EPSC framework suggested by Hutchinson which was implemented to describe the plastic deformation behavior. The software uses the obtained single-crystal elastic constants for the EPSC modeling of the plastic deformation and compares the results to diffraction or tensile data.

The accuracy and utility of the technique was tested on different ferrous metals. They are the perfectly suited candidates for that purpose as they are commonly used in industry and a large amount of characterizations are available. From the six grain-to-grain interaction models implemented Voigt prooved to be not useful for the evaluation since the strains are not uniquely defining the elastic constants and the algorithm tends to converge into multiple results depending on the starting values given. The Kroener and consequently the de Wit grain-to-grain modeling show minor gaps in the domain of the function. This follows

from the self consistent approach used to derive the shear modulus from a third degree polynomial. However, the gap in the domain does not influence the accuracy of the gained results but only increases the iterations needed to fit the single-crystal elastic constants.

The results of the grain-to-grain interaction models compare well to existing literature values. The differences between the grain-to-grain interaction models were significant enough and influence the overall results. Therefore it is essential to select the most suitable interaction model depending on the present microstructure of the material. For cubic materials the Zener anisotropy has proven to be a quite strong indicator for the result quality of the interaction model and can be used to qualify the result additionally to microstructure. In a similar manner but not restricted to cubic symmetries is the use of $\frac{c_{11}}{c_{12}}$. This relation is quite similar to the Zener anisotropy but may be used in hexagonal systems as well.

The influence of the texture was also tested on the ferrous metals. But for the investigated samples the use of additional weightings during the evaluation did not change the results significantly above the uncertainties. It is therefore adequate to assume a random orientation distribution among the grains while evaluating the single-crystal elastic constants in case of not strongly textured, i. e. multiple of random distribution values below 8. This results was also predicted by Matthies in 2001 but with the restrain of a sufficient number of grains taking part in the deformation process.

The EPSC framework introduced is perfectly suited for comparison to diffraction data. The averaging applied during the modeling can be modified to match the average strains measured during diffraction and reveals the stress state of prior inaccessible orientations and directions. In this work the framework was used to test the prediction of the stress-strain behavior of the steel S235JR. The simulation matches well with the experimentally observed data and literature data obtained on a ferrous dual-phase alloy. On sample level the macroscopic strain rate in the experiment is somewhat higher in the early plastic regime than predicted by the framework but in later stages of deformation they agree well. Contrary the diffraction data agree better in early stages of deformation because in later stages the simulation is more isotropic than observed experimentally. By including more deformation mechanisms the accuracy of the simulation may improve further on sample and on lattice strain level. Similar results are found in the literature for α-iron.

Titanium alloys are modern high performance alloys first used in the 1940's by the aerospace industry. The two most important phases of titanium are the α phase (h.c.p.) and the β (b.c.c.). Even though both phases are known for a while, reports on the single-crystal elastic constants of both phases show discrepancies to one another. Especially for the β-phase at room temperature where reported Young's moduli vary from 40 MPa to almost 100 MPa. This inconsistency originates from the thermodynamic instability of the β-phase and most samples investigated contained α-phase to different extends without properly taking it into account during the evaluation. In other cases the β-phase was stabilized at room

temperature by alloying. This work shows similar single-crystal elastic constants of this phase measured on two different titanium alloys with different evaluation approaches.

Modern engineering is improving many high performance alloys by using the properties of multiple phases and balancing them by modifying the phase fraction to best suit the working environment. Only diffraction techniques are able to deliver distinguishable experimental data in situ of all present phases. Since one phase influences the other for example by redistributing the stress only "effective" properties are measured during this kind of experiment. To be able to directly access the single-crystal elastic constants a self-consistent scheme to account for the load transfer is introduced into the calculation suggested by Gnäupel-Herold. It was successfully used to evaluate all 8 single-crystal elastic constants of the α and β phase of Ti6246 in a single experiment at once. The results are compared to measurements performed on single-phase alloys containing respective phases. The calculations show a large redistribution of the stress from β to the α phase shifting the single-crystal elastic constants to almost the values obtained by the single-phase measurements. This new method improves the accuracy and accessibility of elastic properties on high performance alloys greatly.

Further investigations of the plastic deformation of Ti6246 show very little strain hardening and the maximum applied stress is reached in the early stages of plastic deformation. Most of the measured lattice strains show continuous increase indicating a stress pile-up at the grain boundaries of the α- and β-phase. The stress pile-up can be observed along different lattice directions in both phases with only a few exceptions. In later stages of plastic deformation, at about 13 % sample strain this behavior changes after the basal slip in the α-phase is initiated. At this point in deformation the stress distribution between the phases has completely changed and the distribution valid in the elastic regime is reversed. The formation of the α-phase from cooling is restricted to certain orientations depending on the alignment of the neighboring β grains. This behavior promotes slip transfer between grain boundaries causing a reduction of the pilled-up stress in both phases. During this deformation phase the stress tensor in the grains is changing relieving stress along some lattice directions and redistributing it along others.

The presented diffraction techniques and evaluation methods offer a wide range of possibilities for further methods of characterization. The evaluation and comparison of the EPSC modeling to diffraction data could be improved by performing a classical stress analysis. The obtained values would help to further develop EPSC prediction models for the stress pile-up at grain boundaries as observed during the early stages of the deformation of Ti6246. These stress pile-ups are caused by a dislocation pile-up at the grain boundary and there have been efforts by different groups to incorporate these effects into the EPSC scheme [66, 67, 68, 69]. For a description of the stress release during slip transfer the theoretical work of these groups is of great importance because it allows an incorporation of the slip transfer at certain stages of modeling. The knowledge of the stress tensor development of

average grain gives the possibility to test the theoretical predictions against measured values and would validate the averaging principles applied to find analytical solutions.

9 Own References

Heldmann et al. "Diffraction-based determination of single-crystal elastic constants of polycrystalline titanium alloys",
Journal of Applied Crystallography, Vol. 52, Issue 5, pp. 1144-1156, 2019,
DOI: 10.1107/s1600576719010720.

Breitkreuz et al., "Quantitative Comperability of Heavy Ion and In-Pile Irradiation on UMo fuel Systems",
Journal of Nuclear Materials, 2018, Vol. 507, Pages 276-287,
DOI: 10.1016/j.jnucmat.2018.04.007

References

[1] E. S. Fisher and C. J. Renken, "Single-crystal elastic moduli + hcp to bcc transformation in ti,zr, + hf," *Physical Review A-General Physics*, vol. 135, pp. 482–494, 1964.

[2] W. Petry, A. Heiming, J. Trampenau, M. Alba, C. Herzig, and H. Schober, "Phonon dispersion of the bcc phase of group-iv metals. i. bcc titanium," *Phys. Rev. B*, vol. 43, pp. 10933–10947, 1991.

[3] H. M. Ledbetter, "Monocrystal-polycrystal elasric constants of a stainless steel," *Physica Status Solidi A*, vol. 85, pp. 89–96, 1984.

[4] H. M. Ledbetter, "Predicted monocrystal elastic constants of 304-type stainless steel," *Physica B+C*, vol. 128(1), pp. 1–4, 1985.

[5] J. J. Adams, D. S. Agosta, R. G. Leisure, and H. M. Ledbetter, "Elastic constants of monocrystal iron from 3 to 500 k," *Journal of Applied Physics*, vol. 100, p. 113530, 2006.

[6] S. A. Kim and W. L. Johnson, "Elastic constants and internal friction of martensitic steel, ferritic-pearlitic steel, and α-iron," *Materials and Science Engineering A*, vol. 452-453, pp. 633–639, 2007.

[7] V. Hauk and H. J. Nikolin, "The Evaluation of the Distribution of Residual Stresses of the I. Kind (RS I) and of the II. Kind (RS II) in Textured Materials," vol. 8, pp. 693–716, 1988.

[8] T. Gnaeupel-Herold, P. C. Brandt, and H. J. Prask, "Calculation of single-crystal elastic constants for cubic crystal symmetry from powder diffraction data," *Journal of Applied Crystallography*, vol. 31, pp. 929–935, 1998.

[9] W. Voigt, *Lehrbuch der Kristallphysik*. Teubner Verlag, 1928.

[10] W. Voigt, "Calculation of single-crystal elastic constants for cubic crystal symmetry from powder diffraction data," *Ann. Phys. u. Chem.*, vol. 38, pp. 573–587, 1889.

[11] A. Reuss *Zeitschrift für Angewandte Mathematik und Mechanik*, vol. 9, pp. 49–58, 1929.

[12] G. I. Taylor and C. F. Elam, "Bakarian Lecture: The Distortion of an Aluminium Crystal during a Tensile Test," *Proceedings of the Physical Society. Section A*, vol. 102, no. 719, pp. 643–667, 1923.

[13] C. M. Zener, *Elasticity and Anelasticity of Metals*. University of Chicago Press, 1948.

[14] R. Hill, "The Elastic Behavior of a Crystalline Aggregate*," *Proceedings of the Physical Society. Section A*, vol. 65, no. 5, pp. 349–354, 1952.

[15] J. D. Eshelby, "The determination of the elastic field of an ellipsoidal inclusion, and related problems," *Proceedings of the Royal Society of London. Series A. Mathematical and Physical Sciences*, vol. 241, pp. 376–396, aug 1957.

[16] E. Kröner, "Berechnung der elastischen Konstanten des Vielkristalls aus den Konstanten des Einkristalls," *Zeitschrift für Physik*, vol. 151, pp. 504–518, 1958.

[17] G. Kneer, "Die elastischen Konstanten quasiisotroper Vielkristallaggregate," *Physica Status Solidi (B)*, vol. 3, pp. 331–335, 1963.

[18] R. Hill, "Micro-Mechanics of Elastoplastic," *Journal of Mechanics and physics of solids*, vol. 13, pp. 89–101, 1965.

[19] R. Hill, "Theory of Mechanical Properties of Fibre-Strengthened Materials-III. Self-Consistent Model," *Journal of Mechanics and physics of solids*, vol. 13, pp. 189–198, 1965.

[20] R. Hill, "Generalized Relations for Incremental Deformation of Metal Crystals," *J. Eng. Mater. Technol.*, vol. 14, pp. 95–102, 1966.

[21] J. W. Hutchinson, "Plastic deformation of b.c.c. polycrystals," *Journal of the Mechanics and Physics of Solids*, vol. 12, no. 1, pp. 25–33, 1964.

[22] J. W. Hutchinson, "Elastic-Plastic Behaviour of Polycrystalline Metals and Composites," *Proceedings of the Royal Society A: Mathematical, Physical and Engineering Sciences*, vol. 319, no. 1537, pp. 247–272, 1970.

[23] V. Hauk and H. Kockelmann, "Ermittlung der Einkristallkoeffizienten aus den mechanischen und röntgenographischen Elastizitätskonstanten des Vielkristalls," *Zeitschrift für Metallkunde*, vol. 70, pp. 500–502, 1979.

[24] P. A. Turner, N. Christodoulou, and C. N. Tomé, "Modeling the mechanical response of rolled Zircaloy-2," *International Journal of Plasticity*, vol. 11, no. 3, pp. 251–265, 1995.

[25] B. Clausen, C. N. Tomé, P. Maudlin, and M. Bourke, "Self-consistent Modeling of Polycrystal Plasticity Polycrystal versus Continuum Constitutive Description," 2000.

[26] C. N. Tomé and E. C. Oliver, "Code Elasto-Plastic Self-Consistent (EPSC)," Tech. Rep. May, Los Alamos National Laboratory and CLRC Rutherford Appleton Laboratory, 2002.

[27] B. Clausen, C. N. Tomé, D. W. Brown, and S. R. Agnew, "Elastic-Plastic Self-Consistent Model Including Grain Reorientation Due to Twinning," *Los Alamos National Laboratory, University of Virginia, 13th Annual Meeting and Exhibition*, 2007.

[28] S. Matthies, H. G. Priesmeyer, and M. R. Daymond, "On the diffractive determination of single-crystal elastic constants using polycrystalline samples," *Journal of Applied Crystallography*, vol. 34, no. 5, pp. 585–601, 2001.

[29] S. Matthies, S. Merkel, H. R. Wenk, R. J. Hemley, and H. kwang Mao, "Effects of texture on the determination of elasticity of polycrystalline ϵ-iron from diffraction measurements," *Earth and Planetary Science Letters*, vol. 194, no. 1-2, pp. 201–212, 2001.

[30] R. De Wit, "Diffraction elastic constants of a cubic polycrystal," *Journal of Applied Crystallography*, vol. 30, no. 4, pp. 510–511, 1997.

[31] C. J. Howard and E. H. Kisi, "Measurement of single-crystal elastic constants by neutron diffraction from polycrystals," *J. Appl. Cryst.*, vol. 32, pp. 624–633, 1999.

[32] M. Finkel, *Experiments to determine the monocrystalline elastic constants in polycrystalline materials from diffraction data.* Masterthesis Technische Universität München, 2016.

[33] S. Fréour, D. Gloaguen, M. François, and R. Guillén, "Modelling and simulation of multi-phase effects on X-ray elasticity constants," *Physica Status Solidi (B) Basic Research*, vol. 239, no. 2, pp. 297–309, 2003.

[34] S. Freour, D. Gloaguen, A. P. M. Francois, and R. Guillen, "Determination of single-crystal elasticity constants in a cubic phase within a multiphase alloy: X-ray diffraction measurements and inverse-scale transition modelling," *Journal of Applied Crystallography*, vol. 38, pp. 30–37, September 2005.

[35] J. Bouillo, E. Girard, S. Fréour, R. Guillén, D. Gloaguen, and M. François, "Determination of the Macroscopic Elastic Constants of a Phase Embedded in a Multiphase Polycrystal-Application to the β-Phase of a Ti-17 Titanium Based Alloy," *Materials Science Forum*, vol. 404-407, pp. 723–728, 2009.

[36] D. H. Chung and W. R. Buessem, "The elastic anisotropy of crystals," *Journal of Applied Physics*, vol. 38, no. 5, pp. 2010–2012, 1967.

[37] S. I. Ranganathan and M. Ostoja-Starzewski, "Universal elastic anisotropy index," *Physical Review Letters*, vol. 101, no. 5, pp. 055504–4, 2008.

[38] D. Tromans, "Elastic Anisotropy of HCP Metal Crystals and Polycrystals," *International Journal of Recent Research and Applied Studies*, vol. 6, no. March, pp. 462–483, 2011.

[39] C. M. Kube, "Elastic anisotropy of crystals," *AIP Advances*, vol. 6, p. 095209, sep 2016.

[40] H. Behnken, *Mikrospannungen in vielkristallinen und heterogenen Werkstoffen*. Shaker Verlag, 2003.

[41] L. D. Landau and E. M. Lifschitz, *Lehrbuch der theoretischen Physik - VII Elastizitäts-theorie*. Verlag Harri Deutsch, 2010.

[42] A. Heldmann, M. Hoelzel, M. Hofmann, W. Gan, W. W. Schmahl, E. Griesshaber, T. Hansen, N. Schell, and W. Petry, "Diffraction-based determination of single-crystal elastic constants of polycrystalline titanium alloys," *Journal of Applied Crystallography*, vol. 52, no. 5, pp. 1144–1156, 2019.

[43] B. Gairola and E. Kröner, "A simple formula for calculating the bounds and the self-consistent value of the shear modulus of a polycrystalline aggregate of cubic crystals," *International Journal of Engineering Science*, vol. 19, pp. 865–869, jan 1981.

[44] H. Ledbetter and A. Migliori, "A general elastic-anisotropy measure," *Journal of Applied Physics*, vol. 100, no. 6, 2006.

[45] R. Hill, "The essential structure of constitutive laws for metal composites and poly-crystals," *Journal of the Mechanics and Physics of Solids*, vol. 15, no. 2, pp. 79–95, 1967.

[46] M. Hoelzel, A. Senyshyn, N. Juenke, H. Boysen, W. W. Schmahl, and H. Fuess, "High-resolution neutron powder diffractometer spodi at research reactor frmii," *Nuclear Instruments and Methods A*, vol. 667, pp. 32–37, 2012.

[47] H. G. Brokmeier, W. M. Gan, C. Randau, M. Völler, J. Rebelo-Kornmeier, and M. Hofmann, "Texture analysis at neutron diffractometer stress-spec," *Nuclear Instruments and Methods A*, vol. 642, pp. 87–92, 2011.

[48] T. C. Hansen, P. F. Henry, H. E. Fischer, J. Torrefrossa, and P. Convert, "The d20 instrument at the ILL: a versatile high-intensity two-axis neutron diffractometer," *Measurement Science Technology*, vol. 19, p. 034001, jan 2008.

[49] N. Schell, A. King, F. Beckmann, M. Müller, and A. Schreyer, "The high energy materials science beamline (HEMS) at PETRA III," *Materials Science Forum*, vol. 772, pp. 57–61, 2014.

REFERENCES

[50] M. Hoelzel, W. M. Gan, M. Hofmann, C. Randau, G. Seidl, P. Jüttner, and W. W. Schmahl, "Rotatable multifunctional load frames for neutron diffractometers at FRM II - Design, specifications and applications," *Nuclear Instruments and Methods in Physics Research, Section A: Accelerators, Spectrometers, Detectors and Associated Equipment*, vol. 711, pp. 101–105, 2013.

[51] Y. Kim, Y. M. Kim, J.-Y. Koh, T.-H. Lee, W. C. Woo, and H. N. Han., "Evaluation of single crystal elastic constants and stacking fault energy in high-nitrogen duplex stainless steel by in-situ neutron diffraction," *Scripta Materialia*, vol. 119, pp. 1–4, 2016.

[52] R. Woracek, J. R. Bunn, D. Penumadu, and C. R. Hubbard, "Method to determine hkl strains and shear moduli under torsion using neutron diffraction," *Applied Physics Letters*, vol. 100, p. 191904, Dezember 2012.

[53] W. Petry, "Phonons At Martensitic Phase Transitions Of Bcc-Ti, Bcc-Zr And Bcc-Hf," *Phase Transitions*, vol. 31, no. 1-4, pp. 119–136, 1991.

[54] J. Neuhaus, M. Leitner, K. Nicolaus, W. Petry, B. Hennion, and A. Hiess, "Role of vibrational entropy in the stabilization of the high-temperature phases of iron," *Physical Review B - Condensed Matter and Materials Physics*, vol. 89, no. 18, pp. 5–10, 2014.

[55] W. Petry, "Dynamical Precursors of Martensitic Transitions," *Le Journal de Physique IV*, vol. 05, no. C2, pp. C2–15–C2–28, 1995.

[56] W. Burgers, "On the process of transition of the cubic-body-centered modification into the hexagonal-close-packed modification of zirconium," *Physica*, vol. 1, no. 7, pp. 561 – 586, 1934.

[57] T. Lorentzen, M. R. Daymond, B. Clausen, and C. N. Tomé, "Lattice strain evolution during cyclic loading of stainless steel," *Acta Materialia*, vol. 50, no. 6, pp. 1627–1638, 2002.

[58] V. Hounkpati, S. Fréour, D. Gloaguen, V. Legrand, J. Kelleher, W. Kockelmann, and S. Kabra, "In situ neutron measurements and modelling of the intergranular strains in the near-β titanium alloy Ti-β21S," *Acta Materialia*, vol. 109, pp. 341–352, 2016.

[59] M. R. Daymond and H. G. Priesmeyer, "Elastoplastic Deformation of Two Phase Steels Studied by Neutron Diffraction and Self-consistent Modelling," *Acta Materialia*, vol. 50, pp. 1613–1626, 2002.

[60] L. Lutterotti, S. Matthies, H.-R. Wenk, A. S. Schultz, and J. J. W. Richardson, "Combined texture and structure analysis of deformed limestone from time-of-flight neutron diffraction spectra," *Journal of Applied Physics*, vol. 81, pp. 594–600, 01 1997.

REFERENCES

[61] J. Rodriguez-Carvajal, "Recent advances in magnetic structure determination by neutron powder diffraction," *Physica B: Condensed Matter*, vol. 192, pp. 55–69, 10 1993.

[62] H. M. Ledbetter, H. Ogi, S. Kai, S. Kim, and M. Hirao, "Elastic constants of body-centered-cubic titanium monocrystals," *Journal of Applied Physics*, vol. 95, no. 9, pp. 4642–4644, 2004.

[63] S. L. Raghunathan, A. M. Stapleton, I. Bantounas, H. J. Stone, T. C. Lindley, and D. Dye, "Evolution of lattice strain in ti-6al-4v during tensile loading at room temperature," *Acta Materialia*, vol. 56, pp. 6186–6196, 2008.

[64] S. Joseph, I. Bantounas, T. C. Lindley, and D. Dye, "Slip transfer and deformation structures resulting from the low cycle fatigue of near-alpha titanium alloy Ti-6242Si," *International Journal of Plasticity*, vol. 100, pp. 90–103, 2018.

[65] D. Banerjee and J. C. Williams, "Perspectives on titanium science and technology," *Acta Materialia*, vol. 61, no. 3, pp. 844–879, 2013.

[66] D. Gloaguen, T. Berchi, E. Girard, and R. Guillén, "Measurement and prediction of residual stresses and crystallographic texture development in rolled Zircaloy-4 plates: X-ray diffraction and the self-consistent model," *Acta Materialia*, vol. 55, no. 13, pp. 4369–4379, 2007.

[67] J. Fajoui, D. Gloaguen, V. Legrand, G. Oum, J. Kelleher, and W. Kockelmann, "Bauschinger Effect in an Austenitic Steel: Neutron Diffraction and a Multiscale Approach," *Metallurgical and Materials Transactions A: Physical Metallurgy and Materials Science*, vol. 47, no. 5, pp. 2024–2036, 2016.

[68] T. Richeton, F. Wagner, C. Chen, and L. S. Toth, "Combined effects of texture and grain size distribution on the tensile behavior of α-titanium," *Materials*, vol. 11, no. 7, pp. 10–13, 2018.

[69] S. Lhadi, M. R. Chini, T. Richeton, N. Gey, L. Germain, and S. Berbenni, "Micromechanical modeling of the elasto-viscoplastic behavior and incompatibility stresses of β-Ti alloys," *Materials*, vol. 11, no. 7, pp. 1–12, 2018.

A   Appendix

A.1   C# Code Examples of the Basic Classes

```csharp
public class Sample
    {
        #region Parameters

        private string _name;
        private double _area;

        public List<DataManagment.CrystalData.CODData>
            CrystalData;
        public List<Pattern.DiffractionPattern>
            DiffractionPatterns;
        public List<Stress.Macroskopic.TensileTest>
            TensileTests;

        public List<List<Stress.Microsopic.REK>>
            DiffractionConstants;
        public List<List<Stress.Microsopic.REK>>
            DiffractionConstantsTexture;

        public List<List<Stress.Microsopic.ElasticityTensors>>
            ElasticTensorData;

        public
            List<MathNet.Numerics.LinearAlgebra.Matrix<double>>
            StressTransitionFactors;
        public List<Stress.Plasticity.ElastoPlasticExperiment>
            SimulationData;
        ...

        #endregion
        #region Methods
        ...
        }
```

Listing 1 – All basic parameters implemented into the sample class. This class represent the heart of the data utilized by the software.

```csharp
public class StrainStressAssociation
    {
        #region Parameters

        public double PhaseFractionStress;
        public double Stress;

        public double PsiAngle;
        public double PhiAngle;

        private bool _elasticRegime;

        public double _macroskopicStrain;
        public double _Strain;
        public double _StrainError;

        private double _mRDValue = 0;

        public MathNet.Numerics.LinearAlgebra.Vector<double>
            MeasurementDirektionVektor;

        public Analysis.Peaks.DiffractionPeak DPeak;

        ...

        #endregion

        #region Methods

        public MathNet.Numerics.LinearAlgebra.Matrix<double>
            MeasurementSystemStress();

        ...

        #endregion

    }
```

Listing 2 – All basic parameters implemented into the Strain class. This class handles the strain values obained by diffraction experiments. It is the core class for the elastic calculations.

A.1 C# Code Examples of the Basic Classes

```csharp
public class YieldSurface
    {
            #region Parameters

        public List<ReflexYield> ReflexYieldData;

        public List<ReflexYield> PotentialSlipSystems;

        public  DataManagment.CrystalData.CODData CrystalData;
        ...

        #endregion

        #region Methods

        public MathNet.Numerics.LinearAlgebra.Matrix<double>
            HardeningMatrixSlipSystem(List<ReflexYield>
            potActiveSystems, ...)
        public MathNet.Numerics.LinearAlgebra.Matrix<double>
            HardeningMatrixSlipSystem(List<ReflexYield>
            potActiveSystems)
        public MathNet.Numerics.LinearAlgebra.Matrix<double>
            SlipSystemX(List<ReflexYield> potActiveSystems, ...)
        public MathNet.Numerics.LinearAlgebra.Matrix<double>
            GetInstStiffnessFactors(List<ReflexYield>
            potActiveSystems, ...)
        public bool CheckForMise(ReflexYield reflex,
            MathNet.Numerics.LinearAlgebra.Matrix<double>
            aStress)
        public bool CheckStandard(ReflexYield reflex,
            MathNet.Numerics.LinearAlgebra.Matrix<double>
            aStress)
        ...

        #endregion
        }
```

Listing 3 – All basic parameters and methods implemented into the YieldSurface class. This class handles the strain values obained by diffraction experiments. It is the core class for the EPSC calculations.

```csharp
public class ElasticityTensor
    {
        #region Parameters

        public MathNet.Numerics.LinearAlgebra.Matrix<double>
            _stiffnessTensor;
        public MathNet.Numerics.LinearAlgebra.Matrix<double>
            _stiffnessTensorError;
        public MathNet.Numerics.LinearAlgebra.Matrix<double>
            _complianceTensor;
        public MathNet.Numerics.LinearAlgebra.Matrix<double>
            _complianceTensorError;
        public Texture.OrientationDistributionFunction ODF;
        public List<REK> DiffractionConstants = new
            List<REK>();
        public List<REK> DiffractionConstantsTexture = new
            List<REK>();

        public double AnIsotropy = 1.0;
        ...

        #endregion

        #region Methods

        public double
            S1ReussCubic(DataManagment.CrystalData.HKLReflex hKL)
        public double
            HS2ReussCubic(DataManagment.CrystalData.HKLReflex
            hKL)
        ...

        #endregion

    }
```

Listing 4 – All basic parameters implemented into the ElasticityTensor class. This class handles the basic methods for elastic behavior. It is the core class for the elastic calculations.

```csharp
public class SimulationData
    {
        #region Parameters

        public List<MathNet.Numerics.LinearAlgebra.
            Matrix<double>> StressSFHistory;
        public List<MathNet.Numerics.LinearAlgebra.
            Matrix<double>> StrainSFHistory;
        public List<MathNet.Numerics.LinearAlgebra.
            Matrix<double>> StressRateSFHistory;
        public List<MathNet.Numerics.LinearAlgebra.
            Matrix<double>> StrainRateSFHistory;
        public List<List<GrainOrientationParameter>>
            GrainOrientations;
        public List<List<List<List<double>>>>
            YieldChangeCFHistory;
        public List<List<List<MathNet.Numerics.LinearAlgebra.
            Matrix<double>>>> StressRateCFOrientedHistory = new
            List<List<List<MathNet.Numerics.LinearAlgebra.
            Matrix<double>>>>();
        public List<List<List<MathNet.Numerics.LinearAlgebra.
            Matrix<double>>>> StrainRateCFOrientedHistory = new
            List<List<List<MathNet.Numerics.LinearAlgebra.
            Matrix<double>>>>();
        public List<List<List<List<ReflexYield>>>>
            ActiveSystemsCFOrientedHistory = new
            List<List<List<List<ReflexYield>>>>();
        ...

        #endregion

        #region Methods
        ...

        }
```

Listing 5 – All basic parameters implemented into the Simulation class. This class handles the complete data during the EPSC modeling. It is the core class for the EPSC data storage.

A.2 C# Code Examples of the Basic Methods

```csharp
public static bool FitElasticityTensor(ElasticityTensors ET)
        {
            ElasticityTensors TrialET = ET.Clone();

            for (int TotalTrials = 0; TotalTrials <
               MaxFittingTrials; TotalTrials++)
            {
                Vector<double> ParamDelta;
                ParamDelta = ET.ParameterDeltaVektor(Lambda);

                TrialET.Parameter += ParamDelta;

                double Chi2Trial = Chi2.Chi2Classic(TrialET);
                double Chi2Real = Chi2.Chi2Classic(ET);

                if (Math.Abs(Chi2Trial - Chi2Real) >
                   FunctionFittingAcuraccy)
                {
                    if (Chi2Trial > Chi2Real)
                    {
                        TrialET.Parameter = ET.Parameter;
                        Lambda *= FittingLambdaMulti;
                    }
                    else
                    {
                        ET.Parameter  = TrialET.Parameter ;
                        Lambda /= FittingLambdaMulti;
                    }
                }
                else
                {
                    if (TotalTrials > 3)
                    {
                        return true;
                    }
                    else
                    {
                        if (Chi2Real > Chi2Trial)
                        {
```

```
                              ET.Parameter   = TrialET.Parameter ;
                              Lambda /= FittingLambdaMulti;
                        }
                  }
            }
      }
      return false;
}
```

Listing 6 – Basic LMA implementation for the elasticity tensors.

```csharp
public static bool FitElasticityTensorLoadTransfer (...)
        {
        while(difference < limit)
                {
                Matrix<double> first = -1 * sampleStiffnesses
                    * (eshelbyTensor - unity);
                Matrix<double> second = (_stiffnessTensor -
                    sampleStiffnesses) * eshelbyTensor;

                second += sampleStiffnesses;
                Matrix<double> third =
                    (this.ReussTensorData[inclusion]._stiffnessTensor
                    - sampleStiffnesses) * sampleCompliances;

                Matrix<double> ret1 = first * second.Inverse()
                    * third;
                ret1 += unity;
                ...
                FourthRankTensor firstFR = -1.0 *
                    sampleStiffnessesFR * (eshelbyTensorFR -
                    unityFR);

                FourthRankTensor secondFR =
                    (phaseStiffnessesFR - sampleStiffnessesFR) *
                    eshelbyTensorFR;
                secondFR += sampleStiffnessesFR;

                FourthRankTensor thirdFR = (phaseStiffnessesFR
                    - sampleStiffnessesFR) * sampleCompliancesFR;
                ...
                FourthRankTensor secondInverseFR =
                    secondComp.Inverse();

                FourthRankTensor ret1FR = firstFR *
                    secondInverseFR * thirdFR;
                ret1FR += unityFR;

                Matrix<double> ret1Comp =
                    ret1FR.GetVoigtTensor();
                Matrix<double> ret2 = +-1 -
```

```
                    (this.CrystalData[inclusion].PhaseFraction *
                    ret1;
            ret2 /= this.CrystalData[matrix].PhaseFraction;

            this.StressTransitionFactors.Clear();
            ResetPhaseStresses()...
            RefitAllDECStressCorrected()...
            RefitElasticConstants()...
            difference = elasticConstantsTrial -
                elasticConstants;
    }
```

Listing 7 – This listing shows the self-consistent routine to determine elastic constants in multi-phase alloys

A.3 C# Code Examples of the EPSC Modeling

```csharp
public static void PerformStressExperiment(Sample actSample,
   ...)
      {
      FourthRankTensor overallStiffnesses =
         GetSampleStiffnesses(textureActive);
      FourthRankTensor overallStiffnessesComp =
         overallStiffnesses.Clone();
      ...
      for (int phase = 0; phase <
         actSample.CrystalData.Count; phase++)
      {
      potentialActiveGOriented.Add(new
         List<List<ReflexYield>>());
      grainStressesOriented.Add(new List<Matrix<double>>());
      grainStrainsOriented.Add(new List<Matrix<double>>());
      shearRate.Add(new List<List<double>>());
      yieldChangeOriented.Add(new List<List<double>>());
      averageYieldChange.Add(new double[5]);
      plasticTensorPhase.Add(new List<PlasticityTensor>());
      }
      for (int actCycle = 0; actCycle < cycleLimit;
         actCycle++)
{

      constraintStiffness =
         actSample.PlasticTensor[0].GetConstraintStiffness(eTmp,
         2);
      for (int phase = 0; phase <
         actSample.CrystalData.Count; phase++)
      {
      for (int grainIndexTmp = 0; grainIndexTmp <
         grainIndexCounter; grainIndexTmp++)
      {
      if (singleCrystalTracking)
      {
      ...
            for (int pS = 0; pS <
               YieldInformation[phase].PotentialSlipSystems.Count;
               pS++)
      {
```

```csharp
                PotentialSlipSystems[pS].YieldMainHardennedStrength
                    += hardennedYield[pS];
            }
    }
    Matrix<double> transformationMatrix;
    if (actCycle == 0)
    {
            for (int k = 0; k < n; k++)
            {
            actStressGrainBc +=
                StressRateCFOrientedHistory[phase][k][grainIndex];
            }
    actStressRateGrainBc = stressRateS;
    }
    else
    {
    FourthRankTensor lastBc;
    for (int k = 0; k < n; k++)
    {
    actStressGrainBc
        +=StressRateCFOrientedHistory[phase][k][grainIndex];
    }
    actStressRateGrainBc = lastBc * stressRateS;
    }
    actStressOriented = actStressGrainBc +
        actStressRateOriented;
    List<ReflexYield> potentialActive =
        GetPotentiallyActiveSlipSystems (actStressOriented,
        slipCriterion);
    if (potentialActive.Count != 0)
    {
    YieldInformation[phase].CheckDependencies (...);
    while(trialSystems.Count != 0)
    {
    ...
            HardeningMatrix =
                YieldInformation[phase].HardeningMatrixSlipSystem
                (trialSystems);
    ...
    ConditionX =
        YieldInformation[phase].SlipSystemX(trialSystems,
```

```csharp
        plasticTensorGrain.HardeningMatrix, ...);
            for (int i = 0; i < trialSystems.Count; i++)
            {
            InstantStiffnessFactors.Add
                (YieldInformation[phase].GetInstStiffnessFactors
                (trialSystems, TensorData[phase], i,
                plasticTensorGrain.ConditionY));
        }
        GrainStiffness =
            GetInstantanousGrainSiffnessTensor(trialSystems,
            TensorData[phase],
            plasticTensorGrain.InstantStiffnessFactors);
        if (invDifference < 0.0001)
        {
                GrainTransitionStiffness =
                    PlasticTensor[phase].GetTransitionConstants
                    (constraintStiffness,
                    plasticTensorGrain.GrainStiffness,
                    overallStiffnesses);
                SetShearRates()...
        if (!negativeShear)
        {
        SetYieldChange()...
                if (difference < 1)
        {
                ParameterSave()...
                }
                }
        }
        }
        }
        overallStiffnessesPhase[phase] =
            AverageInnerProduct(plasticTensorPhase[phase]);
        }
        for (int phase = 0; phase <
            actSample.CrystalData.Count; phase++)
        {
        overallStiffnesses +=
            actSample.CrystalData[phase].PhaseFraction *
            overallStiffnessesPhase[phase];
        }
```
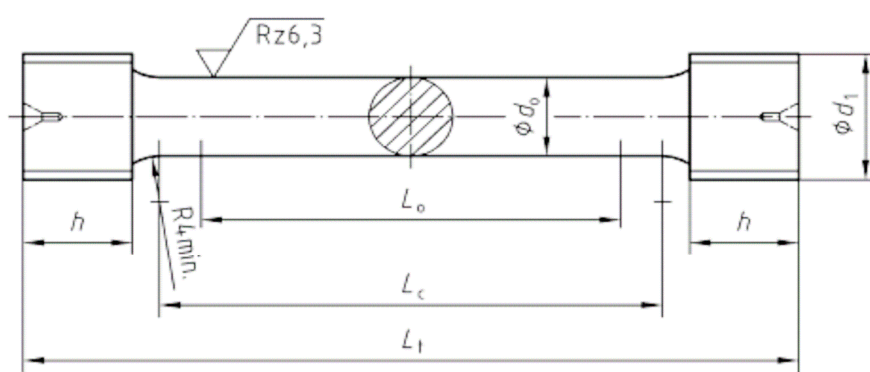
126

```csharp
        if (overallDifference < 100)
        {
        break;
        }
        else
        {
        overallStiffnessesComp = overallStiffnesses.Clone() as
           Tools.FourthRankTensor;
        }
        }
        SaveAllParameters()...
}
```

Listing 8 – This listing shows major parts of the EPSC routine

```csharp
        if (overallDifference < 100)
```

Round sample type 1 (tension)

d_0	L_0	d_1 (thread)	h min.	L_C min.	L_t min.
4	20	M6	6	24	40
5	25	M8	7	30	50
6	30	M10	8	36	60
8	40	M12	10	48	75
10	50	M16	12	60	90